Cyclist Aerodynamic Drag Analysis through Large-Scale PIV

Terra, W.

DOI
10.4233/uuid:7be5ba28-0699-408f-be0e-3e4c448cb42c

Publication date
2020

Document Version
Final published version

Citation (APA)
Terra, W. (2020). *Cyclist Aerodynamic Drag Analysis through Large-Scale PIV*.
https://doi.org/10.4233/uuid:7be5ba28-0699-408f-be0e-3e4c448cb42c

Cyclist Aerodynamic Drag Analysis through Large-Scale PIV

Cyclist Aerodynamic Drag Analysis through Large-Scale PIV

Dissertation

for the purpose of obtaining the degree of doctor
at Delft University of Technology
by the authority of the Rector Magnificus, prof. dr.ir. T.H.J.J. van der Hagen,
chair of the Board for Doctorates
to be defended publicly on
23 November 2020 at 12:30 o'clock

by

Wouter TERRA

Master of Science in Aerospace Engineering,
Delft University of Technology, the Netherlands,
born in Alkmaar, the Netherlands.

This dissertation has been approved by the promotors.

Composition of the doctoral committee:

Rector Magnificus,	chairperson
Prof. dr. F. Scarano,	Delft University of Technology, promotor
Dr. A. Sciacchitano,	Delft University of Technology, copromotor

Independent members:

Prof. dr. W. van de Water,	Delft University of Technology
Prof. dr. B. Blocken,	Eindhoven University of Technology
Dr. R. Stevens,	Renault F1 Team
Dr. T. Crouch,	Monash University
Dr. D. Rival,	Queen’s University
Prof. dr. L.L.M. Veldhuis,	Delft University of Technology, reserve member

Keywords: Cycling aerodynamics, aerodynamic drag, large-scale PIV

Printed by: Koninklijke Rijnja BV

Front & Back: Cover design by Koen Terra

ISBN 978-94-6384-179-5

An electronic version of this dissertation is available at
http://repository.tudelft.nl/.

to Nicky, Bo and Max

CONTENTS

SUMMARY

The use of large-scale particle image velocimetry (PIV) is proposed for cycling aerodynamic study to advance the general understanding of the flow around the rider and the bike, leading to new strategies for cycling aerodynamic drag reduction in the future. The investigation concentrates on the measurement of the wake velocity and its relation to the aerodynamic drag of stationary models in wind tunnels and of transiting models in the field.

In the first part of this work, PIV measurements are conducted in a wind tunnel to capture the wake flow topology of a full-scale cyclist model and determine the cyclist aerodynamic drag. In-house built seeding systems are employed to inject Helium-filled soap bubble (HFSB) tracers upstream of an elite time-trial cyclist replica. The obtained flow topology compares well among different experimental repetitions and with literature, demonstrating the robustness of the PIV measurement approach. The aerodynamic drag is obtained by a so-called PIV wake rake approach, which relies on the conservation of momentum in a control volume surrounding the model. Comparison of the PIV wake rake aerodynamic drag against that of a force balance demonstrates that a drag accuracy of the latter below 1% is possible.

The PIV wake rake measurements are conducted in a plane downstream of the bike's rear wheel to avoid shadows and optical blockage. At this distance from the athlete, however, investigation of the separated and reverse flow regions, that are the main driver of the aerodynamic drag, is not possible. In the second part of this dissertation, therefore, robotic volumetric PIV measurements are conducted to retrieve the velocity description close to the cyclist. The near-wake of the cyclist limbs is presented, which somehow resembles that of isolated bluff bodies, such as cylinders, featuring a recirculation region bounded by two shear layers. The size of the recirculation region, however, is not only governed by the width of the limb, but also by the coherent vortical structures emanating from these limbs near the limb junctions (e.g. elbows and knees). Moreover, interaction of the limbs with the wakes of the upstream body parts also plays a role in the local wake properties.

In addition to the measurement of the cyclist's near wake at typical race speed, also the cyclist Reynolds number effects are investigated to understand how to reduce the aerodynamic drag by dedicated skinsuits designs in the future. This is achieved repeating the robotic volumetric PIV measurements in a wide range of freestream velocity. While reductions of the wake width are observed on both lower leg and arm with increasing free-stream velocity, the wake of the upper leg follows an opposite trend increasing in size at higher velocity. These variations of wake width with increasing freestream speed are related to the behaviour of the local drag coefficient, indicating a drag crisis behaviour on both leg and arm. The distribution of the so-called critical velocity upon these body segments is discussed, as it determines the freestream speed where a minimum value for the drag occurs.

The third, and last part of this work, is dedicated to the development of quantitative flow visualisation and drag determination of cyclists in the field. This so-called Ring-of-Fire system allows, among others, aerodynamic studies that are practically impossible in the wind tunnel, such as model accelerations and model curved-linear trajectories. A tomographic PIV wake rake is employed to measure the flow around a simplified transiting bluff body, a towed 10 cm sphere. These scaled experiments serve as a proof-of-concept of this novel measurement system.

The aerodynamic drag is obtained invoking the control volume momentum balance in a frame of reference moving with the object. The expression for the time-average drag consists of three terms, a momentum, Reynolds stress and pressure term, which are individually evaluated at increasing distance downstream of the sphere. It is shown that the aerodynamic drag is most accurately evaluated when the contribution of the momentum term dominates the overall drag and that the PIV pressure evaluation can be avoided five sphere diameters into the wake. The latter largely simplifies the data reduction procedures of the Ring-of-Fire. Finally, the present system estimates the aerodynamic drag with an accuracy of 20 drag counts. This is evaluated from repeated model passages in a range of Reynolds numbers in which the model's drag coefficient is constant. This resolution is comparable to other aerodynamic drag measurement field techniques. It is rather poor, instead, in comparison to force balance measurements in wind tunnels. In contrast to the latter drag measurement techniques, the Ring-of-Fire also provides information about the flow yielding advanced insights into cyclist aerodynamics in the future.

SAMENVATTING

Het gebruik van grote-schaal particle image velocimetry (PIV) wordt voorgesteld voor fiets aerodynamisch onderzoek om de kennis van de stroming rond een wielrenner en de fiets te verbreden en te verdiepen. Het onderzoek concentreert zich op het meten van de stromingssnelheid in het zog in relatie tot de luchtweerstand en richt zich op zowel stationaire modellen in windtunnels als voorbijkomende objecten in het veld.

In het eerste deel van dit onderzoek, zijn PIV metingen gedaan in een windtunnel om de topologie van het zog van een wielrenner te meten en hieruit de luchtweerstand te bepalen. Er is gebruikt gemaakt van in huis gemaakte instrumenten voor het injecteren van helium-gevulde zeepbellen, die dienst doen als PIV tracers. Deze worden stroomopwaarts van een 1:1 replica van een wielrenner in tijdrithouding geïnjecteerd in de stroming. De resulterende stroming typologieën van verschillende experimentele herhalingen vertonen grote gelijkenis onderling en met de literatuur, wat de robuustheid van de PIV meetmethode aantoont. De luchtweerstand wordt verkregen via een zogenoemde PIV zog-hark methode, welke berust op het behoud van impuls in een controle volume dat het model omgeeft. De vergelijking van de PIV zog-hark luchtweerstand met die van een krachtenbalans toont aan dat een weerstandsnauwkeurigheid van de eerst genoemde van onder de 1% mogelijk is.

De PIV zog-hark metingen zijn gedaan in een vlak stroomafwaarts van het achterwiel van de fiets om schaduwen en optische blokkades te voorkomen. Op deze afstand van de atleet is het echter niet mogelijk om loslating en gebieden met terugstroming te onderzoeken, welke de grootste bijdragers zijn aan de luchtweerstand. In het tweede deel van dit onderzoek wordt daarom gebruik gemaakt van robot gestuurde volumetrische PIV om de stroming vlak rond de renner te beschrijven. Het nabije-zog van verschillende ledematen van de renner wordt gepresenteerd. Dit vertoont enige gelijkenis met het zog van geïsoleerde stompe objecten, zoals cilinders, met een recirculatie gebied afgebakend door twee afschuiflagen. Het formaat van het recirculatiegebied wordt echter niet alleen bepaald door de breedte van de ledematen, maar ook door de aanwezige coherente wervelstructuren die ontstaat in de stroming rond de verbindingen tussen de ledematen, zoals de ellenbogen en knieën. Bovendien speelt de interactie van de stroming rond de ledematen met die van lichaamsdelen stroomopwaarts ook een rol in de eigenschappen van het zog.

Naast de metingen van het nabije zog van de renner op een typische racesnelheid, zijn ook de Reynolds getal effecten in de stroming onderzocht om te begrijpen hoe de luchtweerstand in de toekomst verder verlaagd kan worden middels nieuwe tijdritpakken. Dit is gerealiseerd door de robot gestuurde volumetrische PIV metingen te herhalen binnen een groot snelheidsbereik van de vrijestroming. Terwijl zog versmallingen worden waargenomen achter het onderbeen en de arm met een verhoging van de snelheid, wordt het zog van het bovenbeen in deze situatie juist breder. Deze variatie van de breedte van het zog met een toenemende snelheid van de vrije stroming wordt gerelateerd aan de variatie van de lokale weerstand coëfficiënt. Dit toont typisch weerstand-dal gedrag aan op zowel het been als de arm. Tenslotte wordt de verdeling van de

zogenoemde kritische snelheid over de ledematen besproken, welke de snelheid is met bijbehorende minimale lokale weerstand coëfficiënt.

Het derde en laatste deel van dit werk is gewijd aan de ontwikkeling van een kwantitatieve stroming visualisatie en luchtweerstandsmeting van wielrenners in het veld. Met deze zogenoemde Ring-of-Fire zijn aerodynamische studies mogelijk die in de praktijk onmogelijk zijn in windtunnels, zoals metingen op versnellende objecten en objecten die een gekromd traject afleggen. Een tomografische PIV zog-hark wordt gebruikt om de stroming rond een voorbijkomend stomp object de meten, namelijk een bol van 10 cm diameter. Deze geschaalde metingen dienen als bewijs van het concept van dit nieuwe meetsysteem. De luchtweerstand wordt bepaald door beroep te doen op het behoud van impuls in een referentiesysteem dat meebeweegt met het object. De uitdrukking van de tijdgemiddelde luchtweerstand bestaat uit drie termen, een impuls, een Reynolds spanning en een druk term, waarvan de waarde individueel bepaald wordt bij toenemende afstand achter de bol. Er wordt getoond dat de luchtweerstand het nauwkeurigst bepaald wordt als de contributie van de impuls term de totale luchtweerstand domineert en als de bepaling van druk uit de PIV data voorkomen kan worden, namelijk meer dan vijf bol diameters in het zog. Dit laatste vereenvoudigt de benodigde Ring-of-Fire data reductie aanzienlijk. Tenslotte, meet het gebruikte systeem de luchtweerstand met een nauwkeurigheid van 20 weerstandstellen. Dit is bepaald door middel van herhalende passages van de bol binnen een Reynolds getal bereik waarbinnen de weerstand coëfficiënt van de bol constant aangenomen mag worden. Deze resolutie is vergelijkbaar met die van andere luchtweerstand veldmeettechnieken. In vergelijking met balans metingen in een wind tunnel is dit echter mager. In tegenstelling tot de andere technieken voorziet de Ring-of-Fire echter ook in stromingsinformatie, welke nieuwe fiets aerodynamische inzichten op kan leveren in de toekomst.

1

INTRODUCTION

Cycling aerodynamics is introduced here, with particular relevance to the aerodynamic drag and its impact on the rider's performance. The research tools used for cycling aerodynamic investigations are briefly surveyed and the potential of particle image velocimetry (PIV) to extent the description of the flow around a cyclist and determination of the wind resistance is discussed. The chapter closes with the statement of motivation and objectives of the work, along with the organisation of this PhD dissertation.

1.1 A short history of cycling

On November 20, 1866, the world witnessed the first patented bicycle (Lallement 1866; Figure 1.1) featuring a steering device, a seat and a frame and two wheels largely made out of wood. This is typically considered to be one of the first modern bikes, despite the fact that the power exerted on the pedals is directly transmitted to the front wheel hub, rather than by a chain to the rear hub. The latter improved safety, speed and comfort and, by the end of the 19th century, the bike was used for daily transportation by the masses (e.g. Malizia and Blocken 2020).

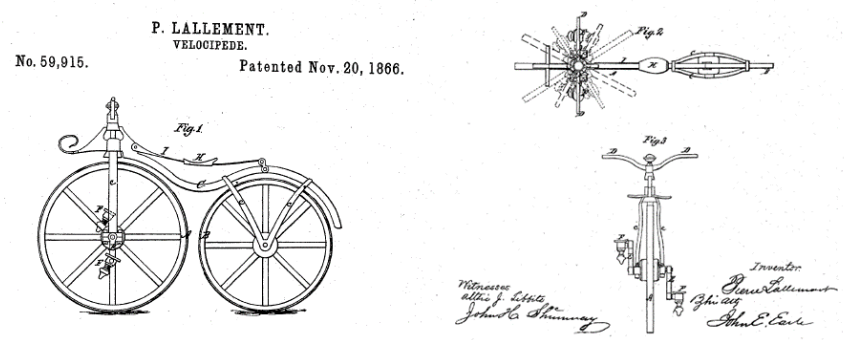

Figure 1.1: Drawing of the first modern bike (Lallement 1866).

Riding speed kept increasing, among others through application of inflatable tires and the use of gearing. In 1903 Henri Desgrange sensationally proposed a bike race through all of France to promote *L'Auto*, the magazine he was chief editor of. By that summer, the first edition of the *Tour de France* was organised, which arguably evolved throughout the 20th century into the most prestigious bike competition in the world (over 15 million spectators on the streets, one billion watching it, an annual turnover over 50 million euro). It was also Desgrange that set the first world hour record (WHR) in 1893 (Figure 1.2) completing a distance of 35,325 meters on the *Vélodrome Buffalo* in Paris. The application of technological advancements in materials and manufacturing techniques, among others, has affected race bike design significantly and it allowed Victor Campenaerts to set the current Union Cycliste Internationale (UCI) world hour record to a stunning 55,089 meters. The UCI is the responsible organization for regulating, among others, bike geometry and rider garment in competition. The history of this 1-hour time-trial reflects the large impact of aerodynamics, and in particular the aerodynamic drag, in competitive cycling. The 49,431 meters of Eddy Merckx, set at an altitude of 2240 meter above sea level, resulting in relatively low air resistance, stood over a decade. By adopting more streamlined positions on specifically designed aero bikes, among others, Graeme Obree (1994) and, later, Chris Boardman (1996), set new records. The latter 56,375 meter was conducted in the famous *superman-position* and is still recognized as the best human effort to date. As a consequence of the UCI ban of such extreme bike designs in the year 2000, the world-hour record dropped back, close to that of Merckx set in 1972. Only after a relaxation of the regulations in 2014 (allowing among others time-trial handlebars and disc wheels) a significant increase in the hour record has been achieved.

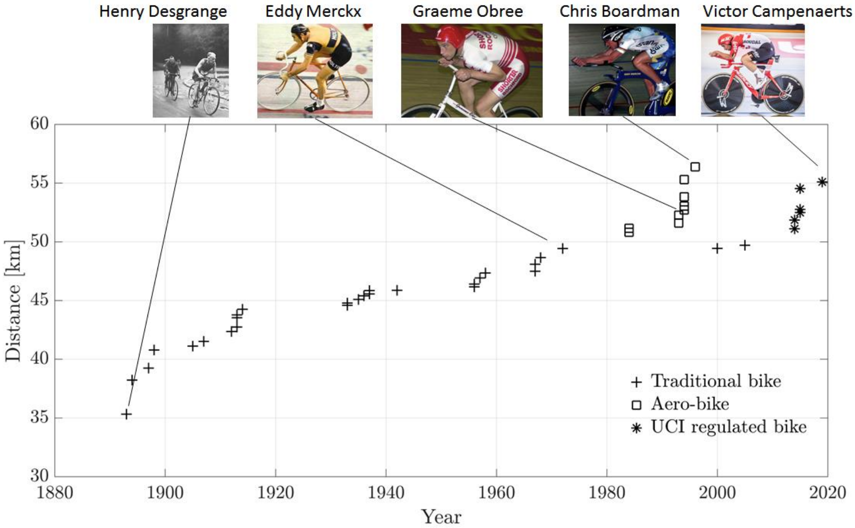

Figure 1.2: History of the world hour record (Wikipedia).

1.2 Cyclist aerodynamic drag

The direct resistive forces acting on a bike-rider system, hereafter simply referred to as the cyclist, at constant speed on a flat, non-inclined road are the aerodynamic drag, D_{air}, hereafter also simply referred to as D, and the rolling resistance, D_{roll} (Figure 1.3 left). The latter originates from the friction between the tires and the road. The aerodynamic drag, or air resistance, results from the relative velocity, U between the object and the surrounding air and acts in the direction opposite to the cyclist motion:

$$D = 0.5\rho U^2 C_D A \qquad 1.1$$

where ρ is the air density and C_D A are the drag coefficient and the frontal area of the cyclist, respectively. Instead of considering the latter two separately, in cycling aerodynamic research the aerodynamic performance is generally expressed by the drag area, $C_D A$ [m^2]. At typical race speeds (~50 km/h), the aerodynamic drag dominates the total resistive force contributing to approximately 90% (e.g. Kyle and Burke 1984; Martin et al. 1998). Hence, one strategy to improve rider performance is to reduce aerodynamic drag. The quantification of this drag is essential and therefore a physical understanding of its generation is necessary.

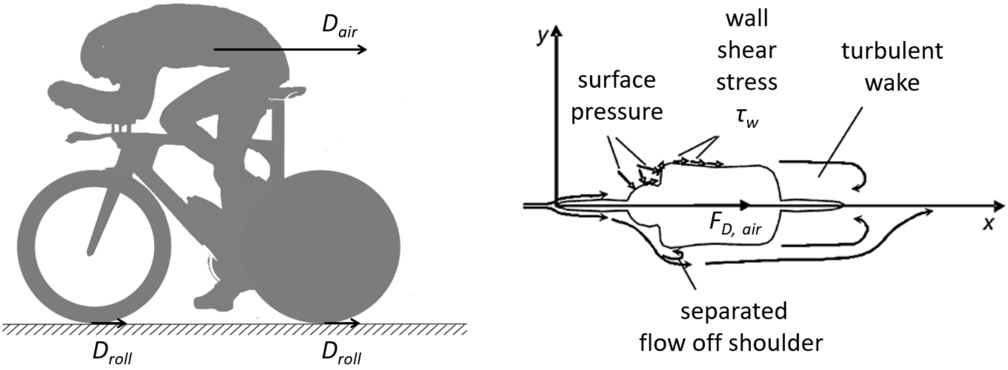

Figure 1.3: The bike-rider system: external forces and moments (left) and schematic flow topology (right; Figure reproduced from Martin et al. 2007).

The aerodynamic drag can be decomposed into pressure drag, D_{pres} and friction drag, D_{fric} resulting from the pressure and shear stress distribution over a model's surfaces (illustrated in Figure 1.3-right), respectively:

$$D = D_{pres} + D_{fric} \tag{1.2}$$

In front of the cyclist the flow decelerates and locally stagnates in close proximity to the model, generating regions with pressure excess. Instead, pressure deficits mostly occur in the wake, as a consequence of the flow separation, among others, over the rider's limbs and lower back. This difference in pressure results in a relatively large drag force. In comparison, the friction drag is smaller and often neglected, and the cyclist can typically be considered as a bluff body. A detailed discussion on bluff body aerodynamics and the cyclist flow topology is provided in Chapter 2.

As a consequence of the relatively small friction drag, cyclist drag reduction strategies generally aim to reduce pressure drag. Drafting is arguably the most efficient way to achieve this. As a consequence of riding in the low-pressure wake of one or multiple leading cyclists, the air resistance of the trailing rider may reduce over about 40% (e.g. Defraeye et al. 2013; Blocken et al. 2013) and over 90% in pelotons (Blocken et al 2018). Reduction of the aerodynamic drag of an individual rider may be achieved, among others, by changing the rider's position, its garments or the bike. The former strategy is generally considered the most effective (e.g. Kyle and Burke 1984). To illustrate this, three main elite rider positions are depicted in Figure 1.4. Changing from the upright position into the drops and time-trial posture reduces the aerodynamic drag by 15-20% and 30-35%, respectively (Lukes et al. 2005; Crouch et al. 2017). Reductions of the aerodynamic drag by garment modification (next section) or bike streamlining, instead, are generally well below 10%. Detailed overviews of cycling aerodynamic and drag reducing strategies are provided, among others, by Lukes et al. (2005)

and Crouch et al. (2017). The recent review work of Malizia and Blocken (2020) particularly focuses on the bike aerodynamics.

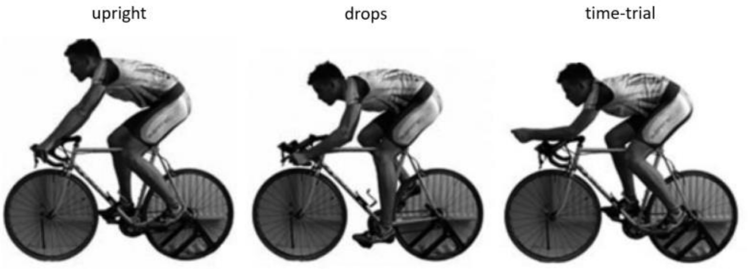

Figure 1.4: Main cyclist positions (Figure adopted from Lukes et al. 2005).

1.3 Low-drag skinsuits

A drag reducing approach that is particularly relevant to cycling is that of streamlining the cyclist apparel. Early works in literature have shown that tightly fitting *Lycra* suits are able to reduce the aerodynamic drag by more than 10% in comparison to woollen suits (Van Ingen Schenau 1982) and loosely fitting apparel (Brownlie 1992). Currently, zoned skinsuits are typically used, consisting of smooth and rough patches on different parts of the cyclist body (e.g. Brownlie 2009; Figure 1.5-left). This design concept relies on the phenomenon of the *drag crisis*, which is generally associated with the steep decrease and subsequent increase of the drag coefficient for bluff bodies, such as circular cylinders, spheres and alike, with increasing Reynolds number (Figure 1.5-right). The underlying laminar to turbulent transition process responsible for this rapid change in drag coefficient is discussed in more detail in Section 2.1.2. Apart from the Reynolds number, the drag crisis behaviour can also be controlled acting on model's surface roughness or surface texture. Increasing the latter can anticipate the laminar to turbulent transition and shift the drag crisis to lower Reynolds numbers (Achenbach 1971; Figure 1.5-right).

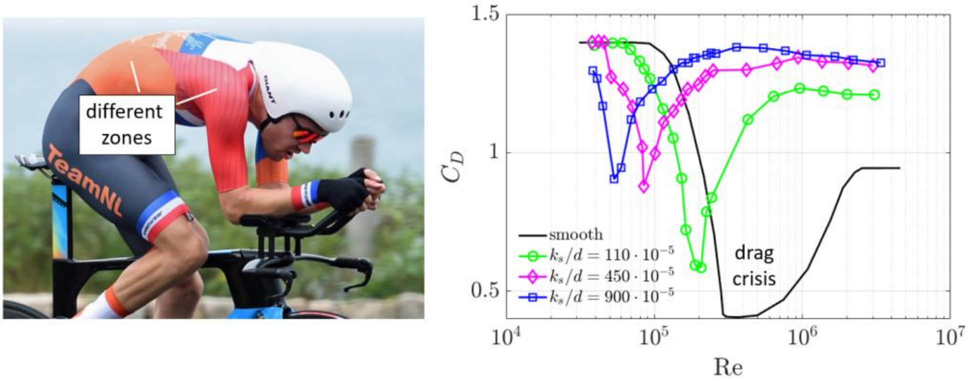

Figure 1.5: Illustration of zoned skinsuit (left; Figure adapted from Wielerflits 2017) and the circular cylinder drag crisis (right; Figure reproduced from Achenbach 1971. k_s/d is the dimensionless surface roughness)

Selection of the appropriate skinsuit fabrics, and moreover the division of the body into zones, relies strongly on the assumed similarities between the flow across the human limbs and that of general isolated bluff bodies. First of all, it is assumed that the cyclist limbs feature typical drag crisis behaviour, and secondly, that this behaviour is governed mainly by the local limb thickness. This allows fabric selection based on isolated bluff bodies force balance measurement data, similar to that depicted in Figure 1.5-right. However, given the geometrical complexity of the athlete’s body and equipment, modelling the cyclist drag crisis based on these simplified bluff bodies measurements and superposition of effects may to yield inaccurate conclusions. In comparison to isolated bluff geometries, the cyclist flow and drag crisis behaviour is expected to be distorted by wake interactions (Section 2.2.2), junction regions and free ends (Section 2.2.3) and other three-dimensional features. Although, drag crisis behaviour is known to vary among individual body segments (Defraeye et al. 2011; D’Auteuil et al. 2012), variations along body limbs have not been presented and the mechanisms governing the flow Reynolds number effects are not yet fully understood. Chapter 5 of the present work is dedicated to study of the cyclist Reynolds number effects with a focus on when the drag crisis phenomenon occurs.

1.4 Methods for cycling aerodynamic investigation

The gross of the cyclist aerodynamic studies aims to reduce the rider’s aerodynamic drag, which can be evaluated in the field, in wind tunnels or by flow modelling. In addition, some studies use the information of the flow around the cyclist, measured or available from the models, to gain insight into the generation of the air resistance and to determine drag minimization strategies. This section surveys the main cycling aerodynamic testing techniques and their capabilities and limitations to understand how the description of cycling aerodynamics may be extended using PIV. The next section is particularly dedicated to latter technique and, so, it is omitted here.

1.4.1 Field measurements

Cycling aerodynamic field tests typically provide the aerodynamic drag by measuring the athletes’ power exerted on the bike’s pedals or cranks and estimating the system’s rolling resistance using linear regression. These tests are generally conducted riding at constant speed, on a flat surface and in the absence of wind or, more recently, with a Pitot tube mounted upstream of the bike’s handlebars to determine the relative velocity between cyclist and surrounding air (Fitzgerald et al. 2019). Other approaches consist of coast-down tests, towed models or rely on the measurement of the rider’s oxygen intake as summarized by Debraux et al. (2011). Although a systematic drag accuracy assessment is missing in literature, these field techniques are generally considered relatively inaccurate in comparison to balance measurements in wind tunnels (e.g. Crouch et al. 2017)

Nonetheless, field tests are common practise for cycling aerodynamic testing. An important advantage of field testing is that it provides the cyclist’s aerodynamic performance during an unconstrained cycling motion and it allows replication of the conditions experienced in competition. Furthermore, field measurements allow aerodynamic investigation of large cyclist groups and pelotons, which are rarely possible in wind tunnels. These techniques also allow aerodynamic investigations that are practically infeasible in wind tunnels (e.g. model accelerations and curved-linear trajectories).

Figure 1.6: Measurement techniques adopted for cycling aerodynamic research: pressure probe scanning the wake (left; adopted from Crouch 2013); pressure taps on the cyclist's back (middle; adopted from Crouch et al. 2014); China clay visualization depicting separation line on upper arm (right; adopted from Brownlie et al. 2009).

1.4.2 Wind tunnel experiments

Measurements in wind tunnels can be conducted with actual cyclists or full-scale and scaled-down models immersed in an air stream at well controlled velocity. This simulated cyclist wind tunnel flow is generally different from the flow around the rider in the field as a result of, among others, the presence of model supports, a static wind tunnel floor boundary layer (in the absence of a rolling floor) and low freestream turbulence levels.

The forces and moments acting on the wind tunnel model are often measured with a six-component force balance (e.g. Zdravkovich 1990) with a high precision (up to 0.0003% of the full scale load, Tropea et al. 2007). Force balance measurements, however, are 'blind' in the sense that they do not provide insights into the flow behavior and the phenomena responsible for the drag generation. As a result the aerodynamic drag is typically reduced through an iterative process of trial and error variations of cyclist configurations.

More recently, the flow around a cyclist has been examined. Crouch et al. (2014) scanned the wake with a pressure probe (Figure 1.6-left) to understand the relation between the aerodynamic drag and the time-average wake topology (see Section 2.3.2 for a more detailed discussion). The same technique was used to relate differences in the cyclist drag coefficient, as a result of changing posture, to changes in time-average wake velocity deficit and turbulence intensity distribution (Barry et al. 2014). Using pressure probes, the wake of the cyclist is mapped at relative large distance to the model to avoid regions of reverse flow and with a velocity direction deviating more than 45^{o} from the probe's principal axis.

In addition to pressure measurements in the wake, pressure taps have been integrated into cyclist model surfaces to investigate the distribution of the time-average pressure and, in addition, the dynamics of the instantaneous surface pressure (e.g. Crouch 2013; Figure 1.6-middle). A spatial distribution of the surface pressure over the relevant model surfaces can provide valuable information about the pressure drag acting on the model (D'Auteuil et al. 2012; Crouch et al. 2014). In addition, China clay and oil flow visualizations have provided complementary qualitative descriptions of the near-surface flow rendering the direction of streamlines and flow separations and reattachments (e.g. Brownlie et al 2009; Figure 1.6-right). Finally, a general description of the cyclist near-wake is given by Jux et al. (2018; see Section 1.5). The latter work, however, does not discuss the separated and reverse flow near-wake regions in detail, which are responsible for a large portion of the overall aerodynamic drag.

1.4.3 Numerical simulations

The use computational fluid dynamics (CFD) for sport aerodynamic investigations has increased over the past two decades to model the flow field around the cyclist (Hanna 2002). CFD investigations help, among others, to distinguish between the friction and pressure forces and to separate the loads acting on individual cyclist limbs from that of the entire body (e.g. Defraeye et al. 2011; Griffith et al. 2014). After comparing the results of steady Reynolds Average Navier-Stokes (RANS) simulations, in combination with the shear-stress (SST) $k-\omega$ model, and large-eddy simulations (LES) to wind tunnel experimental data, it was demonstrated, that the latter approach resolved the flow in the wake of the cyclist to a higher degree of accuracy (Griffith et al. 2014). RANS, however, being computationally an order of magnitude less expensive than LES, is most commonly used in the field of cycling aerodynamics (e.g. Defraeye et al. 2010; Blocken et al. 2018b). Despite the growing use of CFD and in particular RANS simulations, the level of accuracy implied such modelling makes experimental validation of results essential. For this purpose, the whole-field measurement capability of PIV has proven valuable for CFD validation in other fields (e.g. Ford et al. 2008) along with cycling aerodynamic research.

1.5 PIV in cycling aerodynamic research

The flow around bluff geometries features relatively large reverse flow regions, bounded by separated shear layers, as a consequence of early flow separation (discussed in more detail in Chapter 2). In order to investigate such topology experimentally, the technique of digital particle image velocimetry (digital PIV; Willert and Gharib 1991) can be employed (herein simply referred to as PIV). PIV is an optical, non-intrusive, whole-field flow measurement technique that relies on the motion of tracer particles immersed in the flow, illuminated and imaged, to obtain the fluid velocity. The technique is used in many different areas (e.g. aerodynamics, biology and combustion) to investigate a wide range of topics, such as airfoil performance, the fundamentals of turbulence and blood transport in the human body (Raffel et al. 2018). For PIV in air flows, micrometric oil droplet tracers are most commonly used allowing measurement domains in the order of 0.05 m^2 and 50 cm^3 for planar and volumetric techniques, respectively.

The latter is small in relation to the size of an actual athlete, which may explain why, upon the start of the present study, PIV was not frequently used in cycling aerodynamic investigation. To the best knowledge of the author, only Chabroux et al. (2010) employed PIV in air to characterize the wake of time-trial helmets (see Figure 1.7-left). More recently, and with a similar size of the measurement domain, PIV was conducted in a water channel to characterize the wake of scaled cyclist models (Barry et al. 2016; Crouch et al 2016b).

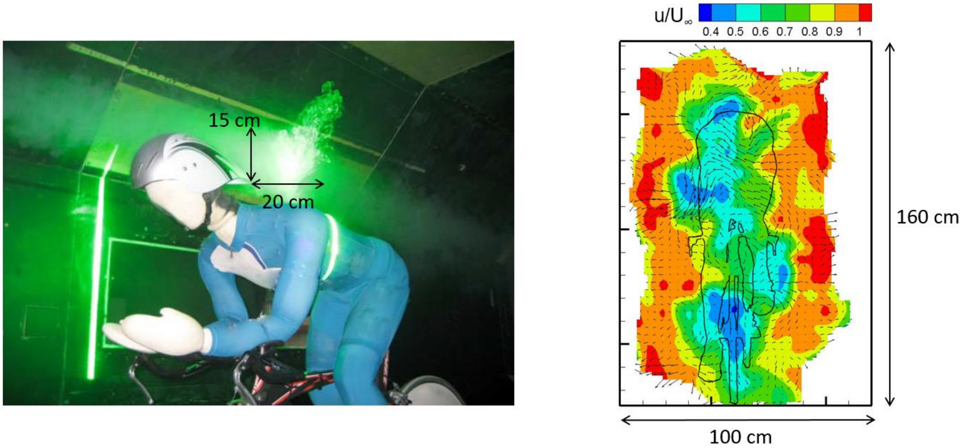

Figure 1.7: PIV measurement downstream of a cyclist: Photo of illumination using micrometric tracers (left; Figure reproduced from Chabroux et al. 2010) and instantaneous velocity field obtained with large-scale PIV using HFSB (right; present work see Section 4.3)

PIV measurements, however, have been achieved at the scale of several square meters (Bosbach et al. 2009; Kühn et al. 2011) using helium-filled soap bubble (HFSB) as tracers (Section 3.4). The HFSB high light scattering efficiency and tracing fidelity in low-speed wind tunnels (Scarano et al. 2015) preluded the first, recent, human-scale PIV measurements in wind tunnels by Jux et al. (2018). The latter authors demonstrated the integration of a compact 3D PIV system (coaxial volumetric velocimery, CVV; Schneiders et al. 2018) onto a robotic arm (robotic volumetric velocimetry; Jux et al. 2018) in order to scan the flow field around a full-scale cyclist mannequin (developed in the present work; Section 4.3). Robotic volumetric PIV allows measurement of the time-average velocity field all around complex geometries (see Section 3.4.2 for more detail), hence, permitting an understanding of the regions of flow separations and reverse flow. This technique is particularly relevant for cycling aerodynamic study and a more detailed discussion is given in Section 3.4.2. In addition to the work of Jux et al. (2018), examples of human-scale PIV are presented in Chapters 4 and 5 of the present dissertation. As an example, Figure 1.7-right depicts the instantaneous velocity field measured in the wake of the aforementioned full-scale cyclist to illustrate the size of the large-scale PIV measurement domain in comparison to that of conventional PIV (left figure).

In addition to these PIV cycling aerodynamics studies in wind tunnels, Spoelstra et al. (2019) have proposed a novel experimental approach to realize PIV measurements in the field for cycling aerodynamic study. The Ring-of-Fire concept was initially conceived by Sciacchitano et al. (2015) and allows measurement of the flow around a cyclist in motion when riding through a cloud of HFSB particles, generated and traced by a PIV system (see Figure 1.8). This new measurement system allows study of the cyclist aerodynamics under more realistic and complex conditions, for example, during acceleration and in peloton formations. The principle of the system's aerodynamic drag evaluation, used by Spoelstra et al., and its uncertainty is established in the present work (Chapter 6).

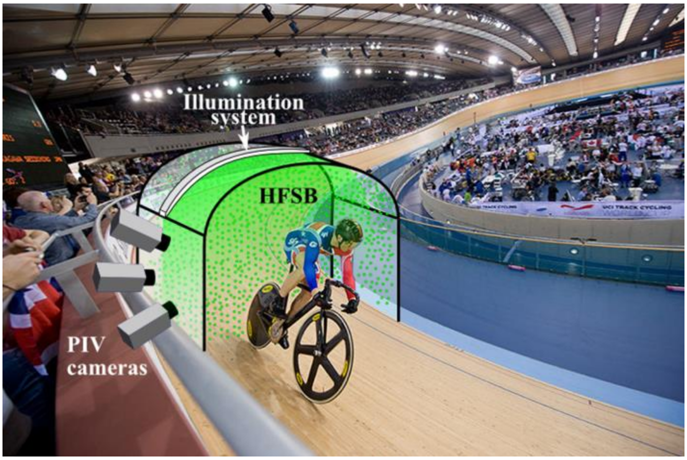

Figure 1.8: Schematic representation of the Ring-of-Fire system for on-site quantitative flow investigation (adapted from Sciacchitano et al. 2015)

1.6 Motivation and objectives

In cycling, relatively little is known about the flow topology in the near-field of the bike-cyclist system and about the flow mechanisms responsible for the generation of drag. PIV promises to be a suitable technique to reveal the three-dimensional flow field around a cyclist. However, its use in cycling aerodynamic research has been rather limited. The latter may be justified by the mismatch between the size of the PIV measurement domain and the human. Hence, at the start of the present work, an upscale of the measurement capabilities seemed necessary for PIV to contribute in cycling aerodynamic research. Furthermore, the relevant advancements of large-scale PIV during the course of the present research, allows mapping regions of separated and reverse flow, which are generally considered the main contributors to the aerodynamic drag. Detailed description and understanding of this cyclist near-wake, therefore, may lead to further drag reduction in the future. In addition, field PIV measurements allow quantitative flow visualization of the complex real-world cyclist airflow, which is practically infeasible in wind tunnels (e.g. model accelerations and curved-linear trajectories). This Ring-of-Fire system allows measurement of the cyclist's aerodynamic drag and at the same time relates it to the flow behavior and the phenomena responsible for its generation. Altogether, the application of large-scale PIV allows extension of the general description of cycling aerodynamics.

Objectives

The aim of the current study is to apply large-scale PIV for the purpose of cycling aerodynamic investigation and drag determination. The specific objectives are threefold:

- Realise experiments at the human scale by PIV inside a wind tunnel to study the flow behaviour around a cyclist and relate it to the aerodynamic drag at the relevant scale and Reynolds number.
- Obtain a general description of the flow behaviour in relation to the transition process driving the extent of flow separation over the cyclist body.
- Study the feasibility to develop the concept of the Ring-of-Fire for cyclist drag determination and quantitative flow visualization in the field.

1.7 Thesis outline

This dissertation is structured as follows:

- Chapter 2 provides the background of bluff body aerodynamics, evolving from simplified geometries towards cyclist flow. The former focuses on the Reynolds number effects of circular cylinders and spheres, which are somehow similar to those of the cyclist limbs (Chapter 5). The discussion concentrates on flow separation, reverse flow regions and the turbulent wake.
- Chapter 3 is dedicated to PIV, its working principle and the different approaches to perform large-scale experiments using HFSB seeding. An overview is provided of relevant PIV data processing techniques and, finally, Section 3.5 presents a framework for load determination from velocity fields around bluff bodies.
- Chapter 4 presents the first full-scale cyclist measurements with a PIV wake rake in a wind tunnel to quantify the aerodynamic drag. The discussion covers the technical developments needed for the experiments, such as in-house built HFSB seeders and a full-scale replica of an elite cyclist, specifically manufactured for the present research. Finally, Section 4.5 gives a detailed discussion of the principle and procedures used to estimate the accuracy of drag evaluation from PIV wake rakes.
- Chapter 5 describes the use of robotic volumetric PIV for the investigation of the cyclist Reynold number effects. The near-wake topology is related to the aerodynamic drag to investigate the distribution of the drag crisis phenomenon and the critical flow regime around the rider.
- Chapter 6 is dedicated to the foundations of the Ring-of-Fire's working principle. Experiments conducted at smaller scale identify the main capabilities of the approach and estimate the experimental uncertainties of the method.

- Chapter 7 summarizes the findings of the present work and provides recommendations for future applications of large-scale PIV in cycling.

2

BLUFF BODY AERODYNAMICS

The flow around the bluff body of a cyclist is complex due to the three-dimensional nature of the human geometry and the motion and deformation of its limbs. This chapter first introduces the main features of bluff body flows, such as separation and trailing vortices. The discussion is deepened on the topic of bluff body flow regimes, governed by the laminar to turbulent transition process, the aerodynamic drag and its variation with Reynolds number, also known as the drag crisis. The chapter finally concludes by describing the main flow properties of a full cyclist.

2.1 Cylinder and sphere flow

The description of the flow around isolated circular cylinders and spheres are two of the canonical fluid mechanical problems. A description of the flow around these two bluff geometries is presented first, considering the cylinder in a cross-flow orientation. Afterwards, other cases of cylinder flow are discussed.

2.1.1 Flow regimes

The flow past circular cylinders and spheres is generally described by a single governing parameter, the Reynolds number (*Re*; e.g. Zdravkovich 1997), representing the ratio of inertial to viscous forces:

$$Re = \frac{dU_\infty}{\nu} \qquad 2.1$$

where U_∞ is the relative velocity between the object and the fluid, generally referred to as the freestream velocity, d is the diameter of the object and ν is the kinematic viscosity of the fluid. Despite the geometrical differences between a circular cylinder, hereafter simply referred to as cylinder, and a sphere, the flow around these objects presents some similarities. In particular, the role of turbulent transition process with increasing Reynolds number and the corresponding division into flow regimes can be considered the same, as will be illustrated in the present and the next section. Hence, these flows are discussed here as one, unless specifically mentioned otherwise.

At very low Reynolds numbers ($Re < 5$), a fully laminar and attached flow is observed (see Figure 2.1-top-left). Increasing the Reynolds number ($5 < Re < 40$), the laminar separation occurs as a steady flow feature over the rear part of the body along with the formation of a pair of counter rotating vortices. For $Re > 40$, the cylinder flow becomes unsteady featuring vortices that are alternately shed from the two sides of the cylinder, resulting in the typical *Von Kármán vortex street*. Only in the critical regime, which is discussed in more detail hereafter, this vortex street and the corresponding vortex shedding frequency, is interrupted. The flow around the sphere becomes unsteady at approximately $Re = 130$ featuring a street of hairpin vortices (Figure 2.1-right). Laminar unsteady spherical flow may be further classified into four sub-regimes, which have been omitted here for reasons of conciseness (for details see Sakamoto and Hanui 1990).

The higher Reynolds number flow regimes are characterized by the laminar to turbulent transition process, which first establishes in the shed vortices, forming a turbulent vortex street (Figure 2.1-fourth row). With increasing Reynolds number, this transition process moves upstream eventually settling in the attached boundary layer on the object’s upstream surface ($Re > 5\times10^6$). The turbulent flow regimes, being relevant to the present work, are discussed here in some detail. For a more complete overview, also including the laminar regimes, the reader may look into the work of Zdravkovich (1997), among others. Furthermore, note that in addition

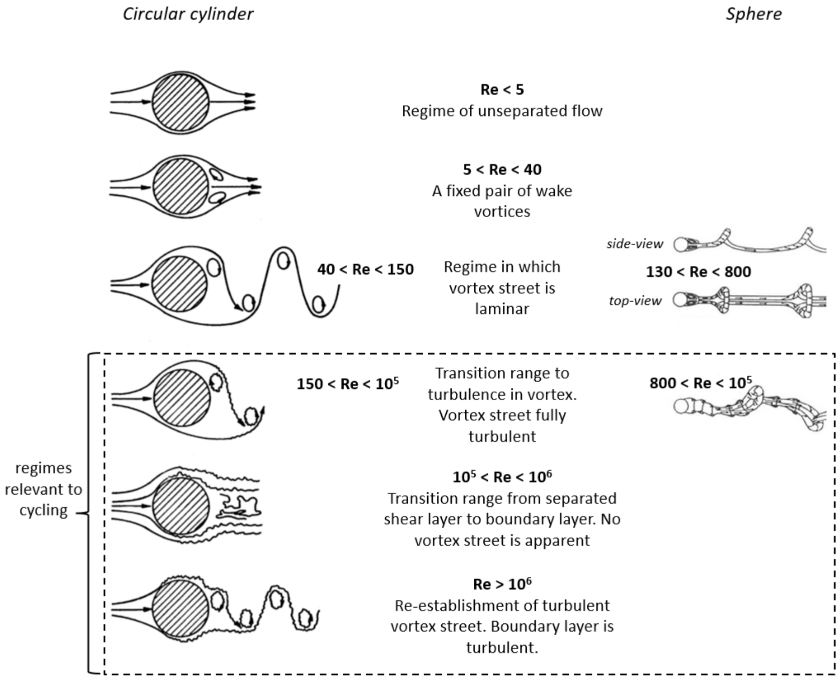

Figure 2.1: Flow regimes of cylinders (left; reproduced from Lienhard 1966) and spheres (right; reproduced from Sakamoto and Hanui 1990). The Reynolds numbers, marking the regime boundaries, are representative for a smooth flow and object.

to the Reynolds number, other parameters, such as surface roughness and freestream turbulence, may govern the flow around cylinders and spheres. The laminar to turbulent transition process, in particular, is susceptible to these so-called *influencing parameters* and it is generally anticipated by increasing freestream turbulence and surface roughness. As a consequence, the bluff body flow regimes depicted in Figure 2.1, representing a fully smooth flow and object surface, may occur at lower Reynolds numbers.

2.1.2 Flow regimes relevant to cycling

The Reynolds numbers relevant to cycling are mostly within $10^4 < Re < 10^6$ ($Re \sim 10^4$ for a 23 mm wide tube moving at 10 m/s; Re approaches 10^6 for a rider's torso of 60 cm at 20 m/s). The corresponding relevant regimes, marked in Figure 2.1, are discussed in this section. The regime occurring at $Re > 10^6$ is considered here, despite being out of the relevant Re-range, since it may occur at increased levels of surface roughness and freestream turbulence.

Below $Re = 10^5$ the flow regime is referred to as *sub-critical* featuring a laminar boundary layer separating from the upstream part of the model surface and developing a wide and turbulent wake. Within this regime the transition to turbulence, takes place in the free shear layers, and moves upstream towards the model surface at increasing Reynolds number. The unsteady turbulent wake is characterized by large coherent vortical structures (Figure 2.2) formed by a roll-up of the turbulent shear layers. In the cylinder wake (right figure) the aforementioned turbulent *Von Kármán vortex street* is established.

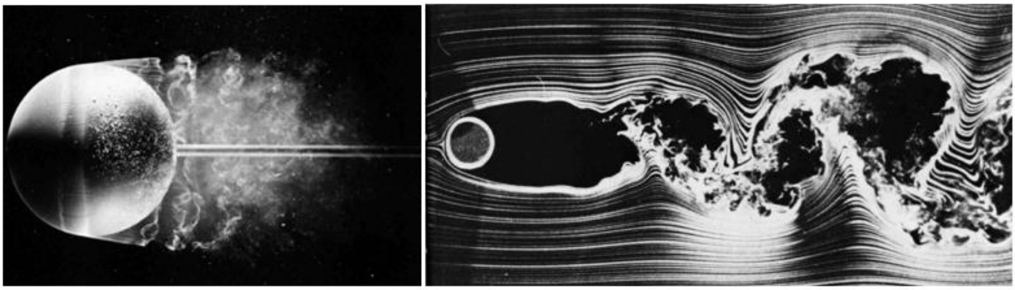

Figure 2.2: Visualization of the instantaneous flow topology over a sphere (right; *Re* = 15,000) and a circular cylinder (right; *Re* = 10,000). Photos adapted from Van Dyke (1982).

In the *critical* regime ($10^5 < Re < 5 \times 10^5$), the free shear layer undergoes transition to turbulence shortly after separation and, as a consequence, is able to reattach on the model surface, forming a so called laminar separation bubble (LSB; e.g. Lehmkuhl et al. 2014). The now turbulent boundary layer finally separates on the downstream facing surface of the model, resulting in a narrower wake. The onset of the critical regime is typically defined as the point where the aerodynamic drag starts declining by increasing Reynolds number. At its endpoint, the drag coefficient reaches a minimum, which defines the critical Reynolds number, Re_{crit} or critical flow condition (Roshko 1961; Schewe 1983).

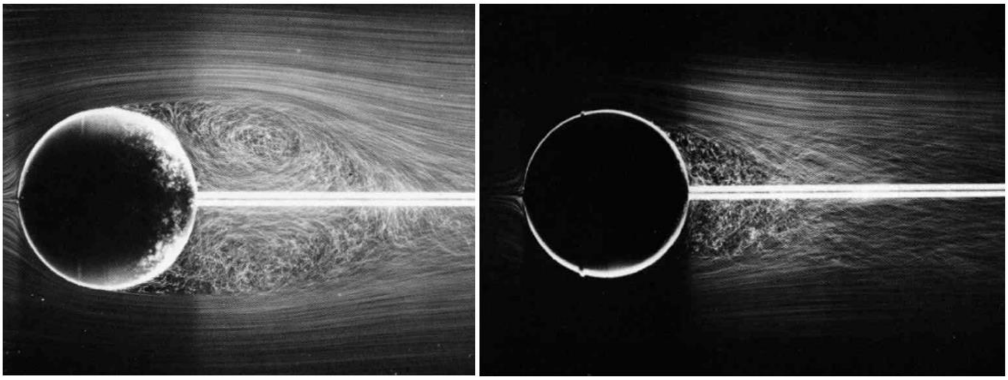

Figure 2.3: Time-average flow around a sphere in sub-critical (bottom-left; *Re* = 15,000) and super-critical condition (bottom-right; tripped at *Re* = 30,000); Photos adapted from Van Dyke (1982).

In the *super-critical* regime ($Re > 5 \times 10^5$), the turbulent transition slowly moves further upstream decreasing the size of the LSB. The point of flow separation and the corresponding drag coefficient remain approximately unaltered. In this regime, the wake is relatively narrow in comparison to that in the sub-critical regime, which is clearly observed comparing the corresponding time-average sphere flow visualization depicted in Figure 2.3 and the schematic description in Figure 2.4. In addition to the wake width, also the downstream stagnation point, marking the end of the reverse flow or recirculation region, formed in the wake, is closer to the model. Note, that in Figure 2.1 the division into the critical and super-critical regime has been omitted and these two are depicted as one ($10^5 < Re < 10^6$).

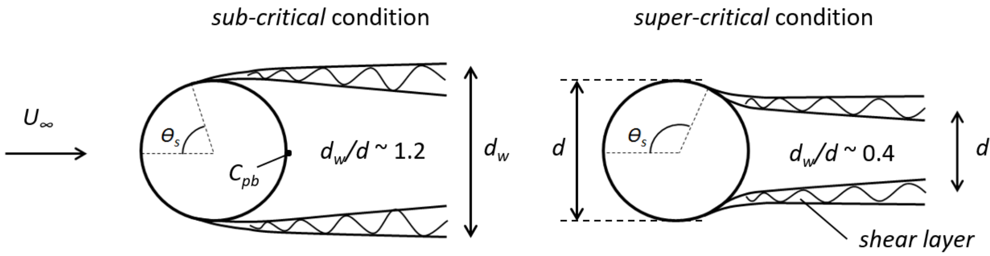

Figure 2.4: Schematic description of a bluff body wake in the *sub-critical* and early *super-critical* regime

At $Re > 10^6$, the LSB has disappeared and the turbulent transition occurs in attached boundary layer moving upstream at increasing *Re*. Consequently, the wake widens and the drag coefficient increases. This regime is referred to as, among others, post-critical (Achenbach 1971) and trans-critical (Zdravkovich 1997; Lehmkuhl et al. 2014).

Separation angle

In the sub-critical regime the flow separation angle, θ_s (see Figure 2.4) over cylinders and spheres is relatively constant at approximately 80° (Figure 2.5). Within the critical regime, θ_s increases significantly to approximately 140° and 120° for the cylinder and sphere, respectively. For cylinder flow, the separation angle drops sharply to about 115 ° at approximately $Re = 10^6$. A less significant, but clear, drop is observed around the same Reynolds number for the flow over the sphere.

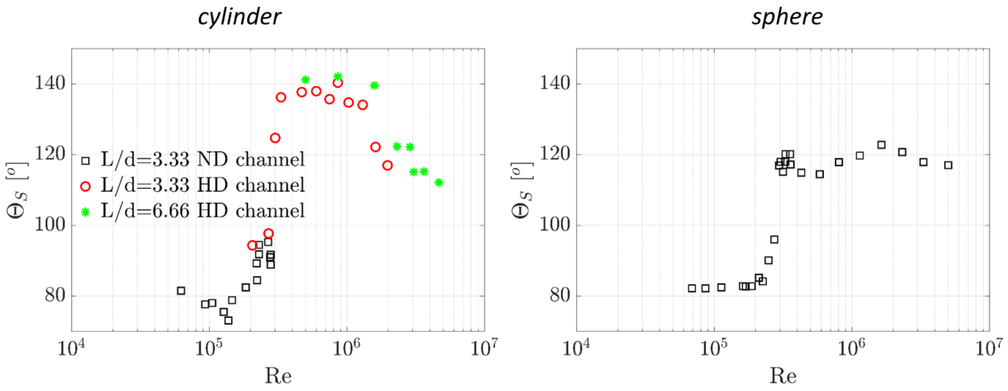

Figure 2.5: Separation angle vs. Reynolds number for a cylinder (left; reproduced from Achenbach 1968) and a sphere (right; reproduced from Achenbach 1972).

Pressure distribution

The pressure is expressed in non-dimensional form by the pressure coefficient:

$$C_p = \frac{p - p_\infty}{0.5\rho U_\infty^2} \qquad 2.2$$

where p_∞ is the freestream pressure. The distribution of the surface pressure coefficient with increasing azimuth angle θ is depicted in Figure 2.6. At the front stagnation point ($\theta = 0^o$) the pressure coefficient equals 1. Further downstream the pressure drops as a consequence of the flow acceleration. This negative pressure gradient stabilizes the boundary layer that remains attached. After a local minimum (sub-critical: $C_p \sim 1.2$ at $\theta \sim 60^o$), the pressure starts rising and, because of this adverse pressure gradient, the boundary layer separates shortly after ($\theta \sim 80^o$). After separation the pressure remains approximately constant until $\theta = 180^o$.

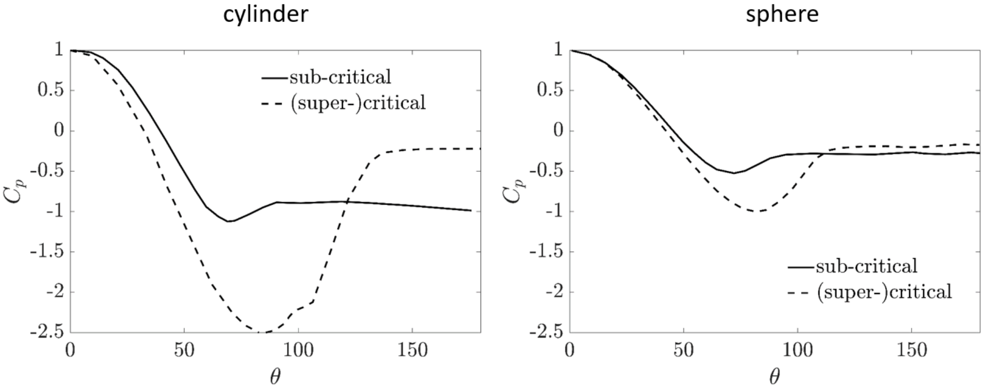

Figure 2.6: Distribution of the pressure coefficient over a cylinder (left; $Re = 6.5 \times 10^5$; Figure adapted from Lehmkuhl et al. 2014) and a sphere (right; $Re = 10^5$; Figure adapted from Constantinescu and Squires 2004).

As a consequence of the delayed separation in the late critical and super-critical regime, the negative pressure peak moves downstream to $\theta \sim 80^o$ (Figure 2.6). In addition, the pressure recovery in the super-critical regime is substantially stronger resulting in a higher base pressure, p_b and, hence, a smaller aerodynamic drag (discussed in next sub-section).

The negative base pressure coefficient is depicted in Figure 2.7 in the range of $10^4 < Re < 10^7$. In the sub-critical regime the base pressure is relatively constant to $C_{pb} = -1.2$ and $C_{pb} = -0.3$ for the cylinder and sphere, respectively (note that in the figure the negative coefficient is reported $-C_{pb}$. Higher values correspond to stronger suction viz. higher drag). Because of the delayed separation along the critical regime, the base pressure coefficient drops by a factor 6 for both bluff geometries. In the super-critical regime, a monotonic increase is observed.

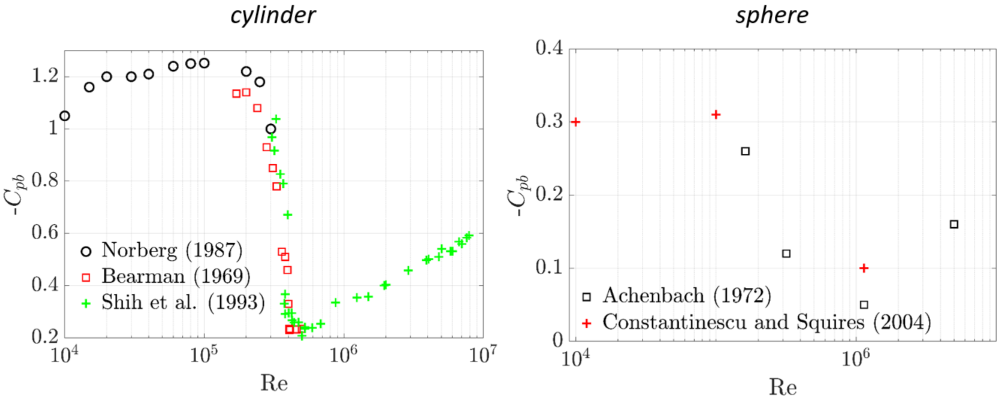

Figure 2.7: Base pressure coefficient vs. Reynolds number for a cylinder (left; Figure composed from Norberg 1987, Bearman 1969 and Shih et al. 1993) and a sphere (right; Figure composed from Achenbach 1972 and Constantinescu and Squires 2004).

Drag coefficient

The aerodynamic drag is expressed in non-dimensional form by the drag coefficient:

$$C_D = \frac{D}{0.5\rho U^2 A} \tag{2.3}$$

The drag coefficient of a cylinder exceeds that of the sphere in all three regimes (see Figure 2.8). Instead, these two bluff bodies exhibit drag variations of the same relative magnitude and occur approximately at the same Reynolds numbers. In both cases the drag coefficient drops by a factor 6 from a sub-critical value, $C_{D,sub}$ to a critical drag coefficient $C_{D,crit}$ within $10^5 < Re < 5 \times 10^5$. After the critical regime, C_D remains relatively constant in super-critical conditions and slowly increases, thereafter, to a value of approximately 0.5 $C_{D,sub}$ at $\mathrm{Re} = 5 \times 10^6$. The strong

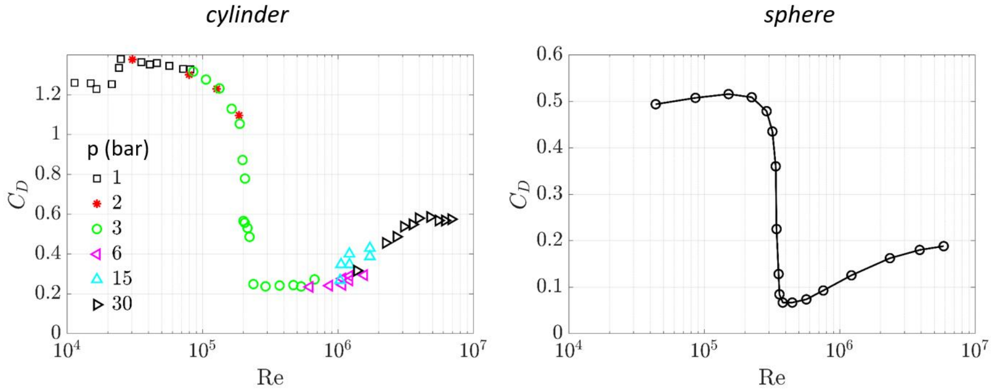

Figure 2.8: Drag coefficient vs. Reynolds number for a cylinder (left; Schewe 1983) and a sphere (right; Achenbach 1972).

drag coefficient reduction and subsequent increase is typically referred to as the *drag crisis* (e.g. Constantinescu and Squires 2004, Lehmkuhl et al. 2014, Zdravkovich 1997) as discussed earlier in Section 1.3.

Equation 1.2 expresses the aerodynamic drag as the sum of the pressure and the friction drag. Similarly, the drag coefficient is expressed in a pressure and a friction coefficient, C_{DP} and C_{DF}, respectively:

$$C_D = C_{DP} + C_{DF} \tag{2.4}$$

Along all regimes, the pressure drag dominates the overall aerodynamic drag of cylinders and spheres. The contribution of the friction drag remains relatively small: its contribution to the total drag peaks at the end of the critical regime because of the pressure drag minimum: $C_{DF}/C_D \sim 0.025$ for cylinders (Achenbach 1968) and $C_{DF}/C_D \sim 0.15$ for spheres (Achenbach 1972). In the sub-critical regime, values below 0.01 and 0.02 are attained, respectively.

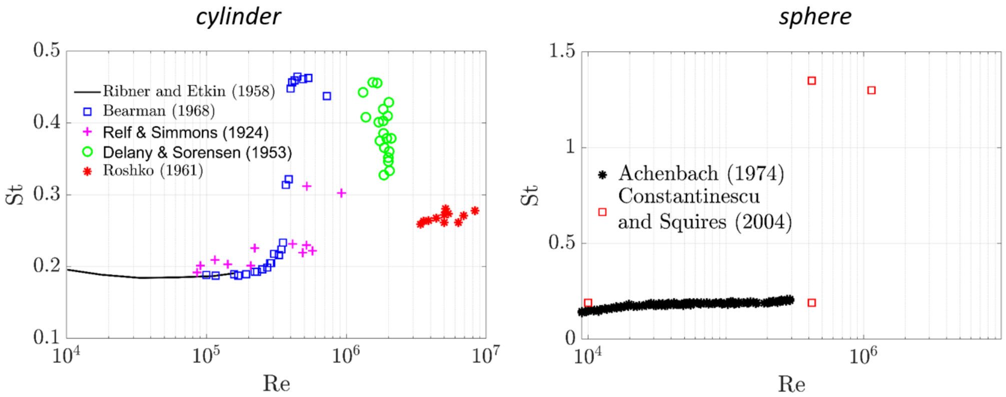

Figure 2.9: Strouhal number vs. Reynolds number for a cylinder (left; Adapted from Bearman 1969) and a sphere (right; composed from Achenbach 1974 and Constantinescu and Squires 2004).

Vortex shedding

The shear layers that separate from the cylinder and sphere surface roll up into coherent vortical structures and are responsible for the formation of the aforementioned vortex streets. This vortex shedding process typically features a distinct shedding frequency *f*, which is expressed in non-dimensional form by the Strouhal number, *St:*

$$St = \frac{fd}{U_\infty} \tag{2.5}$$

Figure 2.9 depicts the Strouhal number, obtained from different works in literature, in the range of $10^4 < Re < 10^7$. In the sub-critical regime, the Strouhal number is approximately 0.2 and increases to 0.45 and 1.35 for cylinders and spheres, respectively, within the critical regime. After the super-critical regime, it drops to 0.25 for cylinders, while for spheres a particular shedding mechanism disappears.

Time-average near-wake flow topology

The cylinder and sphere near-wake flow topology, inspected along a streamwise symmetry plane, feature similar characteristics. The flow accelerates around the forebody and, at some point, separates from the surface, resulting in a large reverse flow or recirculation region featuring two counter rotating vortices (Figure 2.10 top-left). The downstream stagnation point *S*, located on the streamwise symmetry axis, marks the end of the recirculation region. The maximum reverse flow velocity occurs at the streamwise symmetry axis shortly downstream of the object's trailing edge (Figure 2.10 bottom-left). The wake features two branches of peak streamwise velocity fluctuations (Figure 2.10 bottom-right). For the flow around the sphere, the wake is axis-symmetric generally featuring a radial inward motion towards the flow model's principal axis (Figure 2.10 top-right). In addition to the qualitative discussion above, Table 2.1 provides an overview of the wake characteristics in sub- and super-critical conditions for cylinders and spheres. The parameters in the table have been selected to accommodate the comparison of the observed Reynolds number effects in the wake of the cyclist's limbs (Section 5.4.2) and the measured velocity downstream of a transiting sphere (Section 6.4.2).

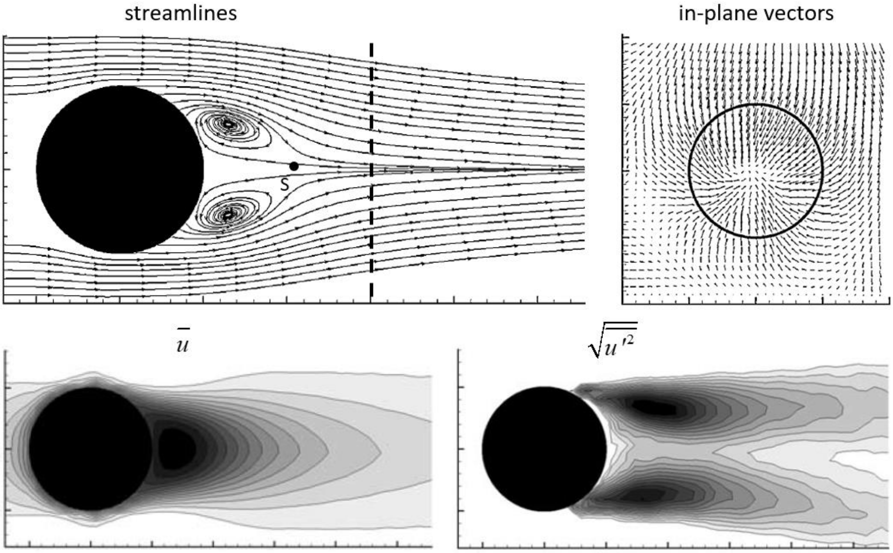

Figure 2.10: Time-average flow topology around a sphere: streamlines (top-left), in-plane vectors at $x/d = 1.5$ (top-right), contours of streamwise velocity (bottom-left; dark colours indicate low values) and streamwise velocity fluctuations (bottom-right; dark colours indicate high values). The dashed line in the top-left figure marks the position of the plane depicted at the top-right. Figures have been reproduced from Jang and Lee (2008).

Table 2.1: Near-wake flow characteristics of circular cylinders and spheres in different regimes.

Circular cylinder			center of recirculation	max reverse velocity ($\bar{u}/U_\infty$)		max ($\sqrt{\overline{u'^2}}/U_\infty$	
	Re	L/d	Position (x/d, r/d)	value	position (x/d)	value	position (x/d, r/d)
Sub-critical							
Norberg (1998) LDV	10,000	1.51		-0.4	1.0		
McClure and Yarusevych (2016) (PIV)	12,000	1.5		-0.3	1.0	0.5	1.1±0.5
Chopra and Mittal (2017) (stabilized finite element)	50,000	1.0	0.7 ± 0.3				
Yeon et al. (2016)	125,000	1.05	0.75± 0.3				
Critical							
Capone et al. (2016) (PIV)	125,000	1.45	1.1 ± 0.3			0.35	1.1±0.5
Rodriguez et al. (2015) (LES)	250,000	1.06	0.71± 0.3				1.0±0.45
Chopra and Mittal (2017) (stabilized finite element)	350,000	0.9	0.7 ± 0.15				
Super-critical							
Rodriguez et al. (2015) (LES)	850,000	1.1	0.82± 0.13	-0.23			1.2±0.2
Yeon et al. (2016) (LES)	757,000	1.15	0.75± 0.15				

Sphere			center of recirculation	max reverse velocity ($\bar{u}/U_\infty$)		max ($\sqrt{\overline{u'^2}}/U_\infty$	
	Re	L/d	Position (x/d, r/d)	value	position (x/d)	value	Position (x/d, r/d)
Sub-critical							
Jang and Lee (2008) (PIV)	11,000	1.05	0.75 ± 0.25		0.7	0.65	1.0±0.3
Constantinescu and Squires (2003) (LES)	10,000	2.2	1.22 ± 0.41	-0.40	1.41	0.23	1.8±0.46
Ozgoren et al. (2011) (PIV)	10,000	1.4	0.7±0.4				
Bakić et al. (2006) (LDV)	51,500	1.5		-0.43	1.0		
Yun et al. (2006) (LES)	10,000	1.86				0.25	1.5±0.45
Critical							
Jux et al. (2019) (PIV)	100,000	1.3	0.7 ± 0.35	-0.4	0.7		
Super-critical							
Constantinescu and Squires (2004) (LES)	1,040,000	1.1				0.32	0.9±0.3

Pressure minima in instantaneous snapshots of the wake of cylinders and spheres coincide with the location of the unsteady vortex structures shed from the bodies' surface (e.g. McClure and Yarusevych 2016). The alternating shedding mechanism of cylinder flow results in a time-average pressure distribution depicting a single area of minimum pressure located on the symmetry axis (Figure 2.11-left; McClure and Yarusevych 2016). In contrast, the vortex rings that emanate from spheres result in a time-average annular pressure minimum. Hence, when this is inspected along a streamwise symmetry plane, it is observed as two pressure minima (Figure 2.11-right; Jux et al. 2019).

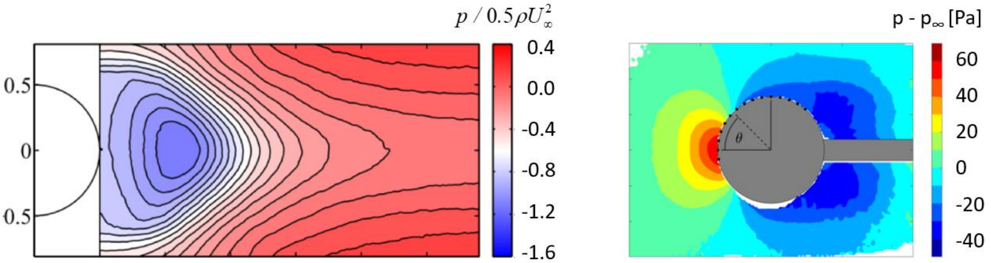

Figure 2.11: Contours of time-average static pressure around a cylinder (left; adopted from McClure and Yarusevych 2016) and a sphere (right; adopted from Jux et al. 2019).

2.2 Other cylinder flow resembling cyclist limbs

The flow around an isolated circular cylinder flow is somehow similar to that around the cyclist limbs. In contrast to a cylinder in cross-flow, however, these limbs are generally not in cross-flow, they have a finite length and the flow around them is affected by nearby body parts. Hence, this section focuses on several cases of cylinder flow that may better resemble the aforementioned conditions.

2.2.1 Inclined cylinders

A two-dimensional approximation, that ignores the velocity component parallel to the cylinder's main axis, is commonly used to estimate, among others, the forces acting on inclined cylinders (e.g. Zdravkovich 2003). This *Independence Principle* (IP) assumes that the aerodynamic drag, among others, scales with the flow velocity normal to the cylinder, so with cos α, where α is the angle between the direction of freestream velocity and cylinder longitudinal axis. At low Reynolds number (Re ~ 1000) the IP assumption is generally valid for $\alpha < 60^o$.

At higher Reynolds number, instead, the maximum angle at which the IP applies is smaller. A few examples are given hereafter. Firstly, at $Re = 1.4\times10^4$, the surface pressure distribution of inclined cylinders, normalized by the normal component of freestream velocity, matches the cosine law well up to $\alpha = 45^o$ (see Figure 2.12; Wang et al. 2019). At $\alpha = 60^o$, however, it clearly deviates from it. Secondly, the typical cylinder vortex street is clearly observed below $\alpha = 30^o$.

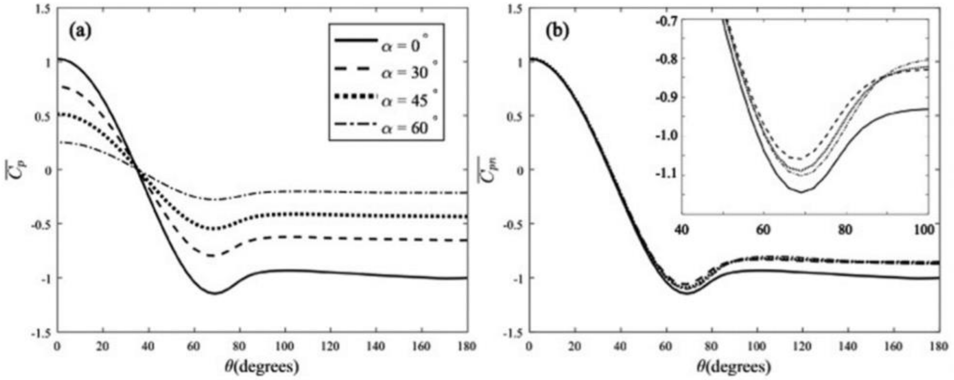

Figure 2.12: Time-average surface pressure coefficient of inclined cylinders ($Re = 1.4\times10^4$) normalized by freestream velocity (left) and by the normal component of freestream velocity (right). Figure reproduced from Wang et al. (2019).

Instead, at larger inclination it is replaced by a steady trailing vortex pattern (Wang et al. 2019; Yeo and Jones 2008). Thirdly, the length of the recirculation region in the cylinder's wake increases at small inclinations ($\alpha < 30^{o}$; Figure 2.13). It seems to remain approximately constant, however, for $\alpha > 30^{o}$. Finally, the trend of the aerodynamic drag, normalized by the normal component of the freestream, remains within a few percent of the IP predicted value below $\alpha = 30^{o}$. Instead, it departs from the IP at larger angles reaching a discrepancy of about 50% at $\alpha = 60^{o}$. The aforementioned deviations with respect to the IP are attributed to the flow component parallel to the cylinder's longitudinal axis, which is not considered by the model, and which seems to play a role especially at the larger inclination.

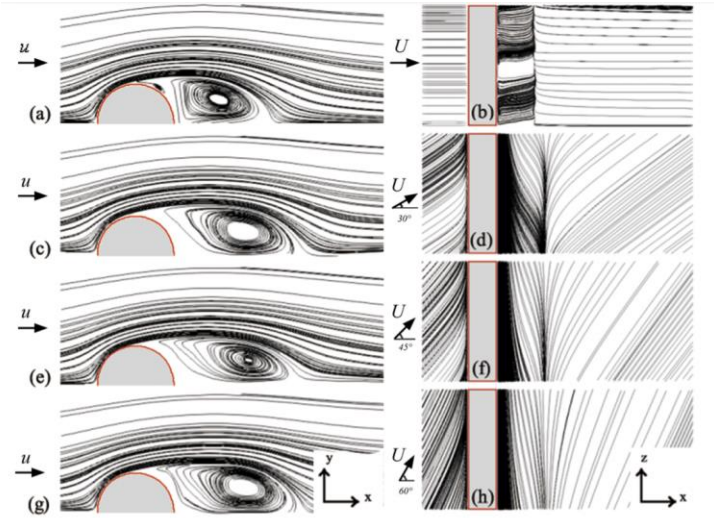

Figure 2.13: Streamlines around a cylinder at different inclination angles. Figure reproduced from Wang et al. (2019).

In the critical flow regime, the cylinder aerodynamic drag cannot be determined only by the normal component of the velocity (Bursnall and Loftin 1951). The super-critical drag coefficient, for example, of a cylinder at a yaw angle of $\alpha = 30^{\circ}$ exceeds that of a cylinder in cross-flow by 100%. Also the critical Reynolds number decreases from approximately 5.0×10^{5} to 3.8×10^{5} and 1.5×10^{5} at yaw angles of $\alpha = 30^{\circ}$ and $\alpha = 60^{\circ}$. These larger discrepancies with respect to the IP, in comparison to the sub-critical case, are attributed to the disappearing laminar separation bubble with increasing inclination.

2.2.2 Interference effects between two cylinders

This section discusses the interference effects of two-cylinder arrangements: side-by-side cylinders and tandem cylinders. A description of these arrangements is depicted in Figure 2.14. Zdravkovich (1987), among others, provides an overview of other cylinder arrangements as well.

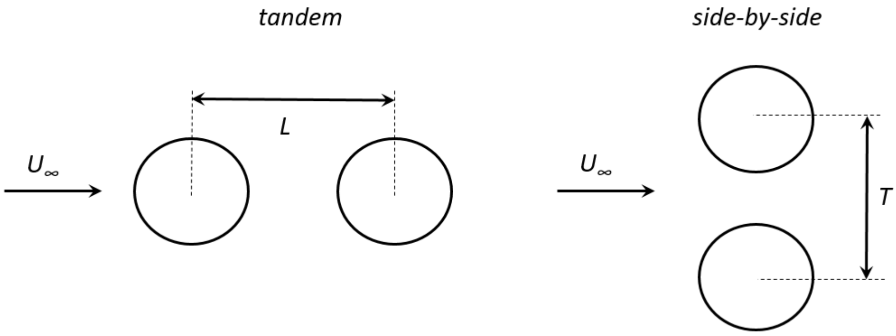

Figure 2.14: Description of two cylinder arrangements

Side-by-side arrangements

The interference effects between two side-by-side cylinders can be categorized into different regimes (Zdravkovich 1987). These regimes, as observed in sub-critical conditions, are illustrated in Figure 2.15 along the vertical axis (marked P-SSA to P-SSC). Along the vertical axis, the spacing, T (Figure 2.14) between the cylinders increases. The first interference regime ($T/d < 1.2$) features a single vortex street with a base bleed through the gap between the cylinders. When increasing the cylinder spacing ($1.2 < T/d < 2.2$), the second, bi-stable regime features one wide and one narrow cylinder wake with a jet flow in between them. The jet bends towards the cylinder with the narrow wake. In the third interference regime ($2.2 < T/d < 4$) the two cylinder wakes are coupled featuring synchronized vortex shedding. Finally, in the fourth regime ($T/d > 4$) the effects of interference are negligible. In all the aforementioned regimes the aerodynamic drag of each of the side-by-side cylinders is approximately equal to that of a single isolated model, except in the second regime. In the latter case ($1.2 < T/d < 2.2$), the drag is reduced by approximately 30%. Finally, in the critical regime (not to be confused with the interference regimes), the drag coefficient of closely spaced cylinders ($T/d < 2.2$) may exceed the value of isolated cylinders by more than 100%. This higher drag coefficient is the consequence of the absence of a laminar separation bubble on the inward side of the cylinders (Okajima and Sugitani 1981).

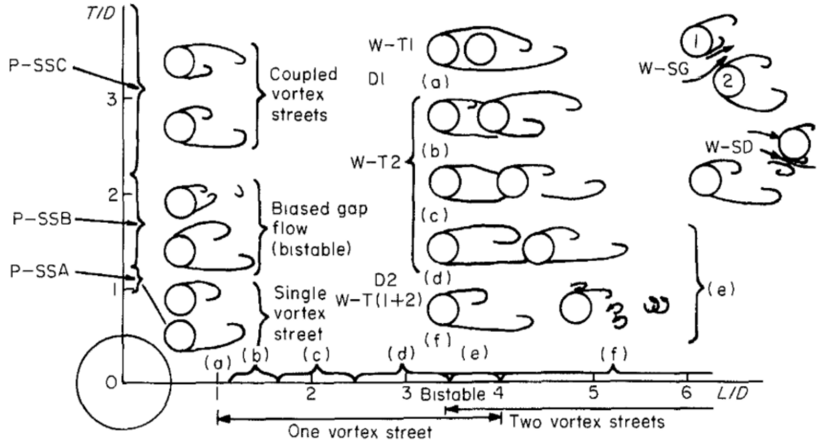

Figure 2.15: Interference flow regimes for two side-by-side, tandem and staggered arrangements of circular cylinders. Figure reproduced from Zdravkovich (1987).

Tandem arrangements

In the sub-critical flow state, three different regimes of interference are distinguished (Zdravkovich 1987), which are illustrated in the middle of Figure 2.15 and are marked W-T1, W-T2 and W-T3. In the first regime ($L/d < 1.5$), the shear layers separated from the leading cylinder do not attach on the trailing one and, hence, the established vortex street results from the shear layers of the former only. In the second regime ($1.5 < L/d < 3.6$) the separated shear layers of the leading cylinder attach on the upstream facing surface of the trailing cylinder and a vortex street is formed only downstream of the second cylinder. In the third regime ($L/d > 3.6$) a vortex street is formed downstream of both cylinders.

The drag coefficient of two tandem cylinders in a Reynolds number range that includes the critical state is depicted in Figure 2.16. The drag crisis, typical for isolated cylinders, is also observed for the leading of the two cylinders. The drag coefficient of the second trailing cylinder, C_{D2} is well below that of the leading one, C_{D1} in the sub-critical regime. In the end of the critical regime, the wake of the first cylinder significantly narrows and, as a result, the drag of the trailing cylinder increases and, paradoxically, exceeds that of the former ($C_{D2} > C_{D1}$). The above findings have been reported for smooth tandem cylinders (Pearcey et al. 1982) and as well for cylinders with rough surfaces (Okajima 1977).

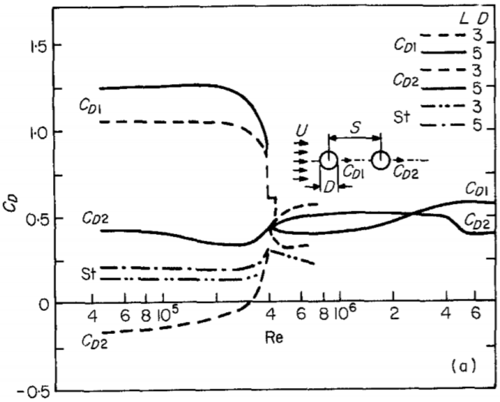

Figure 2.16: Drag coefficient and Strouhal number of two tandem cylinders at different cylinder spacing. Figure reproduced from Zdravkovich (1987) who based it on the findings of Pearcey et al. 1982.

2.2.3 Finite cylinders

The flow around the free end of a cylinder features a streamwise vortex pair resulting from the separation over the cylinder's free-end leading edge (see Figure 2.17). The induced velocity, resulting from the counter rotating vortex pair, injects fluid into the cylinder's wake around its free ends, increasing the pressure over the downstream side of the model. A delayed flow separation towards the free ends is observed as well (marked in Figure 2.17), corresponding to a local decrease of drag coefficient. Therefore, the cylinder's sub-critical drag coefficient decreases with decreasing ratio of cylinder length over cylinder diameter, L_C/d from $C_D = 1.2$ to $C_D \sim 0.7$ for $L_C/d \sim \infty$ and $L_C/d \sim 1$, respectively. Another consequence of the flow topology around the cylinder's free ends is the presence of sub-critical conditions near these free ends in coexistence with super-critical conditions along the cylinder's mid-section (Ayoub and Karamcheti 1982).

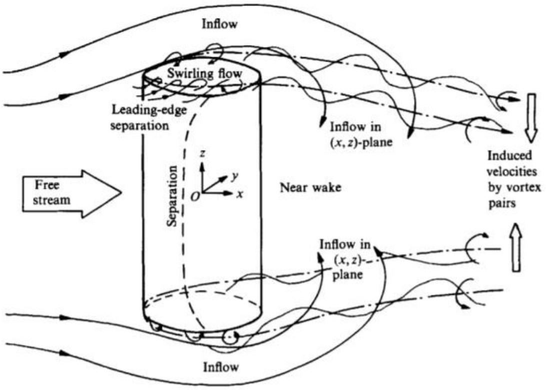

Figure 2.17: Description of the flow around a circular cylinder with two free ends (reproduced from Zdravkovich et al. 1989).

2.2.4 Elliptic cylinders

The fineness ratio, *l/d* defines the cylinder's elliptic cross-sectional shape, where *l* is the length of the cylinder along the streamwise axis. For a fineness ratio of 2, the drag coefficient is approximately 70% of that of the cylinder, the onset of the critical regime is reduced with a factor 2 and the critical Reynolds number increases by a factor 1.4 (Delany and Sorensen 1953). Instead, for a more bluff cross-section of the cylinder, $l/d = 0.5$, the drag coefficient increases to $C_D \sim 1.8$ and the onset of the critical regime is increased well above that of cylinders.

2.3 The flow around the bike and rider

The flow around the cyclist features a wide range of Reynolds numbers, a variety of bluff body flow regimes and interactions between the different bike and body parts, evolving into a complex system of trailing vortices. This section discusses the rider's flow topology along with the characteristic variation of the cyclist aerodynamic drag with changing leg orientation throughout the pedalling cycle.

2.3.1 Cyclist position and geometry

The position of the rider on the bike depends, among others, on the human anthropometrical characteristics in combination with the bike geometry, riding speed and athlete fatigue. Consequently, a variety of rider positions is observed in competition, which is also reflected in cycling aerodynamic research (e.g. Blocken et al. 2018a). Three of the main athlete positions have been depicted in Figure 1.4, illustrating the upright position and two race positions: drops and time-trial position. A typical cyclist race position features an upper body and lower arms that are mostly aligned with the ground (and riding direction). The orientation of the upper arms, instead, is almost orthogonal to the ground, while that of the upper and lower legs changes harmonically in time because of the legs pedalling motion.

When considering a typical race speed, $V_{race} = 15$ m/s, the overall cyclist's torso-based Reynolds number can reach $Re = 6\times10^5$. The Reynolds number of individual cyclist and bike parts, based on the local thickness of the geometry, instead, is generally substantially smaller (e.g. $Re_{ankle} \sim 50{,}000$ and $Re_{spoke} \sim 1{,}000$ based on the corresponding thickness of the object). Hence, the flow around the cyclist features several bluff body flow regimes. A description of the different flow regimes along the rider's limbs is presented in Chapter 5.

2.3.2 Velocity and vorticity topology

The flow around the cyclist features several bluff body flow characteristics. It exhibits large regions of separated flow, among others along the upper arm (separation line depicted in Figure 1.6-right), resulting in a relatively wide wake exhibiting significant velocity deficit (see Figure 2.18). When inspected in a cross-flow plane closely downstream of the saddle, velocity deficit peaks are located behind the lower back and the drive train (Figure 2.18-right). Furthermore, recirculation regions, bounded by two shear layers, are present in the near-wake of the upper arms and legs as will be presented in Chapter 5 (Figure 5.5).

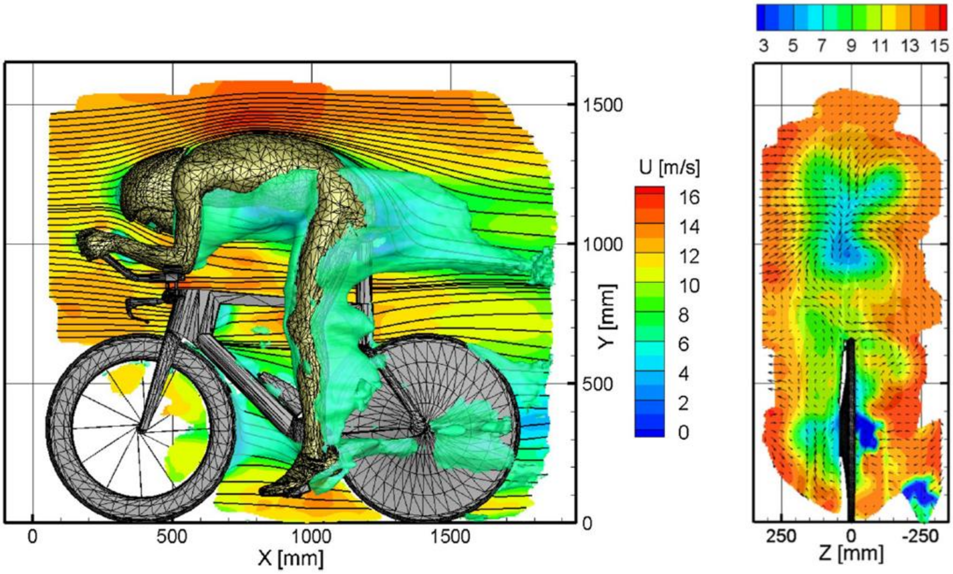

Figure 2.18: Contours of time-average streamwise velocity in the centre plane (*z* = 0; left) and in a plane downstream of the saddle (*x* = 1500 mm; right). Iso-surface of 7 m/s included in the Figure to the left. Figures reproduced from Jux et al. (2018).

In addition to the aforementioned simplified bluff body characteristics, the flow around a cyclist depicts a complex system of streamwise vortical structures that emanate from the different body parts and limb junctions (marked in Figure 2.19). The counter rotating hip/thigh vortex pair is the primary wake structure and is closely correlated to the overall aerodynamic drag of the system (Crouch et al. 2014). The vortex organisation is most clearly observed from the time-average flow topology, although, among others, the primary vortex pair can also be recognized in the instantaneous organisation (Figure 2.19-right). This typical cyclist streamwise vortex topology is observed for different models (e.g. Crouch et al. 2014; Jux et al. 2018; Griffith et al. 2014), at different Reynolds numbers (Crouch et al. 2016b) and in the wake of an individual and drafting cyclist (Barry et al. 2016), which illustrates the robustness of this flow organisation. Instead, the leg position of a rider largely affects the topology and also the corresponding aerodynamic drag (Crouch et al. 2014). The symmetric leg position (upper legs aligned) corresponds to a symmetric wake topology (Figure 2.21 top-left) and a low drag regime (marked in blue in Figure 2.21 bottom) Instead, an asymmetric vortex topology (Figure 2.21 top-right) is observed in the high drag regime (marked in red in Figure 2.21 bottom) corresponding to an asymmetric leg position (one leg stretched and one leg bent).

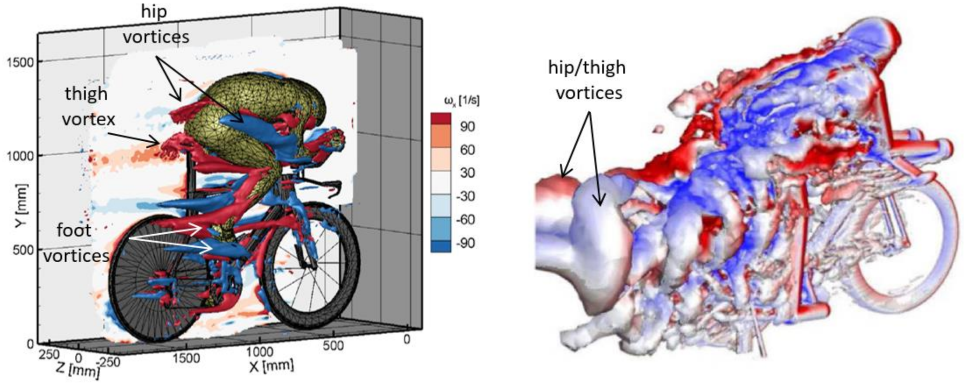

Figure 2.19: Streamwise vortex topology: Iso-surface of time-average vorticity, $\omega_x = \pm 100$ s^{-1} (left; adapted from Jux et al. 2018) and an instantaneous wake snapshot illustrated by iso-surface of q-criterion coloured by cross-stream velocity (blue-negative, red-positive; right) adapted from Griffith et al. (2014).

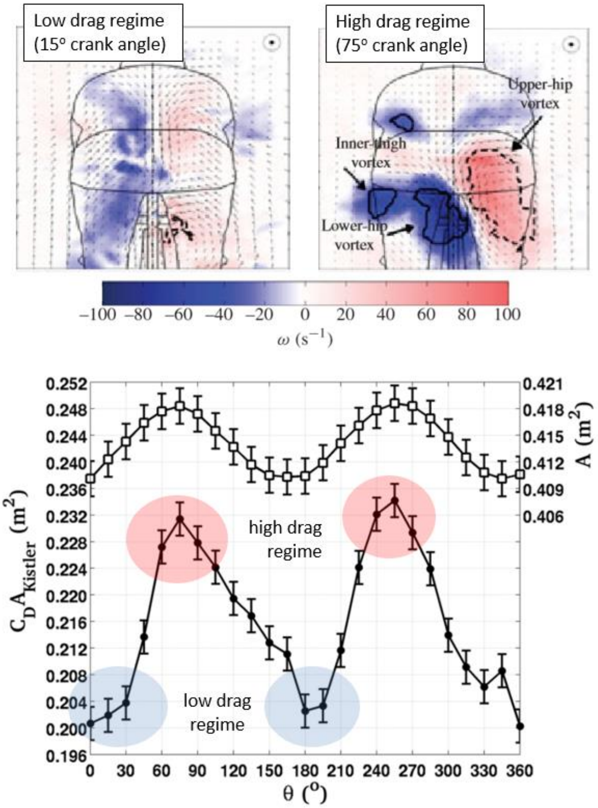

Figure 2.20: Streamwise vortex topology in the low drag regime (top-left) and the high drag regime (top-right) and the corresponding variation of the drag area and frontal area along the crank angle on the left and right axis, respectively (bottom). Figures adapted from Crouch et al. (2014).

2.3.3 Wake velocity fluctuations

A distribution of velocity fluctuations in the wake of the cyclist may provide insight into the distribution of the separated shear layers and the wake width of individual limbs and body parts. Furthermore, when relating the wake width to the drag coefficient (see Figure 2.4), insight into the drag distribution along the cyclist body may be obtained. Crouch et al. (2014) present the turbulence intensity level in the wake of the upper body, in a cross plane downstream of the rear wheel (Figure 2.21). It is observed that the turbulence intensity peaks in an area downstream of the saddle because of the flow separation, among others, over the lower back and upper legs. Similar to the wake vortex topology, the turbulence intensity distribution also changes with changing crank angle and corresponding leg position: Relatively low turbulence levels are observed in the aforementioned low-drag regime, while the high drag regime features higher fluctuations. As a result of turbulent dissipation, individual shear layers, emanating from different body parts, cannot be distinguished from the measurements of Crouch et al. and, so, it is not possible to relate the fluctuation levels to the flow around local parts of the cyclist. For such mapping, measurement closer to the model surface are conducted in the present work (Chapter 5).

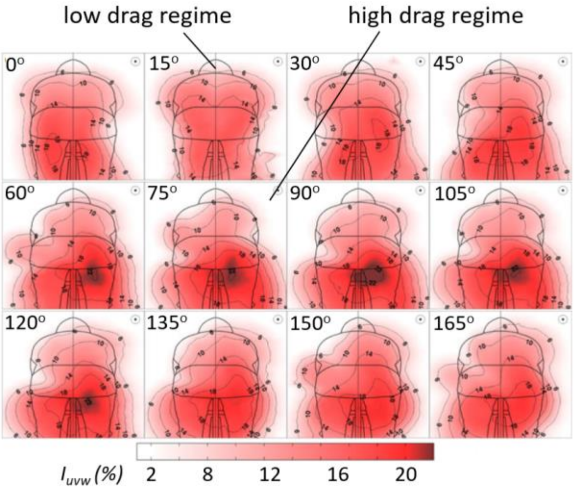

Figure 2.21: Principle turbulence intensity distribution with changing crank angle. Figure adapted from Crouch et al. (2014).

2.3.4 Field and surface pressure

The distribution of the pressure coefficient across a rider in time-trial position highlights an area of high pressure, induced upstream of the rider, and large regions of low pressure over the back, to the left and right of the upper body and downstream of the legs (Figure 2.22-top; Blocken et al. 2013). The latter primarily stems from the accelerating flow around the cyclist and separating over the bluff body limbs. Considering that the overall aerodynamic drag of the cyclist is dominated by the pressure drag, the surface pressure provides valuable information about the distribution of the aerodynamic drag along the rider's body and the bike. As a result of the flow separation over the rider's upper arms and legs, these limbs feature a relatively high negative base pressure (Figure 2.22-bottom), similar to that of isolated cylinder (see Figure 2.6). The flow over the upper back of the cyclist, instead, remains mostly attached and the pressure recovers towards the lower back.

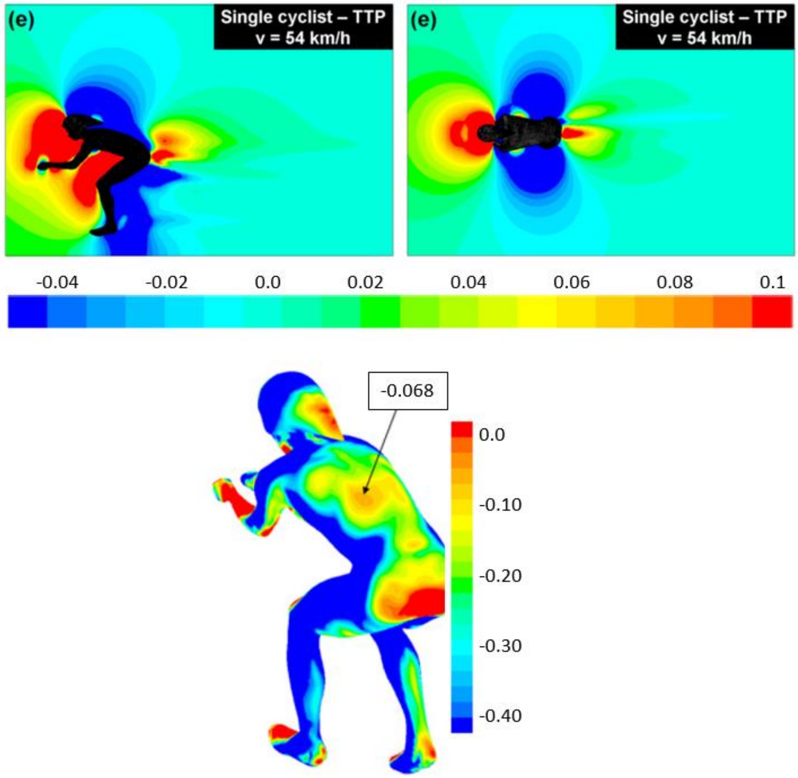

Figure 2.22: Pressure coefficient on the surface of a rider (top) and in the flow across it (bottom). Figures have been adapted from Blocken et al. 2013).

3

PARTICLE IMAGE VELOCIMETRY

Particle image velocimetry (PIV) is an optical, non-intrusive flow measurement technique that allows mapping complex liquid and gas flows. This chapter discusses the working principle of PIV and its main experimental arrangement. Afterwards, large-scale PIV is discussed which allows to match the size of the PIV measurement domain to the size of the cyclist. Finally, evaluation of the aerodynamic drag from the measured velocity is presented, being essential in cyclist aerodynamic study.

3.1 Working principle

PIV is an optical flow measurement technique that relies on the determination of the fluid's velocity from the motion of tracers particles immersed into it (e.g. Adrian 1991; Raffel et al. 2018). A schematic experimental PIV setup is depicted in Figure 3.1. The flow tracers are illuminated, typically using pulsed lasers, and their scattered light is imaged by (digital) cameras. The particle displacement between the consecutive light pulses, separated by a known time interval, Δt provides their velocity. This is converted, using a camera calibration procedure, into the velocity in the real world.

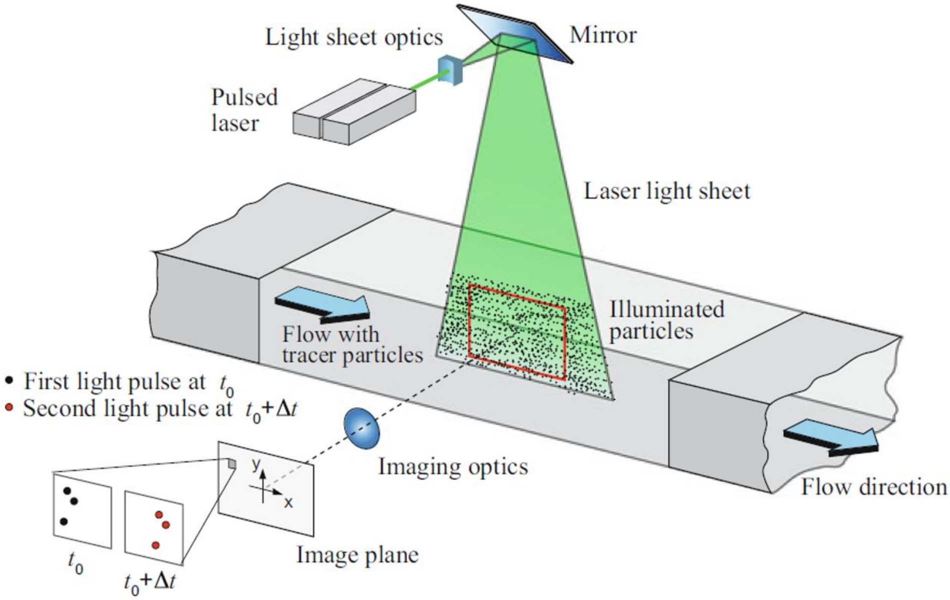

Figure 3.1: Standard PIV experimental arrangement (adapted from Raffel et al. 2018).

Two main PIV acquisition types can be distinguished: dual-frame and single-frame acquisition (see Figure 3.2). Using dual-frame PIV, uncorrelated image pairs are collected at relatively low frequency ($\Delta T >> \Delta t$). Averaging the resulting velocity fields of the acquired image pairs then provides the time-average velocity field and the corresponding distribution of velocity fluctuations. Instead, employing single-frame PIV, also known as time-resolved PIV, single images are acquired at a relatively high frequency in order to obtain the velocity field from each pair of two consecutive images.

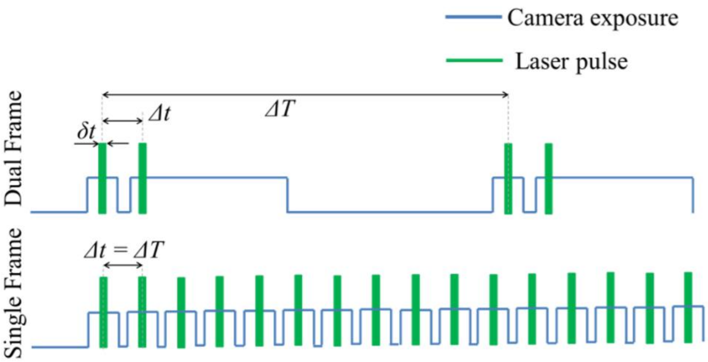

Figure 3.2: Dual frame and single frame PIV acquisition (reproduced from Caridi 2018).

3.2 Stereo and Tomographic PIV

The simplest arrangement for a planar PIV measurement features a single camera. A series of lenses (and sometimes mirrors) is typically used to transform the laser beam into a thin laser sheet (thickness of few millimetre; Figure 3.2). Using a single camera, the in-plane flow velocity components are measured (2D-2C).

In order to measure the third (out-of-plane) velocity component, stereoscopic PIV (stereo-PIV) can be employed (e.g. Prasad 2000), which relies on the same principle as the stereo vison of human eye-sight. Two cameras simultaneously image the illuminated particles in the laser sheet (Figure 3.3), which allows to extract the out-of-plane velocity, in addition to the in-plane components. Lens-tilt adapters are typically used between the camera and the lens in order to match the plane of focus with the illuminated region. Stereo-PIV experiments are more complex in comparison to 2C PIV because the larger amount of alignments and control of illumination and imaging hardware.

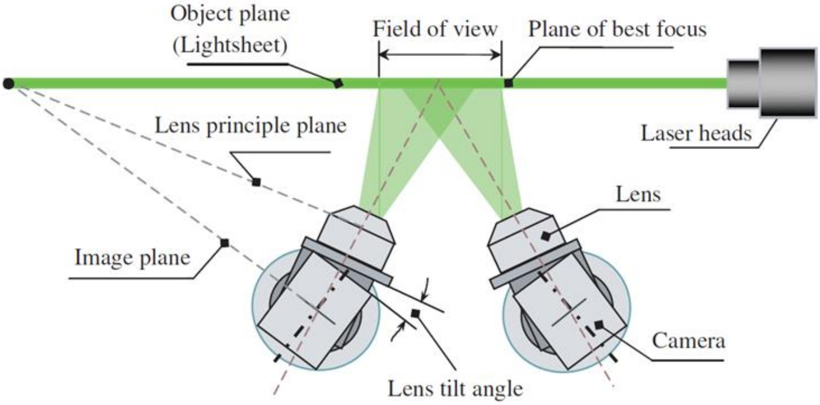

Figure 3.3: Stereo-PIV optical arrangement (adapted Liu et al. 2006).

When the measurements of the velocity and vorticity in a three dimensional domain are necessary, for example in the investigation of complex unsteady three-dimensional flow or to allow accurate pressure reconstruction from velocity data, volumetric PIV can be employed (3D-3C). 3D-PIV is generally conducted using three or more cameras imaging a measurement volume from different angles (see Figure 3.4). The combined 2D images from the different cameras allow to reconstruct the particles in 3D space. The angles between the cameras' lines of sight, the PIV angular aperture, is generally between 40 and 80 degrees for optimal accuracy of the latter particle field reconstruction (e.g. Scarano 2013). A particular concern with volumetric PIV is the particle image density or the number of particles per pixel (*ppp*). Increasing seeding density beyond 0.1 *ppp* results in the situation that individual particles cannot be distinguished anymore on the camera images (Scarano 2013) and their velocity cannot be extracted. In order to avoid a too high *ppp*, the depth of the measurement region typically is small compared to the other two dimensions. Alternatively, one may reduce the seeding concentration at the expense of a reduction of spatial resolution. Some recent 3D-PIV techniques, developed to work at relatively high image density, are discussed in Section 3.3.

For all three PIV arrangements (planar, stereo, 3D), the reduction of the light intensity as a consequence of the expansion of the laser beam, poses further restrictions on the extent of measurement domain. Achieving sufficient illumination for volumetric measurements can be particularly challenging because of the relatively small camera numerical aperture that is required to achieve in-focus particles along the entire measurement depth.

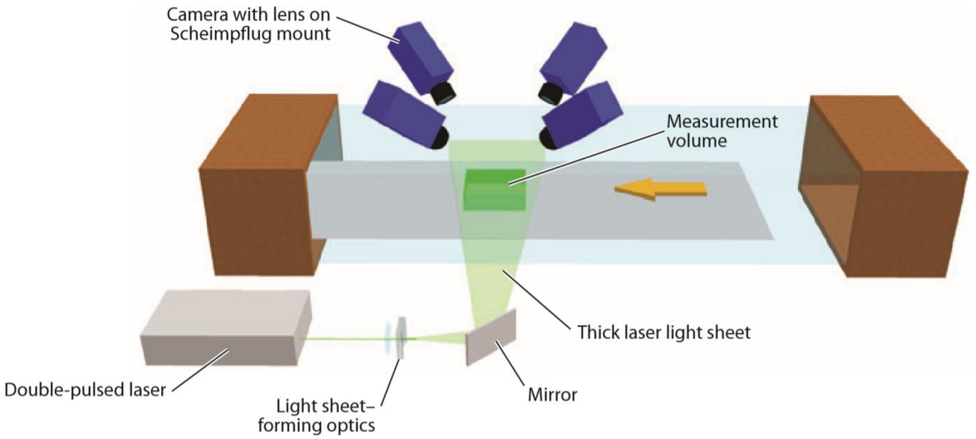

Figure 3.4: Tomographic PIV arrangement (reproduced from Westerweel et al. 2013).

3.3 From particles to velocity

3.3.1 Cross-correlation based PIV

In cross-correlation based PIV the image space is divided into smaller areas, so called ‘interrogation windows’ (Figure 3.5). An average particle displacement is obtained in each interrogation window by cross-correlating the light intensity distribution of two subsequent images. Before cross-correlating, the raw images are typically pre-processed to reduce background reflections that could reduce the cross-correlation signal. The approach finally yields a vector field defined on an Eulerian grid. Cross-correlation based PIV is described by Willert and Gharib (1991), among others.

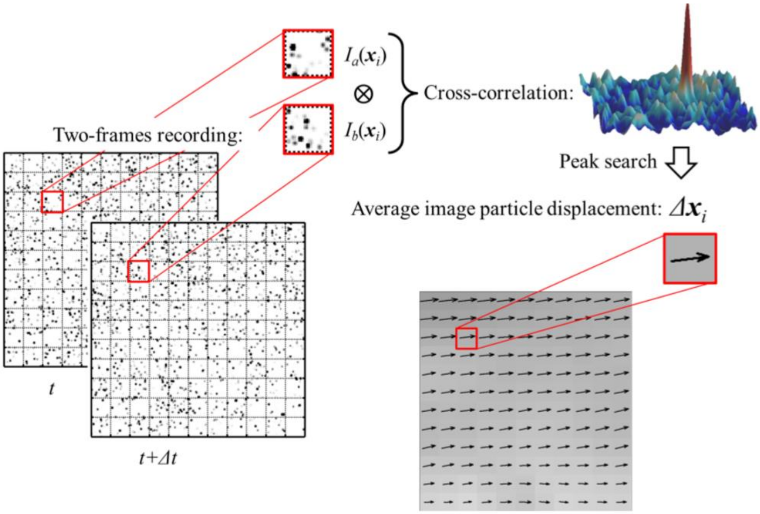

Figure 3.5: Interrogation window cross-correlation procedure.

The literature shows significant efforts to enhance the PIV spatial resolution without sacrificing its accuracy. One of the main algorithms that is commonly used for cross-correlation based PIV is the iterative multigrid window-deformation algorithm (Scarano and Riethmuller 2000): The velocity field, obtained using large interrogation windows, serves as a predictor for window displacement and deformation in a next cross-correlation iteration in which the window size is reduced and, hence, resolution in increased. In addition, to further enhance resolution, but more importantly also PIV measurement robustness and accuracy, ensemble average cross-correlation may be adopted (e.g. Meinhart et al. 2000). This technique relies on averaging the correlation planes of image sequences or image pair ensembles, instead of extracting velocity fields from individual image pairs. In comparison to dual frame velocity field averaging, correlation averaging produces more robust estimates of the time-average flow. The unsteady flow information (velocity fluctuations), however, is lost. Ensemble average correlation may also improve PIV reliability in the condition of inhomogeneous seeding density.

Ensemble averaging correlation may also be used for unsteady flows, providing that the image sequence kernel remains within the flow characteristic time scale (Scarano and Moore 2011). Such selection is not trivial. Alternatively, multi-frame pyramid correlation may be adopted (Sciacchitano et al. 2012) to optimize the observation time based on multiple correlation planes obtained at different time separations.

Tomographic PIV (tomo-PIV; Elsinga et al. 2006) uses the cross-correlation algorithms in 3D. Based on the principle of tomography, the two-dimensional particle images of the different cameras are first reconstructed into a three-dimensional voxel (the 3D equivalent of a pixel) space. This voxel volume is, thereafter, divided into interrogation volumes, yielding the velocity field through cross-correlation. The multiplicative algebraic reconstruction technique (MART; Herman and Lent 1976) proposed by Elsinga et al. (2006) is the most common algorithm for tomographic reconstruction. As a consequence of the large number of particles and small number of cameras, ghost particles are formed during the tomographic reconstruction. These ghost particles appear as spurious peaks in the reconstructed intensity field, in addition to the peaks corresponding to real particles. Because these ghost particles do not follow the flow, they result in velocity vector outliers after the cross-correlation process. The amount of ghost particles and corresponding velocity outliers exponentially increase with increasing particle image density (Elsinga et al. 2011). Hence, the *ppp* of a four-camera MART reconstruction is generally maintained below 0.05. Relying on the fact that the ghosts do not follow the flow, tomo-PIV has been advanced, in order to increase the reconstruction quality, corresponding velocity measurement precision, particularly at high seeding density. This is achieved, among others, adopting time-resolved PIV and utilizing estimated object reconstruction intensities from previous time instances for the prediction of reconstruction in the next and, so, reduce the ghost particle intensity (Lynch and Scarano 2015).

3.3.2 Lagrangian particle tracking

Lagrangian particle tracking (LPT) tracks individual particles along multiple camera exposures. Particle pairing is most simply performed based on a closest neighbour search, which allows to connect the particles from a single image pair. LPT algorithms become more reliable for longer image sequences by using the temporal information from previous time-steps in order to pair particles in the next (see Figure 3.6-left). Long tracks also allow regularization of particle positions by function fitting (e.g. Novara and Scarano 2013; Figure 3.6-right).

Originally, LPT worked reliably up to a maximum particle image density of 0.005 *ppp* (Maas et al. 1993; three camera system). Instead, using tomographic reconstruction (Elsinga et al. 2006) or iterative particle reconstruction (IPR; Wieneke 2013), the *ppp* can be increased one order of magnitude. IPR is used in the Shake-the-Box algorithm (STB; Schanz et al. 2016) presumably the most successful LPT technique in the recent years. Using particle trajectory temporal information, STB predicts the particle distribution in the next time-step. Prediction errors are, subsequently, corrected by an image matching technique, nearly supressing all ghost particles and allowing identification of particle trajectories with high spatial accuracy.

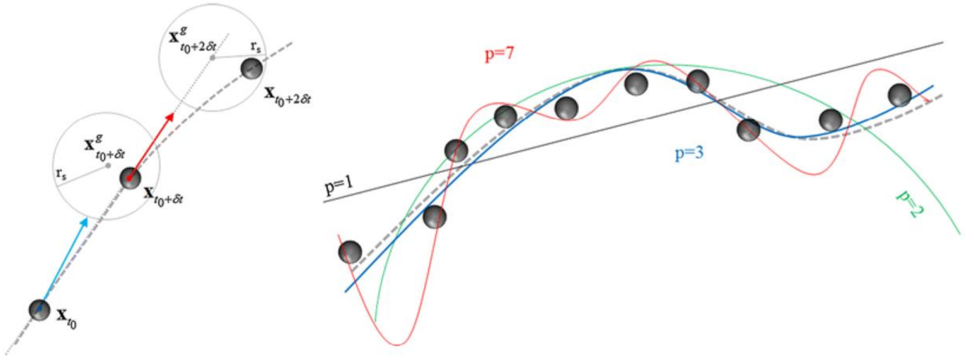

Figure 3.6: Lagrangian particle tracking search algorithm (left) and function-fitting regularization of particle position (right). Figures reproduced from Novara and Scarano (2013).

STB may also be adopted using dual frame PIV acquisition systems using a relatively small time separation and reduced seeding density (Novara et al. 2016). In order to increase the time separation, and, hence, the PIV dynamic velocity range (DVR, Adrian 1997), a multi-Δt approach is recently proposed by Saredi et al. (2020). The velocity field obtained with a small time separation is used as a predictor for the particle pairing at increased Δt .

After application of a Lagrangian particle tracking algorithm, the velocity (and acceleration) is obtained at the particle positions, scattered throughout the measurement domain. The velocity statistics on a Cartesian grid, similar to that resulting from cross-correlation based PIV, can subsequently be obtained from the Lagrangian velocity ensemble (Agüera et al. 2016).

3.4 Large-scale PIV

Most commonly PIV experiments in air flows are conducted using micrometric particles (e.g. fog droplets) as flow tracers, resulting in measurement domains of approximately 30×30 cm^2 and 50 cm^3 for planar PIV and 3D PIV, respectively (Raffel et al. 2018). The introduction of sub-millimeter helium-filled soap bubbles (HFSB; Bosbach et al. 2009) as PIV flow tracers allowed a dramatic increase in measurement size (square meters and liters for planar and volumetric PIV, respectively), making large-scale PIV measurements possible.

3.4.1 Helium-filled soap bubble tracers

The fluid tracing fidelity of a PIV tracer is generally characterized by the response or relaxation time of the particle, τ_p which represents the time in which the particle velocity adapts to 63% of a sudden change in the fluid velocity (defined by a step function):

$$\tau_p = d_p^2 \frac{(\rho_p - \rho)}{18\mu} \qquad 3.1$$

where μ and ρ are the fluid viscosity and density, and d_p ρ_p are the particle diameter and density, respectively. The ideal particle behaviour ($\tau_p \sim 0$) is approached when the particle density equals that of the fluid. Typical subsonic PIV tracers, however, have a density three orders of magnitude larger than that of air and their good tracing fidelity ($\tau_p \sim 1$ µs; Kähler et al. 2012; Melling 1997), instead, relies on the micrometric size of these oil-based droplets (d_p ~ 1 µm). The relatively small extent of conventional PIV measurement domains mainly stems from this small tracer size and their corresponding low light scattering efficiency.

Neutrally buoyant tracers, instead, existed already over two decades ago: HFSB of a few millimeter diameter were used to extend the PIV measurement range to the meter scale (e.g. Müller et al. 1997). As a consequence of the low HFSB production rates (below 1,000 bubbles per second; www.sageaction.com), however, the use of HFSB remained scarce until the introduction of a new type of bubble generator by the German Aerospace Agency (DLR; Figure 3.7), that was able to produce HFSB at a production rate exceeding 50,000 bubbles/second (Bosbach et al. 2009). This nozzle produces sub-millimeter HFSB tracers that scatter approximately 10,000 times more light than the conventional micrometric tracers (Caridi et al. 2016). As a result a rapid increase of the number of investigations conducted with large-scale PIV is observed (e.g. Bosbach et al. 2009; Kühn et al. 2011; Scarano et al. 2015; Caridi et al. 2016; Schneiders et al. 2016; Huhn et al. 2017).

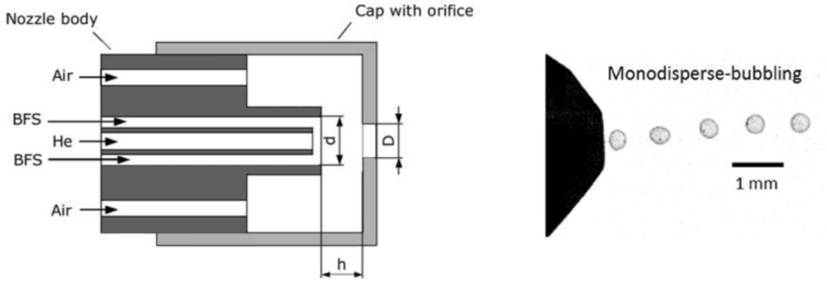

Figure 3.7: DLR HFSB nozzle (Bosbach et al. 2009) and HFSB preferred production regime (right; adapted from Faleiros et al. 2019).

The HFSB are produced using a combination of air, helium and a bubble fluid solution (BFS; Figure 3.7-left). The flow rates of these fluids are controlled by a fluid supply unit to produce neutrally buoyant, lighter-than-air or heavier-than-air bubbles (Caridi 2018). Response times of approximately 30 µs and 500 µs are reported by Faleiros et al. (2018) for HFSB that are close to neutrally buoyant ($\rho_p = 1.1 \pm 0.05$ kg/m^3) and air-filled soap bubbles ($\rho_p = 4.4 \pm 0.7$ kg/m^3). Apart from the response time, the fluid flow rates also affect the HFSB size, production rates and regimes (Faleiros et al. 2019). The latter authors provide guidelines to achieve the shortest response times and the preferred monodisperse-bubbling regime (see Figure 3.7-right).

3.4.2 HFSB seeding for large-scale PIV in wind tunnels

The first large-scale wind tunnel experiment using HFSB tracers employed time-resolved tomo-PIV in a volume of approximately 5 liters (Scarano et al. 2015). A dedicated seeding system was used consisting of a single bubble generator, a reservoir to accumulate the HFSB and a distribution rake to inject the seeding into the wind tunnel test Section (Figure 3.8; Caridi et al. 2016). A seeding density of approximately 1 particle/cm^3 in the wake of a cylinder was temporarily achieved.

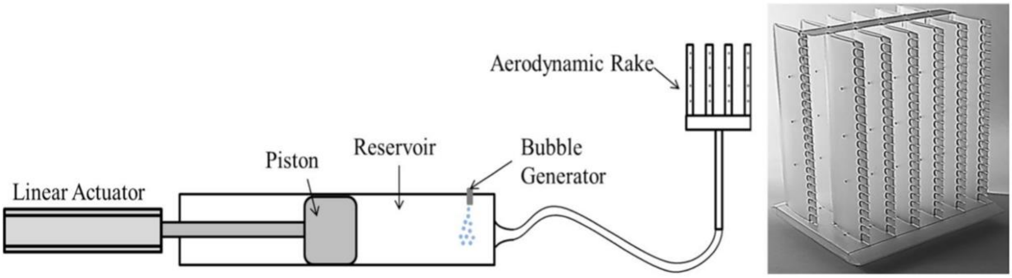

Figure 3.8: Sketch (left) and photo (right) of the HFSB seeding system used by Scarano et al. 2015 and Caridi et al. 2016. Figures reproduced from Caridi et al. (2016).

During the course of the present PhD research, the design of bubble generators has been progressed to achieve robust HFSB seeding in the monodisperse-bubbling regime (e.g. HFSB-GEN-V11 developed at TU Delft; Faleiros et al. 2018). Furthermore, new seeding systems have been developed to achieve higher HFSB production rates and larger cross-sections of the seeded streamtube by increasing the amount of HFSB generators integrated in the seeder rakes (e.g. Jux et al. 2018; Giaquinta 2018). Recently, a modular HFSB generator has been proposed that allows the custom design of the seeding density and the seeded streamtube (Gibeau and Ghaemi 2018) to each unique PIV experiment.

In parallel with the development of the HFSB seeder, different large-scale PIV wind tunnel experiments have been conducted (e.g. dual frame stereo-PIV, Section 4.3 in the present work; single frame tomo-PIV, Scarano et al. 2015; Lagrangian Particle Tracking, Section 4.3 in the present work). The most salient achievement is that of robotic volumetric PIV (Jux et al. 2018) employing robotic actuation of a compact PIV system to scan the time-average flow across a cyclist mannequin in a time-efficient manner (Figure 3.9-bottom). This approach relies on coaxial volumetric velocimetry (CVV; Schneiders et al. 2018), a PIV technique that, in contrast to regular 3D PIV, features a small tomographic aperture ($\beta_0 = 4.3^{\circ}$; see Figure 3.9-top), a coaxial arrangement between the illumination and imaging direction and a large volume depth that exceeds the other measurement area dimensions. The large uncertainty of the particle position along the volume depth, as a consequence of the small aperture, is partly remedied through particle trajectory regularization. The CVV probe integrates four compact cameras and an optical fibre that transmits the laser light, which is consequently directed through a spherical lens achieving a 65^0 light spreading angle (see Figure 3.9-top). As a consequence of the coaxial PIV arrangement, the measurement of the flow around complex geometries can be obtained in a relatively short time (a few minutes per position of the CVV probe).

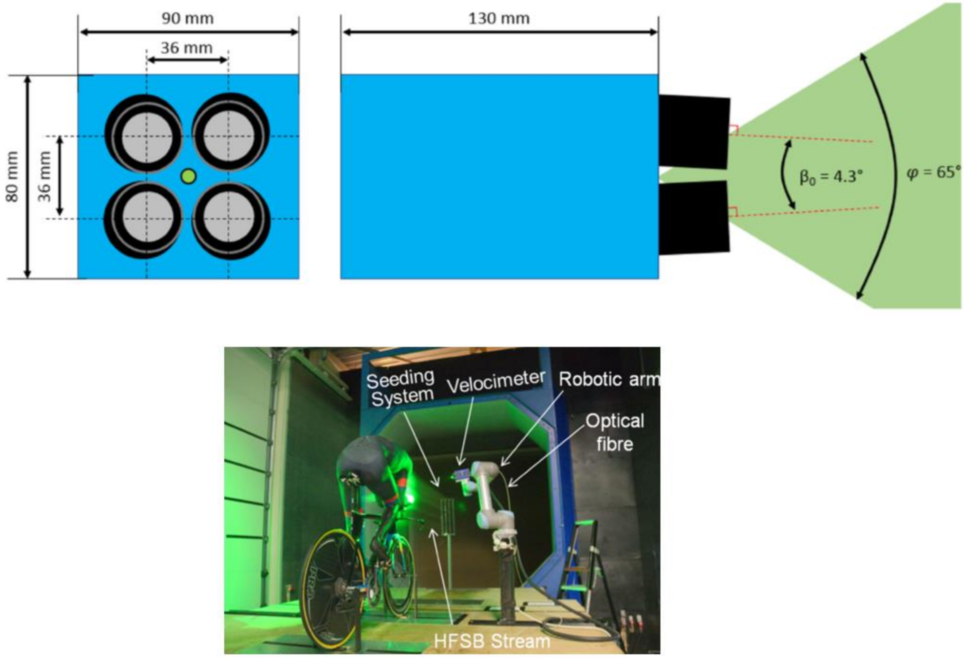

Figure 3.9: A sketch of the CVV probe (top; Figure reproduced Schneiders et al. 2018) and a robotic volumetric PIV experimental setup (bottom; Figure reproduced Jux et al. 2018).

3.5 Aerodynamic drag from PIV

In the last two decades PIV has been used extensively for aerodynamic load determination, primarily due to its whole-field measurement capability and non-intrusive nature. The loads are generally obtained invoking the conservation of momentum in a control volume surrounding the object. This section provides an overview of different control volume formulations and the PIV experimental arrangements reported in the literature for practical implementation of these frameworks.

3.5.1 Control-volume integral formulation

The aerodynamic loads acting on a body moving relative to a fluid can be derived by application of the conservation of momentum in a control volume containing this body (Anderson 1991), as visualized in Figure 3.10. In the incompressible flow regime, the air resistance acting on the body can be written as:

$$D(t) = -\rho \iiint_V \frac{\partial u}{\partial t} dV - \rho \iint_S (\boldsymbol{u} \cdot \boldsymbol{n}) u dS - \iint_S \left((p\boldsymbol{n} - \boldsymbol{\tau} \cdot \boldsymbol{n}) dS \right)_x \qquad 3.2$$

where is $\boldsymbol{u}$ the velocity vector with components [u,v,w] along the coordinate directions [x,y,z] respectively, p the static pressure and $\boldsymbol{\tau}$ the viscous stress tensor. V is the control volume, with S its boundary and $\boldsymbol{n}$ is the outward pointing normal vector.

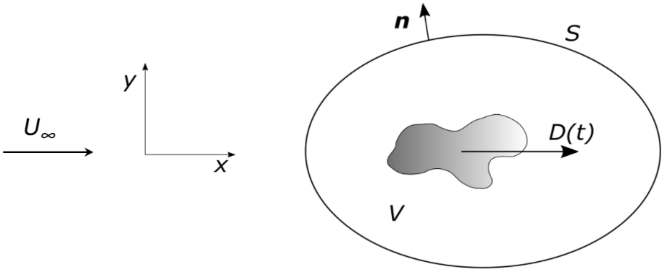

Figure 3.10: Schematic description of the control volume approach.

Equation 3.2 is used, among others, by Unal et al. (1997) and Kurtulus et al. (2007) to estimate the unsteady forces on two-dimensional cylinders. PIV measurement all around the model, to evaluate the volume integral in this equation, however, is not straightforward. In the latter work, a transparent model is used in order to avoid shadows in the region directly atop of the model. Alternatively, illumination in the entire domain may be achieved reflecting the laser light by mirrors or by using a second laser. Despite such adaptations, PIV measurement in close proximity to the model surface typically remains challenging as a consequence of limited optical access and model reflections.

3.5.2 Surface integral formulation

The evaluation of the volume integral on the right hand side of Equation 3.2 poses the typical, aforementioned PIV measurement problems. Moreover, for three-dimensional objects the evaluation of the volume integral is practically impossible. This can be avoided, firstly, considering the time-average drag instead of its instantaneous value. When decomposing the equation into the Reynolds average components and averaging both sides of the equation, the time-average drag force, $\overline{D}$ is obtained with the sole contribution of surface integrals (e.g. van Oudheusden et al. 2006; van Oudheusden et al. 2007):

$$\overline{D} = -\rho \iint_S \left(\overline{\boldsymbol{u}} \cdot \boldsymbol{n} \right) \overline{u} dS - \rho \iint_S (\boldsymbol{u}' \cdot \boldsymbol{n}) u' dS - \iint_S \left(\overline{p} \boldsymbol{n} dS \right)_x \qquad 3.3$$

where the overbars and the primes denote the time-average and fluctuating flow variables. Estimation of the aerodynamic drag using Equation 3.3 can become inaccurate as demonstrated by van Oudheusden et al. (2006) by comparison of the aerodynamic drag from PIV, obtained by invoking the conservation of momentum across a rectangular control volume (Figure 3.11-top), to that from CFD simulations (Figure 3.11-bottom). Using a wake rake formulation (discussed in the next section), instead, provides superior drag accuracy.

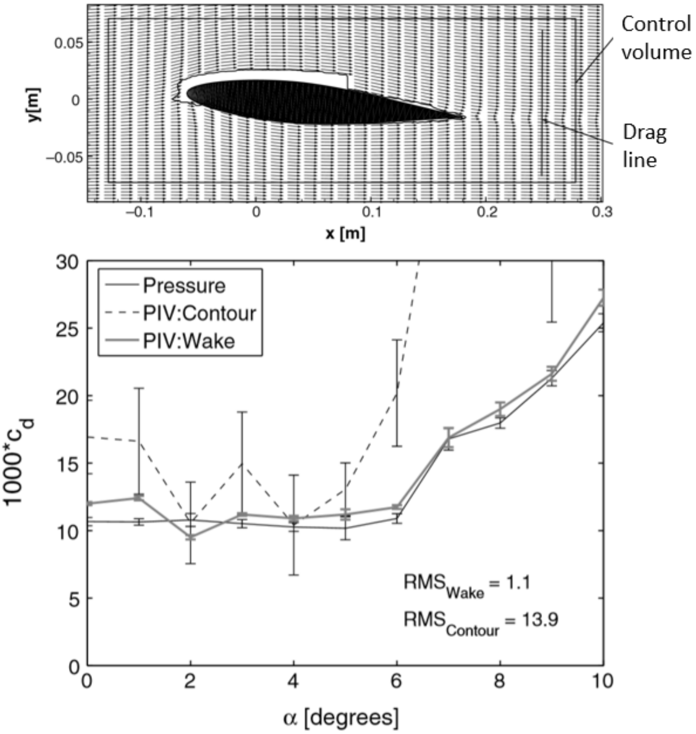

Figure 3.11: Control volume load estimation on 2D airfoil: Sketch of the model, the time-average vector field and the control volume (top) and comparison of the drag coefficient among the different drag evaluation methods (bottom). Figures reproduced from van Oudheusden et al. (2006).

When measurement of the instantaneous aerodynamic drag is required, a second, alternative approach consists of rewriting the volume integral in Equation 3.2 in into surface integrals through a derivative-moment transformation (DMT; Mohebbian and Rival 2012) and so to express the drag force in surface integrals only:

$$D(t) = -\rho \,{}^{\partial}\!/_{\partial t} \iint_S x_{ref}\,(\boldsymbol{u}\cdot\boldsymbol{n})\,dS - \rho\iint_S (\boldsymbol{u}\cdot\boldsymbol{n})\,u\,dS - \iint_S (p\boldsymbol{n}dS)_x \qquad 3.4$$

where x_{ref} is the streamwise distance between the control volume and an arbitrary fixed frame of reference. Mohebbian and Rival demonstrated that the DMT method and the more conventional one, expressed by Equation 3.2, yield a similar drag accuracy.

3.5.3 Wake rake formulation

A more classical, wake rake formulation may be used that only requires the measurement in a plane (a line for 2D flows; drag line is marked in Figure 3.11-top) downstream of the model. Wake rakes have a long tradition and, originally, the resistance force was derived from the pressure field measured in the wake of the model by a Pitot-tube rake (e.g. Jones 1936). The approach is often used to estimate the aerodynamic drag of airfoils (e.g. Guglielmo and Selig 2011) or three-dimensional models (e.g. Brune 1994; Maskell 1973) offering more sensitivity compared to force balances when the drag force is small (e.g. Guglielmo and Selig 2011). The PIV wake rake provides a non-intrusive alternative. When the segments *ab*, *ad* and *bc*, depicted in Figure 3.12, are taken sufficiently far away from the model and invoking the conservation of mass, the expressions for the aerodynamic drag can be rewritten such that the only surface integral to be evaluated is that along S_{wake} (segment *cd*).

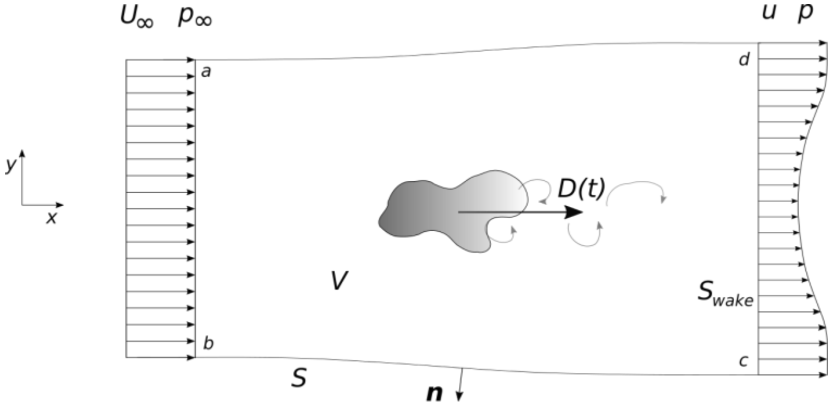

Figure 3.12: Illustration of the control volume and wake rake approach.

The expression for the instantaneous drag, rewriting Equation 3.4, then becomes:

$$D(t) = -\rho \, \partial/\partial t \iint_{S_{wake}} x_{ref} u dS + \rho \iint_{S_{wake}} (U_\infty - u) u dS + \iint_{S_{wake}} (p_\infty - p) dS \qquad 3.5$$

where U_∞ and p_∞ are the freestream velocity and pressure, respectively. The conservation of mass reduces the first integral at the right-hand-side of the equation to zero for stationary inflow conditions and simplifies the expression for the instantaneous aerodynamic drag (de Kat and Bleischwitz 2016):

$$D(t) = \rho \iint\limits_{S_{wake}} (U_\infty - u) u dS + \iint\limits_{S_{wake}} (p_\infty - p) dS \qquad 3.6$$

The expression for the time-averaged aerodynamic drag, rewriting Equation 3.3 into wake rake formulation, becomes:

$$\overline{D} = \rho \iint\limits_{S_{wake}} \left(U_\infty - \overline{u}\right)\overline{u} dS - \rho \iint\limits_{S_{wake}} \overline{u'^2} dS + \iint\limits_{S_{wake}} \left(p_\infty - \overline{p}\right) dS \qquad 3.7$$

The PIV wake rake approach largely simplifies the necessary PIV experimental arrangement in particularly for 3D models. Furthermore, the accuracy of the PIV wake rake drag estimation is improved in comparison to the integrating over the full control volume boundary, as a consequence of the implicit mass conservation (van Oudheusden et al. 2006).

In this work, the first, second and third term at the right-hand-side of Equation 3.7 are addressed to as the momentum, the Reynolds stress and the pressure term, respectively.

3.5.4 Pressure evaluation from PIV measurements

The static pressure is required for the evaluation of the aerodynamic drag using Equations 3.2 to 3.7. For incompressible, low-speed flows, the momentum equation can be used to express the gradient of the pressure field, ∇p in terms of the velocity field:

$$\nabla p = -\rho \frac{D\mathbf{u}}{Dt} + \mu \nabla^2 \mathbf{u} \qquad 3.8$$

where $D\mathbf{u}/Dt$ is the material acceleration, the acceleration of a fluid's parcel in a Lagrangian perspective, and μ the fluid's dynamic viscosity. From an Eulerian perspective, the material acceleration can be expressed in terms of a local and convective term:

$$\frac{D\mathbf{u}}{Dt} = \frac{\partial \mathbf{u}}{\partial t} + \mathbf{u} \cdot \nabla \mathbf{u} \qquad 3.9$$

After substitution of Equation 3.9 into Equation 3.8, the pressure gradient reads as:

$$\nabla p = -\rho \left(\frac{\partial \mathbf{u}}{\partial t} + \mathbf{u} \cdot \nabla \mathbf{u} \right) + \mu \nabla^2 \mathbf{u} \qquad 3.10$$

Reynolds-averaging of Equation 3.10 results in an expression for the time-average pressure gradient:

$$\nabla \overline{p} = -\rho\left(\overline{\mathbf{u}} \cdot \nabla\right)\overline{\mathbf{u}} \ -\rho\nabla \cdot \left(\overline{\mathbf{u}'\mathbf{u}'}\right) + \mu\nabla^2 \overline{\mathbf{u}} \tag{3.11}$$

It is noted here that for a complete evaluation of the above equation, all three velocity components and their spatial derivatives are needed, which is to be considered in the PIV experimental arrangement.

The equations for pressure above can be used to obtain the pressure along the control surface boundaries by spatial integration of the pressure gradient, where pressure boundary conditions are typically described in the undisturbed flow regions. This approach, however, suffers from error propagation, as a consequence of spatial integration (e.g. van Oudheusden 2013). Alternatively, the Poisson equation for pressure can be solved, which is obtained after taking the divergence of Equation 3.9:

$$\nabla^2 p = -\rho\nabla \cdot \left(\mathbf{u} \cdot \nabla\right)\mathbf{u} \tag{3.12}$$

This can also be written in terms of the Reynolds-average components, similarly to Equation 3.11:

$$\nabla^2 \overline{p} = -\rho\nabla \cdot \left(\overline{\mathbf{u}} \cdot \nabla\right)\overline{\mathbf{u}} \ -\rho\nabla \cdot \nabla \cdot \left(\overline{\mathbf{u}'\mathbf{u}'}\right) \tag{3.13}$$

This Poisson equation for pressure can be considered a global optimization formulation of the pressure gradient spatial integration and can be solved using standard numerical mathematic procedures (e.g. Fujisawa et al. 2005).

4

CYCLIST PIV WAKE RAKES IN WIND TUNNELS

This chapter is dedicated to cyclist aerodynamic drag measurement using large-scale PIV wake rakes in wind tunnels. The velocity statistics in the wake of a full-scale cyclist mannequin is obtained adopting, firstly, Lagrangian particle tracking and, secondly, more conventional stereo-PIV. In both cases HFSB tracers are used to allow velocity measurement in a human size wake plane. The choice of the adopted PIV technique depends on the size of the seeded streamtube. The time-average streamwise velocity and vorticity compare well to literature. The chapter closes assessing the accuracy of the PIV wake rake aerodynamic drag, comparing the drag value to force balance data.

Part of the work presented in this chapter is published in:

Terra W, Sciacchitano A, Shah YH (2019), *Aerodynamic drag determination of a full-scale cyclist mannequin from large-scale PTV measurements*. Exp Fluids 60:29

Sciacchitano A, **Terra W**, Schneiders JFG, Jux C, Shah Y, Scarano F (2018) *Flow over a Full-Scale Cyclist Model by Tomographic PTV*. In: Particle Image Velocimetry, A Practical Guide, 3rd edition, Springer International Publishing AG, Cham, Switzerland

4.1 Introduction

Load determination from large-scale PIV in wind tunnels has been hampered firstly by the limited HFSB tracers concentration, which has been below 1 bubble/cm^3 (Caridi et al. 2016), and secondly by the limited size of the seeded stream tube cross-section, not exceeding the order of 0.1 m^2 (Caridi et al. 2016; Jux et al. 2018). The research described in this chapter assesses the feasibility of using a large-scale PIV wake rake for the determination of the aerodynamic drag of a three-dimensional human-scale cyclist mannequin. For this purpose, in a first wind tunnel experiment, Lagrangian particle tracking is employed to obtain the velocity in a plane of approximately 1.6 m^2 in the wake of the model. A wake scanning approach is employed. These *partitioned-wake* experiments (PWE), hence, yields the time-average flow topology after merging the particle tracks obtained in each of the seeder positions. In a second wind tunnel experiment, stereo-PIV is used in combination with a renewed seeding system (50 × 100 cm^2), larger than that used in the first experiment. In these *full-wake* experiments (FWE), the seeded streamtube spans the full wake of the cyclist yielding the time-average velocity as a statistical average of the measured instantaneous velocity fields.

The distribution of streamwise velocity, its fluctuations and the pressure in the wake plane are presented and discussed. Furthermore, the time-average aerodynamic drag is obtained using the PIV wake rake methodology and its accuracy is evaluated by comparison with state-of-the-art balance measurements. For this purpose, in the first campaign, the measurements are repeated in a small range of freestream velocity so that the seeding density and the drag coefficient can be assumed invariant. In the second campaign, a wider range of speeds is selected and different geometrical arrangements are considered as well.

4.2 Drag resolution methodology

The accuracy of the drag estimation via the PIV wake rake approach is assessed via direct comparison with state-of-the-art balance measurements. The drag resolution of the PIV wake rake is evaluated as:

$$\Delta C_D = \sqrt{\frac{1}{N}\sum_{i=1}^{N}\left(\overline{C_{D_{i,PIV}}} - \overline{C_{D_{i,bal}}}\right)^2} \qquad 4.1$$

where $\overline{C_{D_{i,PIV}}}$ and $\overline{C_{D_{i,bal}}}$ are the time-average drag coefficients from the PIV wake rake and the balance system, respectively, and N is the number of repeated measurements at different experimental conditions.

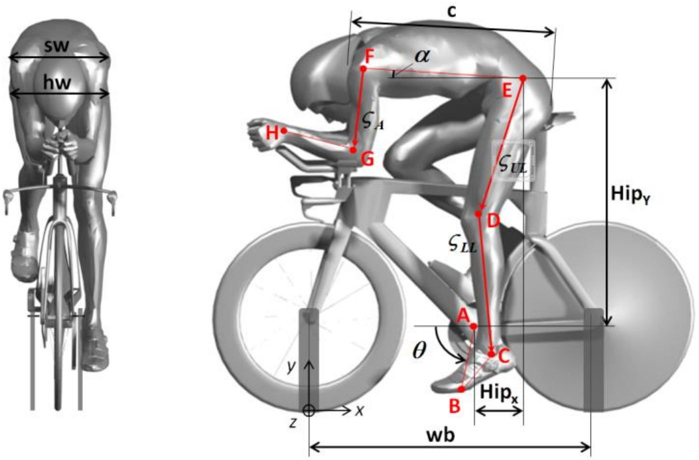

Figure 4.1: Geometry of the cyclist mannequin and bike with indication of reference system.

4.3 Experimental apparatus and procedure

4.3.1 Wind tunnel apparatus

The experiments are conducted in the Open Jet Facility (OJF) of the Aerodynamics Laboratories at the Delft University of Technology. This atmospheric closed-loop, open-jet wind tunnel has an octagonal cross-section of 2.85 m × 2.85 m with a contraction ratio of 3:1 and it can generate a homogeneous jet at speeds between 4 to 35 m/s with approximately 0.5% turbulence intensity (Lignarolo et al. 2014). The cyclist wind tunnel model consists of a rigid-body full-scale cyclist mannequin, which is manufactured from thermoplastic polyester by additive manufacturing after scanning an elite cyclist in time-trial position (Van Tubergen et al. 2017). The legs of the mannequin are in asymmetric position (left leg stretched and right leg bended) relating to a $\theta = 75^{\circ}$ crank angle (Figure 4.1). The model's torso length c and frontal area A are 0.6 m and 0.32 m^2, respectively. More details of the mannequin dimensions are available in Table 4.1. A 4.9 m long and 3.0 m wide wooden table, elevated 20 cm above the wind tunnel contraction exit, is used to reduce the boundary layer thickness interacting with the model.

During all measurements, the mannequin is placed on a time-trial bike, which is supported at the front and rear axis (see Figure 4.2-left). The Giant Trinity Advanced Pro frame is equipped with a Pro Textreme disc rear wheel. In the PWE and FWE, a Shimano DuraAce C75 and a Pro Textreme 3-spoke front wheel are used, respectively. In the PWE, the mannequin was wearing a long-sleeved *Etxeondo* time trial suit along with a *Giant* time trial helmet (season 2016). During the FWE, instead, a bare model was employed wearing a Bell Javelin TT helmet. In the latter case, the helmet orientation is varied between 'tail-up' and 'tail-down' referring to helmet angle of attack, α_H (see Figure 4.2-right). Furthermore, measurements are conducted with and without zig-zag tape applied on the stretched leg. The zig-zag tape (height of 0.35 mm; thickness of 11 mm in streamwise direction; pitch of 6 mm) is applied at the inside and outside of the leg at approximately 45 degrees from the upstream stagnation point (Figure 4.2-right).

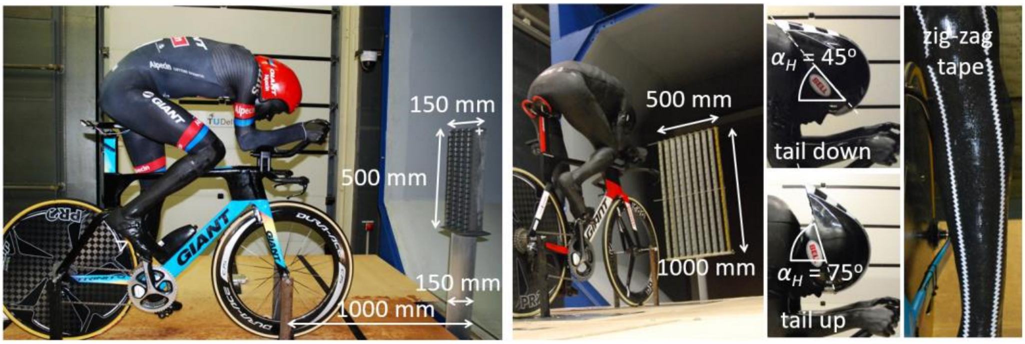

Figure 4.2: Wind tunnel model and PIV seeding system of the *partitioned-wake* experiments (left) and the *full-wake* experiments (middle and right).

Table 4.1: Mannequin and bike characteristic lengths and angles.

Name	Symbol	Position/length
Crank angle	Θ	75°
Torso angle of attack	α	5°
Hip width	hw	365 mm
Shoulder width	sw	380 mm
Hip location x	Hip_x	180 mm
Hip location y	Hip_y	850 mm
Wheel base	wb	1003 mm
Wheel diameter	w_{Θ}	700 mm
Crank length	$\overline{AB}$	175 mm
Lower leg length	$\overline{CD}$	475 mm
Upper leg length	$\overline{DE}$	460 mm
Torso length	c	700 mm

4.3.2 PIV system and procedures

The flow field in the wake of the cyclist model is measured using neutrally buoyant helium-filled soap bubbles (HFSB) as flow tracers. The latter have a diameter of approximately 300 µm (Scarano et al. 2015) and are introduced into the flow by in-house developed seeding rakes. The flow rates of helium, air and bubble fluid solution are regulated via a Fluid Supply Unit from LaVision GmbH. Each seeding rake consists of multiple vertically installed streamlined wings holding the HFSB generators. The same wing design is used in both seeders and the vertical and horizontal pitch between the generators is provided in Table 4.2. At a freestream velocity of

14 m/s and nominal seeder working conditions the seeding concentration is estimated at 1.4 tracer/cm^3 (Caridi et al. 2016).

In the PWE the seeder is installed on a two-axis traversing system at the exit of the wind tunnel contraction (see Figure 4.2-left). The trailing edge of the rake is installed 85 cm upstream of the front wheel's axis seeding a streamtube of approximately 20 × 50 cm^2 cross-section in the freestream. In order to achieve seeding in the entire wake of the model, measurements are repeated at 15 different positions of the seeding rake, 5 along the horizontal direction and 3 along the vertical direction. Details on the different seeder positions and the effect of the seeding rake on the measured aerodynamic drag are provided in Appendix A. In contrast, the seeder in the FWE remains in a fixed position approximately 1.5 m upstream of the front wheel's axis (Figure 4.2-middle). The seeded streamtube cross-section measures approximately 50 × 100 cm^2 in the freestream. Due to the presence of the small seeding rake, the freestream turbulence intensity, measured two meters downstream of the seeding rake, is increased from 0.5% to 1.9%, while the mean flow remains unaltered (Jux et al. 2018). Considering that the streamlined vertical wings of the small and large seeder feature the same cross-sectional shape, it is assumed that the large seeder alters the freestream flow in a similar fashion.

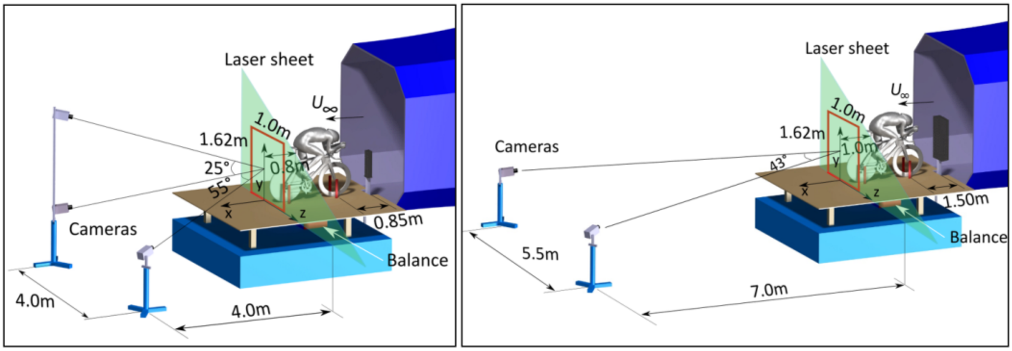

Figure 4.3: Experimental setup of the *partitioned-wake* experiments (left) and *full-wake* experiments (right).

In the PWE a high-repetition rate PIV system is adopted allowing Lagrangian particle tracking. A low-rate system is used to conduct stereo-PIV in the FWE. An overview of all PIV equipment and parameters is provided in Table 4.2. In both experiments a 5 cm thick volume, approximately one meter downstream of the bike's saddle, is illuminated by collimated laser light and an area of approximately 1.6 × 1.0 m^2 in y and z-direction, respectively, is imaged by the PIV cameras. Geometrical calibration is conducted using an in-house built double-plane calibration target of 1.2 m × 1.2 m. The target contains a total of 156 circular dots of 8 mm diameter per plane, distributed over 12 rows and 13 columns with a pitch of 9 cm in both vertical and horizontal direction. The offset between the two planes is 2 cm; the dots of the two planes are staggered by 4.5 cm in both the vertical and horizontal directions.

Table 4.2: PIV equipment and parameters.

Equipment

Purpose	**Instrument/ parameter**	***Partitioned-wake* experiments (PWE)**	***Full-wake* experiments (FWE)**
Imaging	Cameras	3 Photron FastCAM SA1 (CMOS sensor, 12 bit, 20 μm pixel pitch, 1024 × 1024 pixels at full resolution)	2 LaVision *Imager* LX (CCD sensor, 12 bit, 4.4 μm pixel pitch, 1628 × 1236 pixels at full resolution)
	Objectives	Nikkor 50 mm	Nikkor 35 mm
Illumination	Laser	Continuum Mesa PIV 532-120-M laser (Nd:YAG diode pumped, pulse energy of 18 mJ at 1 kHz)	Quantel Evergreen 200 laser (Nd:YAG diode pumped, pulse energy 2 x 200mJ)
Seeding	Tracer particles	HFSB	HFSB
	Seeding system	4 wing-80 nozzles, vertical and horizontal pitch of 25 mm and 50 mm, respectively.	10 wing-200 nozzles, vertical and horizontal pitch of 25 mm and 50 mm, respectively.
	Freestream seeded cross-section [cm^2]	20 × 50	50 × 100

Parameters

Purpose	**Instrument/ parameter**	**PWE**	**FWE**
Field of view	x [m] (laser sheet thickness)	0.05	0.05
	y [m]	1.6	1.6
	z [m]	1.0	1.0
	Downstream position [m]	0.8	1.0
Imaging	$f_\#$	4	5.6
	Magification	0.0125	0.0045
	Digital image resolution [mm/px]	1.6	1.0
	Object distance [m]	4.5	7.5
	PIV angles [°]	55 (y-plane); 25 (z-plane)	43

4.3.3 PIV measurement procedure

In the PWE, the images are recorded in short bursts of 11 images at 4 kHz acquisition frequency. For each position of the seeding generator, 480 bursts are acquired with 0.1 second separation between two successive bursts to obtain a statistical ensemble of uncorrelated particle tracks. Particle streaks, visualized as the maximum image intensity over the 11 subsequent images of a burst, in the centre of the model's wake and in the freestream are depicted in Figure 4.4 top-left and right, respectively. The number of particles per pixel (ppp) varies between 0.04 and 0.1 depending on the seeder position. The highest density is observed in the freestream, where the seeded streamtube remains largely unaffected by the presence of the model, whereas the lowest ppp appears in the cyclist's wake as the particles spread over a larger cross-section.

The stereo-PIV measurements in the FWE are conducted at 5.5 Hz and a total of 500 image-pairs are collected. The central portion of the cyclist's wake is well seeded. However, towards the boundaries of the image seeding is absent. The consequences of this lack of seeding are discussed later in this chapter. At a freestream speed of 4.5 m/s (Figure 4.4 bottom-left) and 13 m/s (Figure 4.4 bottom-right) the particles per pixel are 0.01 and 0.005, respectively. The particle image intensity is approximately equal to 200 and 4000 counts over a background intensity of about 20 and 200 counts, resulting in an image signal-to-noise ratio of 10 and 20 in the PWE and FWE, respectively. In the former case, image acquisition and processing is conducted with DaVis 8.4 (LaVision GmbH), while in the latter case DaVis 10 is used.

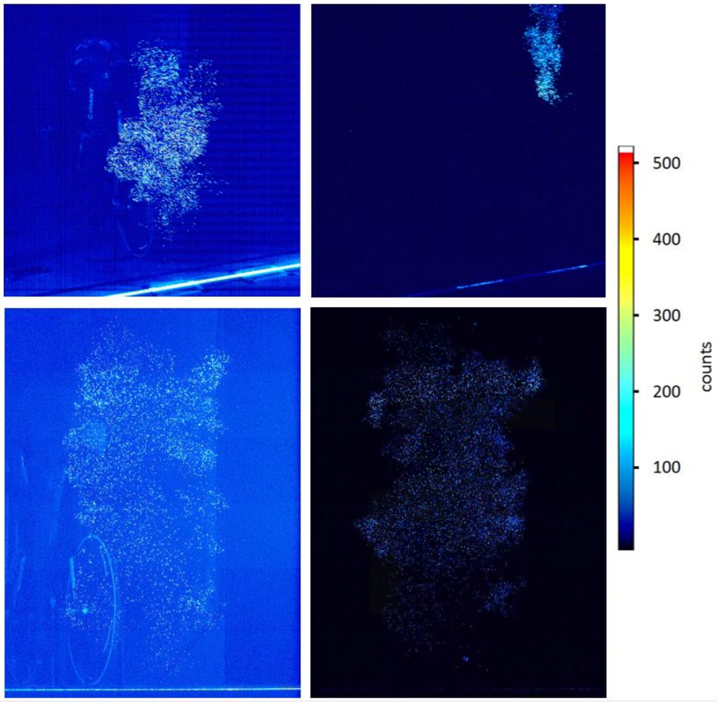

Figure 4.4: Raw images obtained from the *partitioned-wake* (top-left) and *full-wake* experiments (bottom-left). Images after pre-processing of the PWE (top-right) and FWE (bottom-right). Note, that the two images of the PWE experiment (top) are obtained with the seeder in different positions.

4.3.4 Force balance measurements

Force measurements are carried out with a six-component balance designed, manufactured and calibrated by the Dutch Aerospace Laboratory (NLR). Under simultaneous loading of all six components (three forces and three moments), the balance is capable of measuring loads up to 250 N in the streamwise direction with a maximum uncertainty of 0.06% of the full-scale value

(Alons 2008). The balance is mounted directly under the ground plate, shielded from the air flow, and connected to the bike supports (see Figure 4.3). The balance measurements are conducted simultaneously to the PIV measurements in both experiments; the acquisition frequency is set to 2 kHz and the observation time is 30 seconds.

In the PWE, PIV and force balance measurements are repeated at five different freestream velocities between 12.5 m/s and 15 m/s, corresponding to $Re = 5\times10^5$ to $Re = 6\times10^5$ based on the torso length. Table 3 provides an overview of the data acquisition parameters and the varying experimental conditions. The FWE are conducted at two nominal freestream velocities (4.5 and 13 m/s) and at each speed the geometry and surface texture of the cyclist model is varied.

Table 4.3: PIV, wind tunnel and model experimental conditions

***Partitioned-wake* experiments**		
Acquisition parameters	PIV	Bursts of 11 images at 4 kHz; 480 image bursts at 10 Hz
	Force balance	Acquisition at 2 kHz; Observation time of 30 seconds
Experimental conditions (for PIV and balance)	Freestream velocity	U_∞ = [12.95, 13.34, 13.71, 14.33, 14.78] m/s
	Seeding system	15 different positions; 5 along the horizontal direction and 3 along the vertical direction (details are provided in Appendix A)

***Full-wake* experiments**				
Acquisition parameters	PIV	500 image pairs at 5.5 Hz		
	Force balance	Acquisition at 2 kHz; Observation time of 30 seconds		
Experimental conditions (for PIV and balance)		*U_∞ [m/s]*	*Helmet orientation*	*Zig-zag tape leg*
	case 1	4.52	up	no
	case 2	4.58	up	no
	case 3	4.57	down	no
	case 4	4.57	down	yes
	case 5	4.60	down	yes
	case 6	12.90	down	no
	case 7	12.83	up	no
	case 8	13.10	down	yes
	case 9	13.11	down	no

4.3.5 PIV data reduction

The images acquired in the PWE are pre-processed by subtraction of the time-averaged intensity of each burst to remove background noise (see Figure 4.4-top-left vs right for a raw and processed image, respectively) and are then processed with the Shake-The-Box algorithm (STB; Schanz et al. 2016) yielding Lagrangian particle tracks. Particle tracks resulting from one image

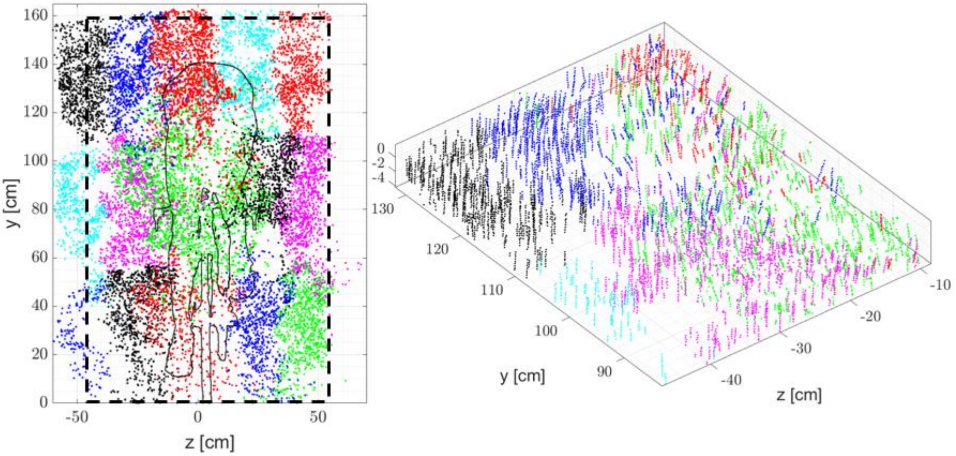

Figure 4.5: Lagrangian particle tracks in the entire wake of the model (left) and a close-up (right) obtained from one image burst for each of the seeder locations (different seeder locations are colour coded).

burst per seeder location are depicted in Figure 4.5 (colours indicate different seeder positions) illustrating the extent of overlap of tracks stemming from the different positions.

Velocity statistics (time-average and fluctuations root-mean-square) are computed from the Lagrangian velocity ensemble within bins of size $5 \times 4 \times 4$ cm^3 with 0%, 75% and 75% overlap in x, y and z direction, respectively (Agüera et al. 2016). The resulting velocity field is defined on a Cartesian grid with a vector pitch of 1 cm along y and z directions. The bin size was determined requiring a minimum number of 25 tracks per bin. A universal outlier detection filter (Westerweel and Scarano 2005) was applied to the particle velocity data in each bin, to reduce spurious tracks, resulting in an average number of used tracks per bin of approximately 2000. The uncertainty of the velocity data is estimated comparing the time-average streamwise velocity obtained from different seeder positions in regions of overlap. Discrepancies of approximately 5% and 2% are obtained in the wake and the freestream, respectively.

The background noise and reflections in the acquired PIV images during the FWE are reduced applying, consecutively, a high-pass frequency filter (Sciacchitano and Scarano 2014) and subtraction of a constant intensity value to reduce the noise level outside of the seeded region to zero. Afterwards, first a reference velocity field is obtained adopting multi-pass stereo cross-correlation applying the PIV sum-of-correlation algorithm using 64×64 interrogation windows with 75% overlap. Afterwards, the same multi-pass stereo cross-correlation approach is adopted to the individual pre-processed image pairs, estimating the interrogation window shift in the first pass from the earlier obtained reference velocity field. This results in a time-average velocity field and its standard deviation featuring a vector pitch of 1.6 cm.

For the computation of the aerodynamic drag via Equation 3.7, apart from the velocity statistics in the wake plane, the freestream velocity U_∞ and the static pressure are needed. The measured freestream velocity, $U_{\infty,meas}$ is obtained as the mean streamwise velocity over the free boundary of the wake plane, excluding a region in relative proximity to the floor ($y > 50$ cm). Furthermore, a correction for the wind tunnel jet expansion, ε_S and the nozzle blockage, ε_N is applied according to Mercker and Wiedemann (1996), to obtain U_∞:

$$\frac{U_\infty}{U_{\infty,meas}} = 1 + \varepsilon_S + \varepsilon_N \tag{4.2}$$

with $\varepsilon_S = 0.0018$ and $\varepsilon_N = 0.0132$. The static pressure is obtained solving the Poisson equation for pressure prescribing Neumann conditions on the bottom boundary and Dirichlet conditions with freestream pressure value on the three free boundaries. For the pressure reconstruction, the streamwise gradients of the time-average velocity and of the velocity fluctuations are neglected after estimating that these are two orders of magnitude smaller than the corresponding in-plane gradients.

Finally, it should be noted that the advantage of the PTV measurement approach adopted in the PWE, opposed to using stereo-PIV, is that a stitching procedure of the velocity information obtained from the different seeder positions is not necessary. Stitching of velocity fields may result in anomalies in the velocity gradients in the overlap regions (Shah 2017), which yield reduced accuracy in the pressure field reconstruction from the solution of the Poisson equation.

4.4 Results

4.4.1 Time-average streamwise velocity and vorticity

The obtained time-average flow topology in the wake of the cyclist mannequin is discussed in terms of the spatial distribution of the streamwise velocity (Figure 4.6-left) and vorticity with in-plane vectors (Figure 4.6-right). The streamwise velocity contours exhibit two main regions of significant velocity deficit. The first one is located behind the lower back of the mannequin ($y \sim 100$ cm) slightly towards the left, and features a minimum velocity of $u/U_\infty \sim 0.6$. The lateral asymmetry of this velocity deficit originates from the asymmetric leg position (left leg extended downwards and right leg bent upwards), and agrees well to literature (e.g. Crouch et al. 2014; Jux et al. 2018). The minimum value of the streamwise velocity is comparatively higher than that measured by Crouch et al. (2014, $u/U_\infty \sim 0.5$) and Jux et al. (2018, $u/U_\infty \sim 0.35$). In the former case, the smaller velocity deficit is attributed to the more streamlined position of the mannequin; The trunk angle of attack is smaller ($\alpha \sim 5^o$ for the present model as compared to $\alpha = 12.5^o$ for that used by Crouch et al.) and the head and helmet do not contribute to the frontal area of the model in contrast to the one used by Crouch et al. Although the same model was used in the latter case, in the work of Jux et al., the measurement plane was further upstream ($x = 30$ cm) compared to the present case ($x = 80$ to 100 cm) and, hence, higher peaks of velocity deficit are expected in their work.

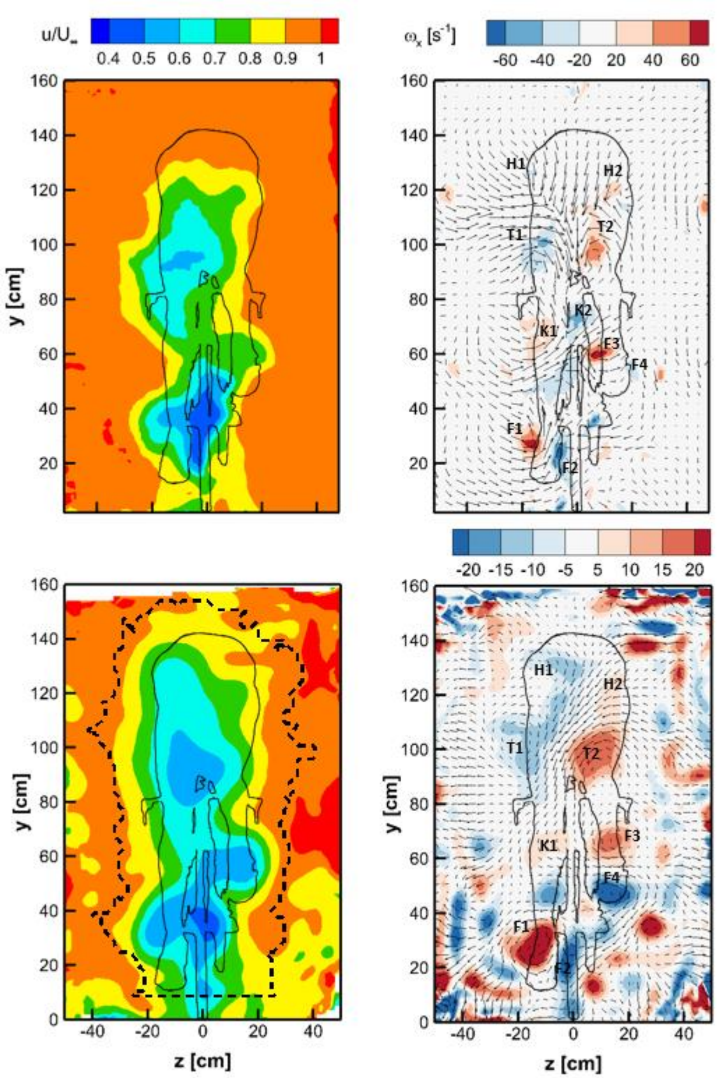

Figure 4.6: Contours of time-average streamwise velocity (left) and streamwise vorticity with in-plane velocity vectors (right) of the PWE (top) and the FWE (bottom) at $U_\infty = 14.33$ m/s and $U_\infty = 12.90$ m/s, respectively.

A second region of high velocity deficit is observed downstream of the wheel axis and the drivetrain configuration ($y \sim 40$ cm). In this region, the minimum velocity of $u/U_\infty \sim 0.45$ matches well the work of Crouch et al. (2016a) in terms of location and magnitude, despite the differences between the respective models. A region of strong downwash behind the back of the mannequin ($y \sim 120$ cm) is observed in Figure 4.6-right, with a peak vertical velocity of $v/U_\infty \sim -0.17$ that also agrees well with literature (Crouch et al. 2016a; Griffith et al. 2014, among others). Two distinct counter-rotating vortices (marked T1/T2 in Figure 4.6-right) originate from the cyclist's thighs and are fed by the downwash behind the model's back, as also documented in previous literature (Crouch et al. 2014). Other counter-rotating vortex pairs originate from the left foot (marked F1/F2) and from the right foot (marked F3/F4). The regions of streamwise vorticity emanating from the hips (H1/H2) are shearing regions, rather than vortex regions, stemming from the interaction between the downwash over the back of the mannequin and the surrounding streamwise velocity.

The measured time-average streamwise velocity and vorticity in the centre of the cyclist wake obtained from the *partitioned-wake* and *full-wake* experiments are generally similar and have been treated such in the discussion so far. However, differences are observed as well. As a consequence of the lack of seeding in the region close to the measurement boundary (see Figure 4.4-bottom), the spatial distribution of streamwise velocity and vorticity obtained in the FWE depicts non-physical spatial variations in this boundary region (Figure 4.6-bottom-left and right, respectively). Instead, the PWE velocity distributions are rather uniform in the boundary region (Figure 4.6-top-left). In the inner wake region, not being affected by a scarcity of seeding, the peak values of streamwise vorticity in the FWE are approximately 50% of those measured in the PWE. Apart from the geometrical differences, this is also attributed to the larger downstream location of the measurement plane in the former case (20 cm difference). Overall, it is concluded that the measured time-average streamwise velocity and vorticity obtained in the two experiments are in good agreement to each other and, as well, with existing work in the literature, which provides good confidence in the quality of the present measurement approaches.

4.4.2 Streamwise velocity fluctuations

The velocity fluctuations obtained from the *partitioned-wake* experiments are presented and discussed first. These are then compared to those obtained from the *full-wake* experiments. Two separated unsteady shear layers behind the lower left leg can be observed in Figure 4.7-left (marked S3/S4), exhibiting peaks of about $\sqrt{\overline{u'^2}}/U_\infty$ ~ 0.1. These shear layers bend inwards just below the knee due to the strong inward velocity component in this region (y ~ 50; z ~ -20, Figure 4.6-right), partly stemming from the counter-clockwise streamwise vortex K1. The shear layer originating from the top part of the extended leg (y ~ 90 cm and z ~ -15 cm) exhibits fluctuations of similar magnitude. Conversely, the fluctuations behind the bent leg are comparatively lower, with peaks of about $\sqrt{\overline{u'^2}}/U_\infty$ ~ 0.06, due to its more streamwise orientation. The location of counter-rotating streamwise vortex pairs originating from the thighs (T1/T2 Figure 4.6-right) and the shearing regions (H1/H2) coincides with two regions of high streamwise velocity fluctuations (marked T1/T2 and H1/H2 Figure 4.7-left) indicating that these flow structures are unsteady in nature. Hence, the presented time-average streamwise vorticity levels in Figure 4.6 are below the instantaneous peak values suggesting that insight into the instantaneous vortex topology may contribute to a better understanding of the streamwise vortex structures in the wake of a cyclist, possibly aiding in future drag minimization. Other maxima

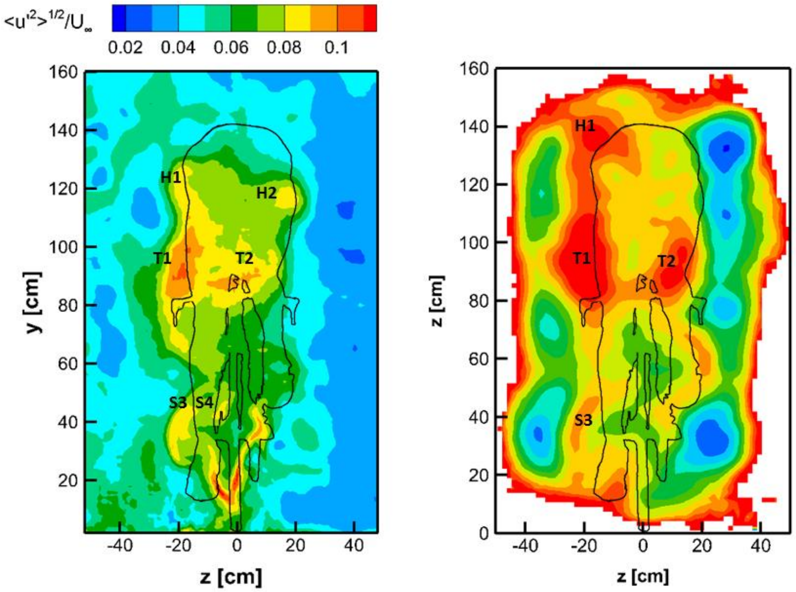

Figure 4.7: Contours of streamwise velocity fluctuations obtained from the *partitioned-wake* (left) and the *full-wake* experiments (right) at U_∞ = 14.33 and U_∞ = 12.90, respectively.

of the streamwise velocity fluctuations appear in the wake of the drivetrain and behind the lower part of the wheel (V-shape area).

Compared to the results of the PWE, the FWE velocity fluctuations are comparatively higher. This is attributed to a non-uniform distribution of seeding, and occasionally lack of seeding, during the measurements resulting in erroneous vectors in the instantaneous velocity fields. This deficiency is most pronounced at the boundaries of the domain where seeding is more scarce. For readability, therefore, fluctuations levels exceeding $\sqrt{\overline{u'^2}}/U_\infty > 0.14$ are blanked.

Outside of the wake of the mannequin, the root-mean-square of the streamwise velocity fluctuations reduces significantly, reaching a level of about 4% and approximately 6% of the freestream velocity in the case of the PWE and FWE, respectively. With an estimated freestream turbulence level in the wake of the seeding system of 1.9% (Jux et al., 2018), it is argued that the freestream turbulence intensity is likely overestimated due to PIV random errors. As a consequence, the contribution of the Reynolds stress term in the expression for the drag (second right-hand-side term in Equation 3.7) is overestimated, thus yielding an underestimation of the aerodynamic drag by approximately 0.15 N and 0.25 N in the case of the PWE and FWE, respectively.

4.4.3 Time-average pressure

At sufficient distance behind a bluff body, the contribution of the pressure term to the aerodynamic drag decays to zero due to the pressure recovery towards the freestream condition

(Terra et al. 2017). To understand the contribution of the time-average pressure term to the drag for the present downstream position of the wake plane, the pressure field distribution is investigated. Figure 4.8 depicts the spatial distribution of the *partitioned-wake* experiments pressure coefficient showing the presence of a large high pressure region (HP1) behind the upper back of the cyclist. This overpressure is attributed to the deceleration of the flow after passing the curved back of the cyclist. Lower in the wake plane, at $y \sim 90$ cm, the flow has separated over the lower back of the cyclist, resulting in a region of negative C_P (LP1). A second low pressure region, likely caused by a flow separation over the left foot and the rear wheel, is observed behind the left foot (LP2). The overall distribution of the time-average pressure coefficient matches well to the work of Blocken et al. (2013), despite the differences in model geometry and crank angle (symmetric leg position instead of the present asymmetric case). Finally it is observed that the spatial variation of the pressure coefficient is small (up to 0.03 between minimum and maximum C_p in the wake plane) and the pressure in most of the domain equals the freestream pressure. Hence, the contribution of the pressure term to the aerodynamic drag through Equation 3.7 is likely negligible (discussed in more detail in Section 4.5) and, therefore, the pressure reconstruction is omitted in the *full-wake* experiments.

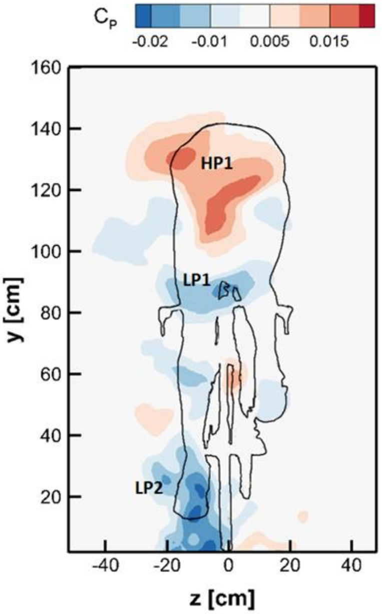

Figure 4.8: Pressure distribution obtained from the *partitioned-wake* experiments.

4.4.4 Repeatability and flow similarity

The *partitioned-wake* experiments are repeated within a narrow range of freestream velocities (12.5 m/s < U_∞ < 15 m/s) where the drag coefficient is constant (Grappe 2009) and, hence, the flow topology is expected to remain unaltered. The contours of $u/U_\infty = 0.9$ at five freestream speeds, depicted in Figure 4.9-left, coincide well and discrepancies of about 5% in non-dimensional streamwise velocity are observed between the different freestream conditions, indicating a good level of repeatability of the experiment. The *full-wake* experiments, in contrast, are conducted at $U_\infty = 4.5$ m/s and $U_\infty = 13$ m/s and, hence, flow Reynolds number effects are anticipated. Comparing the contours among the two speeds (Figure 4.9-right), it is observed that at the higher velocity ($\mathrm{Re} = 6 \times 10^5$ based on the torso length) the wake is narrower above y = 50 cm. This Reynolds number effect can at least partly be attributed to a transition to turbulence in the boundary layer developing over the bluff parts of the cyclist body (e.g. arms and legs), delaying separation, narrowing the wake and reducing the aerodynamic drag. The latter should also reflect in the obtained aerodynamic drag that is discussed in the next section.

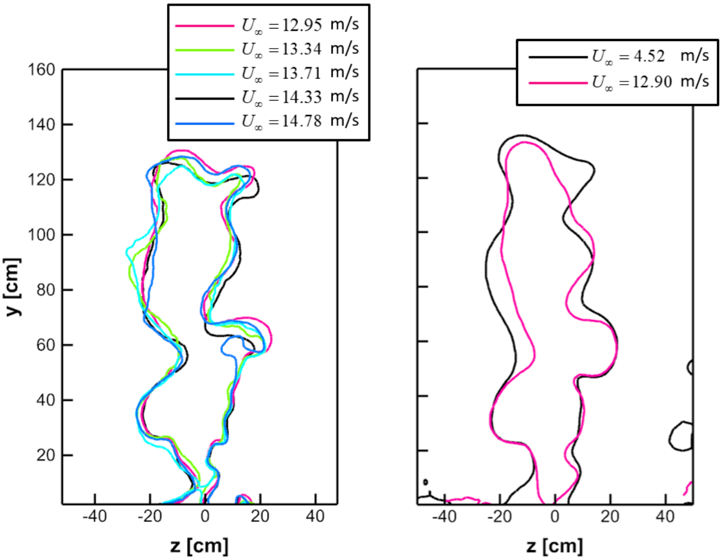

Figure 4.9: Contours of 0.8 u/U_∞ of *partitioned-wake* experiments (left) and *full-wake* experiments (right).

4.5 Drag estimation and resolution

Considering the unaltered flow topology at the different freestream velocities in the *partitioned-wake* experiments (Figure 4.9-left), the drag coefficient of the cyclist can be assumed constant and the aerodynamic drag is expected to scale quadratically with increasing velocity. Hence, despite the narrow range of freestream velocities, the drag force is expected to increase by almost 50%. This expected increase is clearly observed in Figure 4.10 depicting the resistive force obtained by the balance system (black symbols) and from the PIV wake rake (red symbols), using Equation 3.7, at five freestream velocities. The uncertainty of the time-average balance readings is below 0.2 N and, hence, error bars depicting their uncertainty are omitted. A quadratic fit through the five data points resulting from the PIV wake rake ($D = 0.143U_\infty^2$;

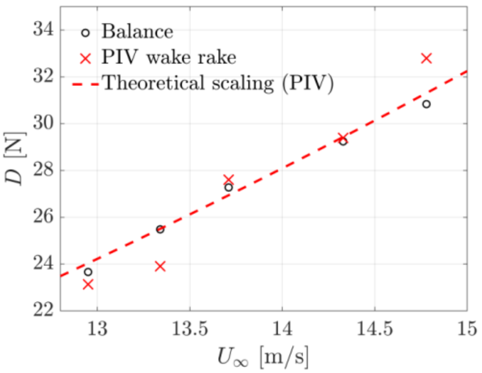

Figure 4.10: Time-averaged aerodynamic drag from the balance (black symbols) and the PIV wake rake (red symbols) at five freestream velocities. The red-dashed line depicts a quadratic fit through the latter ($D = 0.143U_\infty^2$).

red-dashed line) and (*0,0*) is included as well. The scatter in the obtained drag obtained from the PIV wake rake is 1.2 N, which is estimated from the root-mean-square of the residuals between the measured data and the quadratic fit. The assumption of constant drag coefficient does not hold in the case of the *full-wake* experiment considering the observed Reynolds number effects (Figure 4.9-right) and the model geometrical variations among measurements. Hence, the accuracy is determined by comparison to force balance data.

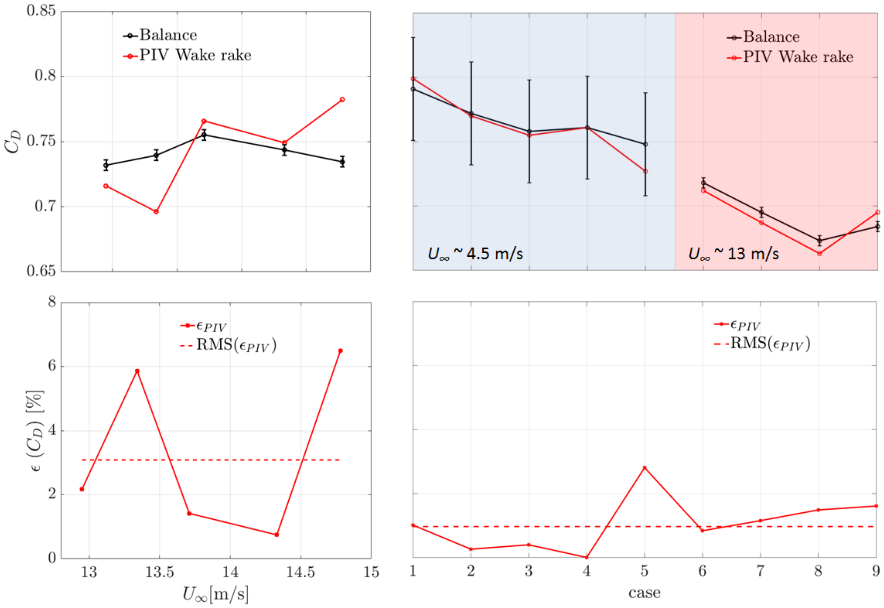

Figure 4.11: Aerodynamic drag from the PIV wake rake and the force balance (top) and the relative error of the drag of the PIV wake rake as a percentage of the balance data (bottom) for the *partitioned-wake* (left) and the *full-wake* experiments (right).

The accuracy of the drag estimation, or drag resolution, is evaluated comparing the drag coefficients obtained with the PIV wake rake with those obtained by force balance. Figure 4.11-top-left shows that the drag coefficients measured by the force balance in the PWE are relatively constant (black line) and the variations are obtained within 1.5% with increasing freestream velocity. The error bars on the time-average drag coefficient indicate the uncertainty of the mean value at one sigma level. Details on the computation of this uncertainty stemming from the different seeder positions are provided in the appendix A. In contrast to the measurements by the force balance, the variations observed in the drag coefficient obtained from the PIV wake rake are significantly larger (Figure 4.11-top-left; red line), illustrating the higher measurement uncertainty of this technique. Figure 4.11-bottom-left (solid-red line) shows the error in the drag coefficient measured by the PIV wake-rake approach relative to that obtained by balance measurements, which varies between 0.75% and 6.5%. Using Equation 4.1, a drag resolution of the PWE PIV wake rake of $\Delta C_D = 0.03$ or 30 drag counts, is obtained (Figure 4.11-bottom-left red dashed line).

In the FWE the drag obtained from the PIV wake rake (Figure 4.11 top-right red line) matches more closely to that of the force balance (solid black). Hence, the drag resolution, being approximately 10 drag counts (Figure 4.11-bottom-right black dashed line), is significantly below that of the PWE wake rake. The reduced accuracy, in the latter case, is attributed to the intrusiveness of the seeding rake in combination with the seeder traversing. The seeding rake, and in particular the supporting strut, affects the cyclist's approach flow and, hence, also its wake velocity deficit and aerodynamic drag. The extent of this intrusiveness depends on the position of the seeder with respect to the wind tunnel model and it is greatest when the two are laterally aligned. Despite filtering the balance data, so to reduce the effect of the seeder's intrusiveness on the aerodynamic drag measured by the force balance (see Appendix A for more details), it is not expected to be negligible. Also the measured velocity, at each seeder position is, to some extent, affected by the seeder. Although, these effects, as a result of changing seeder position, have not been quantified in more detail, it can be safely assumed that they negatively affect the present PIV wake rake aerodynamic drag accuracy.

Concerning the drag accuracy and the computation of the aerodynamic drag in the FWE, it is noted that the chosen integration area is bounded by the contour depicted in Figure 4.6 in order to omit the region with erroneous velocity statistics (details on the algorithm defining this contour is provided in Appendix B). Despite cropping the integration area, however, it is expected that some of this velocity error propagates into the aerodynamic drag. This suggests that the drag resolution of the human-scale PIV wake rake may be further decreased using a more tailored (larger) seeder so to avoid the lack of seeding on the wake boundaries.

Apart from the drag resolution, it is observed that the cyclist drag coefficient at a freestream velocity of 4.5 m/s (Figure top-right; marked blue) exceeds that at 13 m/s (marked red) by approximately 15%. These Reynolds number effects and the corresponding changes in aerodynamic drag are further investigated in Chapter 5.

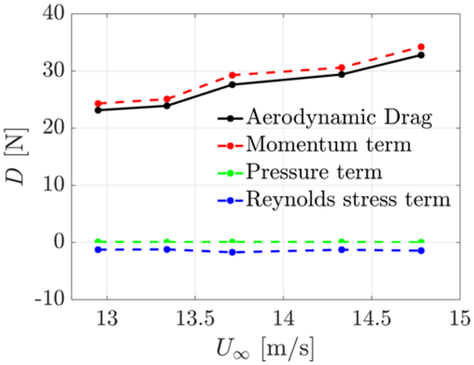

Figure 4.12: Time-average aerodynamic drag from the *partitioned-wake* experiments at five freestream velocities including the contributions of the momentum, pressure and Reynolds stress terms.

Finally, for the PWE, the separate contributions of the momentum term, Reynolds stress term and pressure term in Equation 3.7 to the overall aerodynamic drag are depicted in Figure 4.12. The contribution of the latter is approximately zero at all freestream conditions, which was expected from the small zero-level deviations in the distribution of the pressure coefficient (Figure 4.8-right). Hence, the pressure reconstruction can be omitted in future cyclist drag estimations with a wake plane downstream position $x/L > 2.2$, where L is the characteristic length scale representative for the wake topology (hip width in this case). In the FWE the wake plane is at $x/L = 2.7$ and the contribution of the pressure term is negligible, which significantly simplifies the evaluation of the aerodynamic drag. For both the PWE and FWE, the Reynolds stress term consistently contributes by approximately 5% to the drag and cannot be neglected. Finally, the momentum term dominates the air resistance accounting for the remaining 95%.

5

CYCLIST REYNOLDS NUMBER EFFECTS AND DRAG CRISIS DISTRIBUTION

A successful design of low-drag skinsuits relies, among others, on an understanding of Reynolds number effects in complex cyclist flow. This chapter is dedicated to the description of these Reynolds number effects and the associated drag crisis phenomenon. The near-wake of a cyclist mannequin is mapped using robotic volumetric PIV at different freestream velocities spanning a wide Reynolds number range. The results reveal typical bluff body features in the flow around the cyclist's limbs, such as large regions of separated flow. Moreover, it is observed that, in addition to the limb width, counter rotating streamwise vortex pairs govern the size of the reverse flow area. Finally, the distribution of the critical velocity, the speed at which the drag coefficient is minimal, is estimated along the cyclist limbs by relating the change in wake with increasing velocity to that of the behaviour of the drag coefficient.

Part of the work presented in this chapter is published in:

Terra W, Sciacchitano A, Scarano F (2020), *Cyclist Reynolds number effects and drag crisis distribution*. J Wind Eng Ind Aerodyn 200 104143

5.1 Introduction

The present chapter investigates the flow around body segments of a full-scale cyclist model in time-trial position riding at different speeds. Robotic volumetric Particle Image Velocimetry (PIV) is employed for the cyclist near-wake measurements. The experiment aims at characterizing Reynolds number effects along the cyclist's body and understanding the circumstances for the drag crisis to occur (introduced in Section 1.3). The attention of the present work is on the stretched leg, which produces more drag (Griffith et al. 2014) and where bluff body Reynolds number effects are expected more pronounced in comparison to the flexed leg. The position of the two arms is rather symmetrical to the cyclist's median plane, and, so, in addition to the leg, the left arm is chosen for the investigation. To understand the highly complex cyclist flow, a general near-wake flow description at typical time trial speed is provided first, before the flow Reynolds number effects are discussed. The critical flow condition, corresponding to minimal drag coefficient, is inferred from the local wake width and its distribution along the arm and leg is finally presented so to provide insight into what governs the cyclist drag crisis and how the drag of the cyclist may be minimized by dedicated skinsuits designs in the future.

5.2 Methodology

To assess the existence of the drag crisis on individual sections of the cyclist's body, the local drag coefficient of those sections must be evaluated. In this work, the local C_D of individual body parts is related to the near-wake flow properties. Roshko (1955) suggested the use of the wake width to characterize the bluffness of an object. In a later work (Roshko 1961) a model was advanced, where the drag coefficient is directly proportional to the normalised wake width d_w/d (d being the object width) and the base pressure C_{pb}:

$$C_D = -C_{pb}\frac{d_w}{d} \tag{5.1}$$

However, the model described by Equation 5.1 has shown good agreement with experimental data only in the sub-critical flow regime (Roshko, 1961). In the critical regime, instead, the change of the drag coefficient can be expressed in terms of the change in wake width (Rodriguez et al. 2015):

$$\frac{C_{D,1}}{C_{D,2}} = \alpha_d \frac{d_{w,1}}{d_{w,2}} \tag{5.2}$$

where $\alpha_d \sim 2$ is an empirical constant and the subscripts 1 and 2 refer to sub- and super-critical Reynolds numbers, respectively. The schematic description of the bluff body wake presented in Figure 2.4 is repeated here, now also illustrating the change in drag coefficient and wake width between sub-critical and the critical condition (Figure 5.1). Based on the available literature, the relation between the drag coefficient and the wake width cannot be considered valid for quantitative analysis. It is generally used, however, to draw qualitative conclusions when large variations in the local drag coefficient are associated with variations of the Reynolds number.

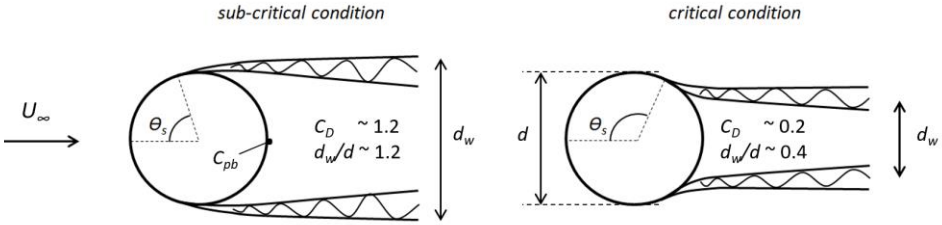

Figure 5.1: Sketch of separated shear layers and wake width in *sub-critical* (left) and late *critical* condition (right).

In the present work, the wake width inferred from experiments is inspected over a range of freestream velocity to detect the occurrence of drag crisis. The critical flow condition is associated with a specific velocity, the critical velocity V_{crit}, instead of critical Reynolds number Re_{crit}. This choice enables a direct assessment of whether the different body parts of the cyclist racing at typical time-trial speed operate in the sub-critical, critical, or the super-critical flow regime.

5.3 Cyclist experimental apparatus and procedures

5.3.1 Wind tunnel apparatus and cyclist mannequin

The experiments are conducted in the OJF wind tunnel using the same cyclist model used for the human-scale wake rake measurements (Section 4.3.1). In the present experiments, the bike is equipped with a Pro 3-spoke *Textreme* front and Pro disc *Textreme* rear wheel with 25 mm tubular tires. Except for the *Giro* Rivett TT helmet, the model is not wearing garments. In the present work, the natural drag crisis is investigated, in the absence of surface roughness control. The mannequin's surface roughness $k < 0.1$ mm is estimated after surface polishing treatment. For a detailed overview of the characteristics of the bike and cyclist mannequin the reader is referred to Figure 4.1 and Table 4.1. To avoid model vibration during the measurements, which would otherwise occur above $U_\infty \sim 16$ m/s, four steel wires of 2 mm diameter connect the bike frame to the floor (Figure 5.3-right).

The critical Reynolds number distribution is, among others, affected by the changing cross-sectional area shape and inclination of the cyclist's body part axis. These geometrical features are illustrated in Figure 5.2 reporting different cross-sections of the arm and stretched leg. As the leg narrows from the hip towards the foot, also the 'bluffness' of the leg changes. Especially closer to the foot ($y = 275$ mm; black cross-section), the aspect ratio d/l of the leg's cross-section decreases in comparison to the knee and upper leg from approximately 0.65 to 0.85, respectively. Changes in cross-sectional shape of the arm are accounted as well.

To allow a non-dimensional analysis of the cyclist's near-wake flow, a human body coordinate ζ is introduced that follows the cyclist limbs, namely the upper arm ζ_A ($\overline{FG}$: elbow to shoulder joint), the upper leg ζ_{UL} ($\overline{DE}$: hip to knee joint) and the lower leg ζ_{LL} ($\overline{CD}$: knee to ankle joint, see Figure 5.2-top-left). The origin ($x_\zeta = 0;\ z_\zeta = 0$) of the body sections depicted in Figure 5.2-right is chosen at the intersection of the line segments connecting the different limb joints and the different horizontal y-planes.

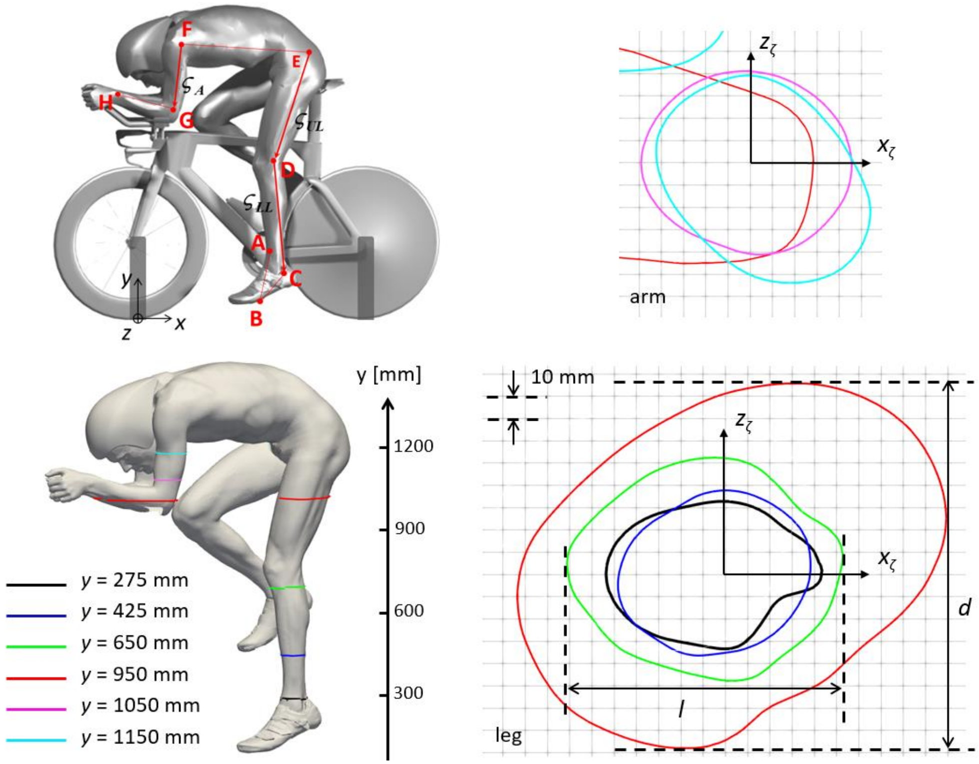

Figure 5.2: Cyclist mannequin human body coordinate system (top-left) and positions of considered cross sections (bottom-left). Contours of the different cross-sections along the arm (top-right) and leg (bottom-right).

5.3.2 Measurement apparatus and data analysis

Considering the three-dimensional complexity of the rider-bike geometry and the large size of the measurement domain, a robotic volumetric PIV (Section 3.4.2) system is employed. The large seeder (200 HFSB generators; 1 (H) × 0.5 (W) m^2; Figure 4.2) is installed in the settling chamber of the OJF (Figure 5.3). The seeded streamtube in the test section upstream of the cyclist is approximately 60×30 cm^2. The seeding array is translated vertically to cover the whole

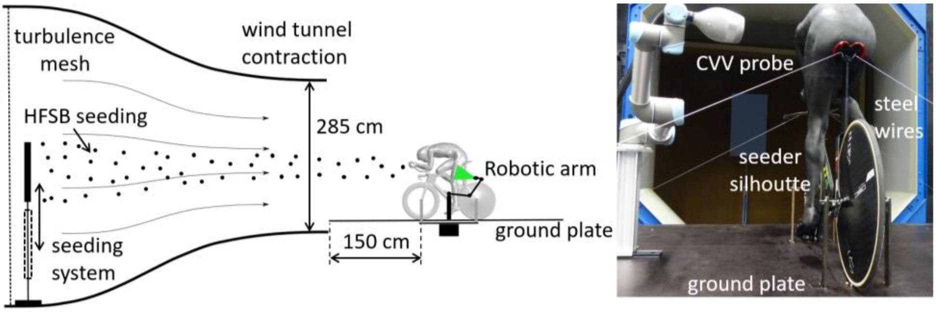

Figure 5.3: Wind tunnel experimental setup: A schematic view (left) and a photo (right) depicting the robotic volumetric PIV components.

cross-section of the rider. The average tracer concentration during the experiments varies from 0.2 to 1 bubbles/cm^3 depending on the freestream velocity (Caridi et al. 2016). The presence of the seeding system is reported to increase the freestream turbulence intensity from 0.5% to approximately 0.8% (Giaquinta, 2018).

The CVV system features four CMOS cameras arranged in a compact holder. The CVV probe is installed on a 6-degree-of-freedom Universal Robots A.S. *UR5* robotic arm that translates and rotates the optical head with a positional repeatability of ±0.03 mm and ±0.01^o, respectively. Aerodynamic interference effects from the robotic PIV system are within 2% (Giaquinta 2018). A Quantronix *Darwin Duo* Nd:YLF laser (25 mJ pulse energy at 1 kHz) is directed, into an optical fibre and transmitted towards the LaVision GmbH *Minishaker Aero* CVV probe. The measurement volume features a conical shape with cross-sections of approximately 10 cm and 40 cm diameter at 20 cm and 60 cm from the probe, respectively. The main specifications of the system are summarized in Table 5.1.

To cover the relevant range of Reynolds number to investigate the drag crisis, the measurements are conducted within the velocity range $U_\infty = [5\ 10\ 15\ 20\ 25]$ m/s. The corresponding Reynolds number ranges from 2.3×10^5 to 1.2×10^6 based on the torso chord (c = 700 mm).

Table 5.1: Coaxial Volumetric Velocimeter specifications.

Optics	Focal length	4 mm
	Cameras numerical aperture	11
Imaging	Tomographic aperture (horizontal; vertical)	4^o; 8^o
	Sensor size	640×475 px^2
	Pixel pitch	4.8 µm
	Maximum acquisition frequency	758 Hz
	Bit depth	10
Illumination	Nominal pulse energy	25 mJ
	Wavelength	527 nm

A geometrical calibration of the system is performed following Jux et al. (2018). The time-average velocity and the velocity fluctuations are obtained adopting the multi-Δt 3D-PTV approach (Saredi et al. 2020) using the Shake-the-Box (STB, Schanz et al. 2016) double-frame algorithm in *Davis 10* from LaVision GmbH. The pulse separations of the initial measurement, used as predictor, Δt_1 is chosen to yield a tracer displacement of approximately 3 mm in the freestream. The measurement dynamic velocity range of the measurement is enlarged with a second acquisition of image pairs separated by Δt_2 corresponding to 10 mm displacement in the freestream. At each position of the CVV, a total of 2,000 and 6,000 image pairs are collected at Δt_1 and Δt_2, respectively, at a rate of 300 Hz, to produce statistically converged velocity estimates. The measurements are conducted scanning through 25 different probe positions for each setting of the freestream velocity, resulting in a total of 250 data sets.

5.3.3 Image pre-processing and data reduction

The background noise and reflections in the acquired PIV images are mitigated applying a Gaussian smoothing in space (kernel size of 5×5 pixels) and a high-pass frequency filter (Sciacchitano and Scarano, 2014). The flow velocity information is then retrieved via Lagrangian Particle Tracking (Shake-the-Box algorithm, Schanz et al. 2016, in the LaVision *DaVis 10* software). Velocity statistics are obtained from the Lagrangian velocity ensemble, combining all CVV probe positions, within cubic bins of $3\times3\times3\ \mathrm{cm}^3$ with 75% overlap (Agüera et al. 2016) requiring at least 20 particles per bin.

The wake width is estimated from the obtained velocity statistics as the distance between the two shear layers. Figure 5.4 depicts the non-dimensional time-average streamwise velocity, $\overline{u}/U_\infty$ (left) obtained in the near-wake of the knee at $y = 650$ mm and $x_\zeta/d = 0.8$, d being the width of the cyclist's leg at the given height y. Norberg (1986) suggested to evaluate the wake width from the distance between the velocity fluctuations peaks in the shear layers (Figure 5.4-middle). However, velocity fluctuations are less accurately captured with the CVV technique (Schneiders et al. 2018). The location of peak velocity fluctuations is known to coincide with the velocity inflection points (e.g. White and Nepf 2008; Unnikrishnan and Gaitonde 2019) and, hence, the wake width is, instead, evaluated as the distance between the velocity inflection points, i.e. the distance between the peaks of $|\partial\overline{u}/\partial z|$ (Figure 5.4-right). The wake width is estimated at $x_\zeta/d = 0.8$, d being the width of the cyclist's leg at the given height y. The latter choice comes as a trade-off between the need to avoid the measurement noise stemming from reflections close to the model and the detectability of $\partial\overline{u}/\partial z$ peak position with increasing distance from the model. The position of the left and right shear layer is measured along the y-direction. The variations along y are regularized using a moving average filter (kernel size of 5 points, 37.5 mm) to reduce measurement uncertainties.

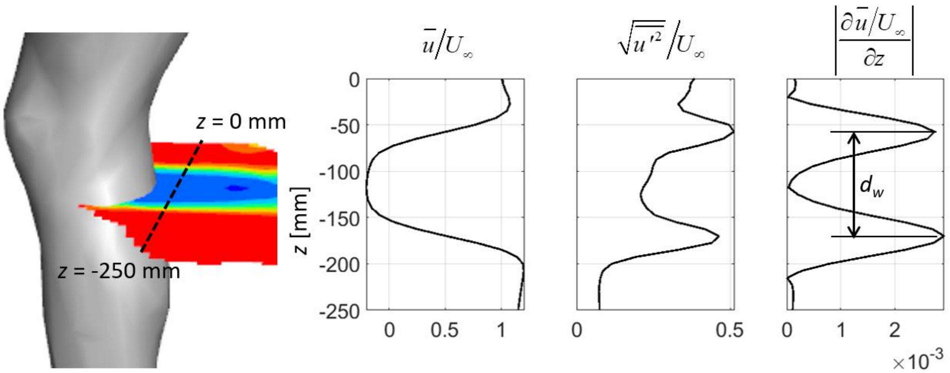

Figure 5.4: Wake width estimation: Profiles of streamwise velocity (left), velocity fluctuations (middle) and spanwise velocity gradient (right).

5.3.4 Experimental uncertainty

The uncertainty of the time-average velocity stems mainly from the unsteadiness of the cyclist's wake and from the random errors in the CVV measurements. The relative random uncertainty at 95% confidence level is evaluated as $\varepsilon_{\bar{u}} = k\sigma_u \big/ \left(U_\infty \sqrt{N_p}\right)$, σ_u being the standard deviation of the measured streamwise velocity, N_p the number of tracer particles per bin and $k = 1.96$ the coverage factor. In the freestream ($N_p \sim 5000$; $\sigma_u/U_\infty \sim 0.07$) and near-wake ($N_p \sim 500$; $\sigma_u/U_\infty \sim 0.5$ in the shear layers), the uncertainty values are approximately 0.2% and 4.5%, respectively. The uncertainty of the wake width evaluation is estimated as $\varepsilon_{dw} = \sqrt{2}\,h \sim 10$ mm, being $h = 7.5$ mm the spacing between adjacent velocity vectors. Furthermore, the uncertainty of the critical velocity, $\varepsilon_{V,crit}$ is defined as the velocity range in which $|d_{w,Vcrit} - d_{w,v}| < \varepsilon_{dw}$, $d_{w,Vcrit}$ being the wake width at the critical velocity and $d_{w,V}$ the wake width at neighbouring freestream speeds. The minimum uncertainty of the critical velocity, $\varepsilon_{V,crit} = 2.5$ m/s is related to the resolution of the selected increase in freestream velocity.

Finally, note that the effect of blockage (4% model blockage) is assumed negligible, considering the small estimated velocity correction for an open-jet wind tunnel ($\sim 1.01U_\infty$; Terra et al. 2019) in comparison to the freestream velocity resolution.

5.4 Results

5.4.1 Global flow structure and topology

The main features of the flow around the cyclist are surveyed at freestream velocity $U_\infty = 15$ m/s, typical of race conditions. Figure 5.5 depicts contours of the time-average streamwise velocity and streamwise velocity fluctuations (right) over multiple horizontal and vertical planes. Recirculation regions are identified by iso-surfaces of null streamwise velocity in the wake of the leg, upper arm and hip. The arm's recirculation region is relatively wide at the shoulder as a consequence of interference with the head wake (marked in

Figure 5.5 top-left). The recirculation region narrows from the shoulder towards the elbow and disappears at the latter junction. The latter is firstly ascribed to a turbulent separation on the elbow as a consequence of the presence of the upstream lower arm. Secondly, the up-wash of air resulting from the triplet of streamwise vortices emanating from the elbow (Figure 5.6-left) injects high momentum fluid into the arm's wake and displaces the separation to the upper region of the arm. The latter resembles the flow topology across the free end of a circular cylinder in cross flow (see Section 2.2.3).

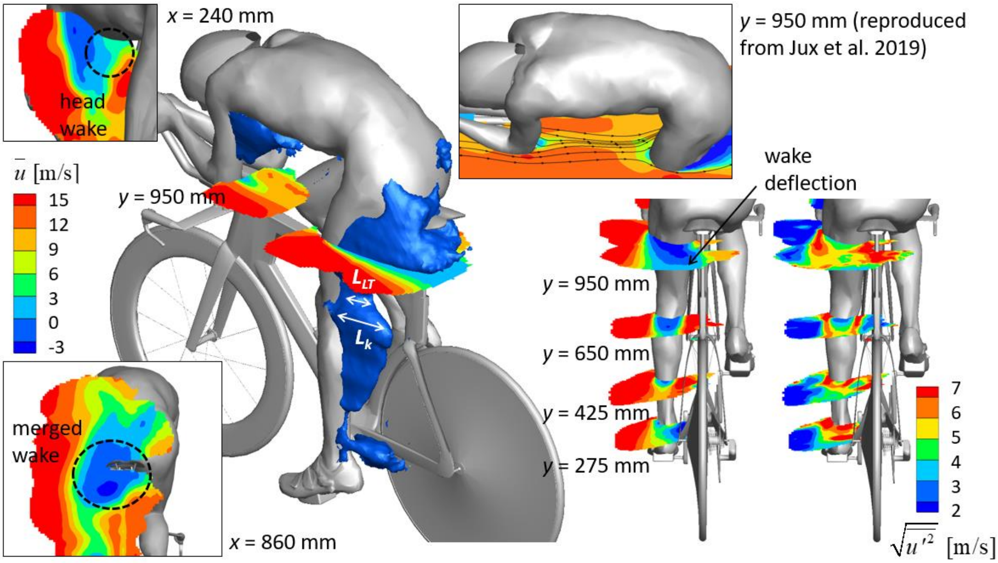

Figure 5.5: Contours of time-average streamwise velocity (all subfigures except that on the right), streamwise velocity fluctuations (right subfigure) and an iso-surface of zero streamwise velocity.

Along the leg, from ankle to hip, the width and downstream extension of the recirculation region increases, partly due to the thickening of the leg. It is remarkable, though, that the geometry of the recirculation region is not directly proportional to the local thickness of the body limbs: for example, the extension of the recirculation region at the lower thigh is approximately 45% of that at the knee (marked L_{LT} and L_k in Figure 5.5, respectively), while the local thickness of the leg instead increases by approximately 10%. This reduction stems from the action of a counter rotating vortex pair that transfers high speed fluid from the upper leg (indicated in Figure 5.6-right). As a result, the streamwise velocity downstream of the knee is increased and separation delayed. Similarly, the shank vortices are responsible for the suppression of the recirculation region towards the ankle. Despite the wake of the ankle being governed by streamwise vortex pairs, a small recirculation is expected in that region. The measurements do not capture it, likely due to its shallow form and the limited spatial resolution. The recirculation region is widest close to the junction of the legs (see Figure 5.5-right; y = 950 mm), partly resulting from the leg's tapered geometry. Additionally, the wakes of the left and right leg merge at $y > 900$ mm (indicated in Figure 5.5-bottom left), somehow similarly to that of two closely spaced side-by-side cylinders (Zdravkovich 1987), which further increases the wake width. The observed deflection of the wake (indicated in Figure 5.5-right) is also ascribed to the merged wakes.

The lower section of the leg (Figure 5.5-right; $y = 425$ mm and $y = 650$ mm) exhibits a flow behaviour more closely resembling that of a two dimensional bluff body: two shear layers emanate from the sides of the leg, bounding a region of flow recirculation. Outside of the shear layers, the flow velocity is close to the free-stream value. Closer to the junction of the two legs (Figure 5.5-right; $y = 950$ mm), the inner shear is not clearly observed anymore and, instead, a wide turbulent region is present downstream of the seat post, which may be ascribed to the leg's turbulent approach flow stemming from the upstream arm (discussed in next paragraph). The flow across the foot is characterized by a pair of counter-rotating streamwise vortices (Figure 5.6-right) and an interaction with the flow across the rear wheel and the bike's left crank, resulting in a sidewise deflection of the recirculation region towards the bike (Figure 5.5-right; $y = 275$ mm). Finally, the main counter-rotating vortex pair originating from the hips and thighs and well documented in the literature (see Section 2.3.2), are observed here too (marked in Figure 5.6-middle).

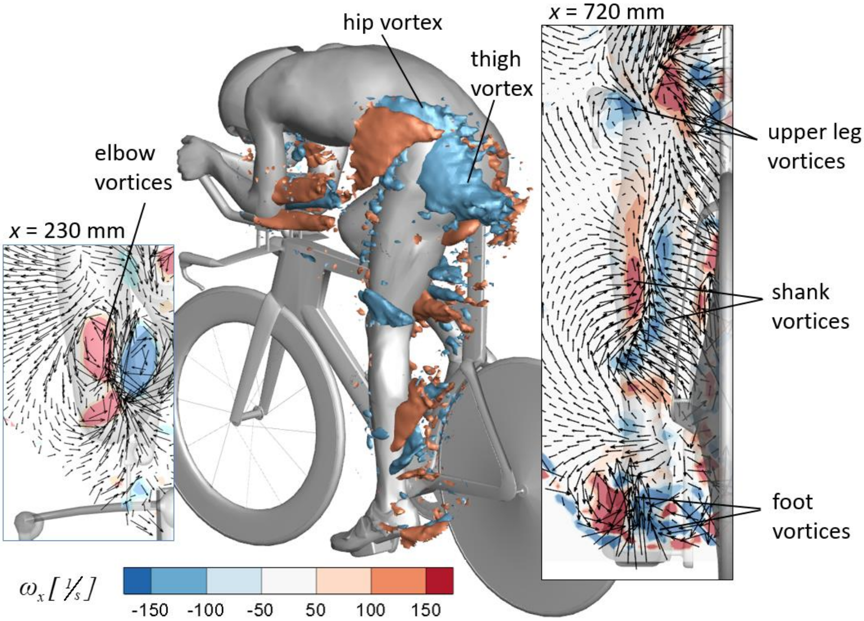

Figure 5.6: Time-average streamwise vorticity (contours and iso-surfaces at -120 and 120 rad/s in blue and red, respectively) and in-plane vectors downstream of the upper arm and the leg (left and right, respectively).

The present measurement domain excludes the area downstream of the arm and upstream of leg between 420 mm $< x <$ 580 mm. To understand the interaction between the flow across the arm and leg, the data collected by Jux et al. (2018) is used to depict streamlines between the

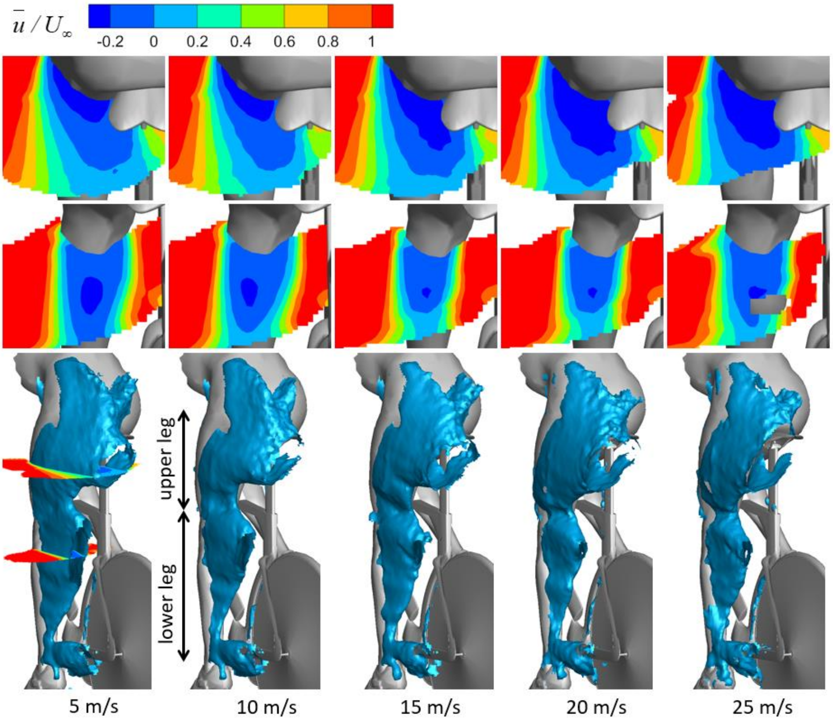

Figure 5.7: Contours of non-dimensional streamwise velocity at *y* = 950 mm (top) and *y* = 650 (middle) and iso-surfaces of $\bar{u}/U_\infty$ = 0.2 (bottom).

two (Figure 5.5-top-right). It is observed that the outside of the left upper leg is mostly exposed to undisturbed flow, while the flow across the inside of the upper leg is governed by disturbed flow emanating from the arm.

Finally, it is noted that the wakes emanating from the steel wires have not been observed in the time-average flow field and, hence, their effect on the present results is assumed negligible. This is attributed to the relatively small size of the wires and the corresponding wakes in comparison to the size of the cyclist model and that of the spatial bins used to average the Lagrangian velocity.

5.4.2 Reynolds number effects across the individual body parts

The cyclist's stretched leg

Figure 5.7 depicts contours of dimensionless streamwise velocity $\overline{u}/U_\infty$ in the horizontal planes *y* = 950 mm (top) and *y* = 650 mm (middle) and iso-surfaces of $\overline{u}/U_\infty$ = 0.2 (bottom). From the latter it is observed that the wake of the lower leg and the knee generally narrows and shortens between U_∞ = 5 m/s and 20-25 m/s. Specifically the length of the recirculation region, *L/d*, at *y* = 650 mm (Figure 5.7-middle) decreases monotonically by about 25% from approximately L/d = 2.2 to L/d = 1.7, respectively (see also Table 5.2). Similarly, also the peak reverse flow velocity $\left|\overline{u}_{\min}\right|$ decreases by 25% from -0.24 to -0.18. Closer to the foot, at y = 425 mm, the recirculation length decays by approximately 35% between U_∞ = 5 m/s and 25 m/s. These trends are similar to those reported for a spherical flow between sub-critical and critical conditions (Constantinescu and Squires 2004), suggesting that the critical condition at the knee and the lower leg occur approximately at 20 m/s and 25 m/s, respectively. The reported Reynolds number effects for cylinder flow in the critical regime, instead, are partly opposite, with an increasing length of the recirculation region throughout the critical regime (e.g. Rodriguez et al. 2015; Table 2.1). The similarity to the flow around a sphere may be related to the presence of the streamwise vortices dominating the wake of the leg, whereas similar vortical structures characterize instantaneous spherical flow topology (see Section 2.1.1).

In contrast to the lower leg, the wake of the upper leg generally widens and elongates between U_∞ = 5 m/s and U_∞ = 20 m/s (Figure 5.7-bottom). At y = 950 mm, the recirculation region clearly grows in size between U_∞ = 10 m/s and 20 m/s (Figure 5.7-top). The relative increase in reattachment length and peak reverse velocity in the latter range of freestream speed is approximately 10% (Table 5.2). This particular behaviour is also observed comparing the profiles of streamwise velocity obtained at x_ζ/d = 0.8. The recirculation region is narrow at U_∞ = 10 m/s (marked W_{10} in Figure 5.8-top row), in relation to its width at 20 m/s (marked W_{20}). The Reynolds number effects in the wake of the upper leg are opposite to those observed at the lower leg, which suggests a different mechanism is governing its wake behaviour. This mechanism is addressed later in this section.

Table 5.2: Characteristic velocities and dimensions of recirculation region of the flow across the leg at different y-positions.

U_∞ [m/s]	max reverse velocity [$\overline{u}/U_\infty$]			reattach length [L/d]			Wake width [d_w/d]		
	at y-position [mm]			at y-position [mm]			at y-position [mm]		
	425	**650**	**950**	**425**	**650**	**950**	**425**	**650**	**950**
5	-0.10	-0.24	-0.27	1.46	~2.2	1.58	0.91	1.14	1.23
10	-0.06	-0.22	-0.27	0.85	2.02	1.59	0.70	1.14	1.20
15	-0.08	-0.21	-0.28	1.23	1.70	1.70	0.74	1.02	1.34
20	-0.08	-0.18	-0.29	0.90	1.70	1.85	0.61	1.00	1.30
25	-0.09	-0.22	-0.29	0.80	1.80	~1.80	0.57	1.00	1.25

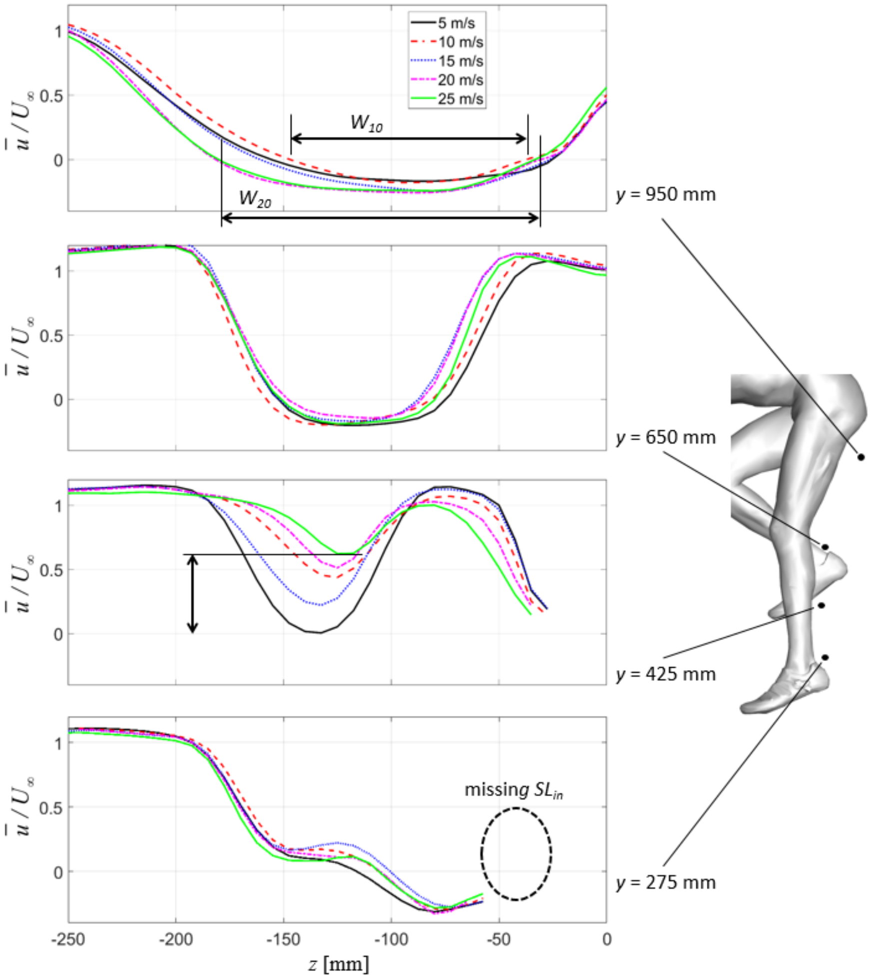

Figure 5.8: Spanwise profiles in the near-wake of the leg of non-dimensional time-average streamwise velocity.

Among the different velocity profiles, the Reynolds number effects are possibly most pronounced at $y = 425$ mm (Figure 5.8-third row). At this location on the leg, the minimum wake velocity increases from approximately $\bar{u}/U_\infty = 0$ to 0.6 at $U_\infty = 5$ m/s and 25 m/s, respectively (difference is marked), as a result of the corresponding decrease of the length of the recirculation region (see Table 5.2). This comparison among the different locations on the leg suggests that the relative reduction of the wake width peaks around $y = 425$ mm.

The non-dimensional wake width, estimated from the spatial gradient of the streamwise velocity profiles, is depicted in Figure 5.9-left at various different y-positions along the leg. At $y = 425$ mm d_w/d generally decays over the full speed range (solid red line), comparable to the drop of the drag coefficient of cylinders and spheres between sub-critical and late critical conditions. The wake width decreases over 30% between 5 and 25 m/s, exceeding the reduction of d_w/d at any other location on the leg. The critical velocity is determined as the speed at which d_w/d is minimal. At the lower leg, however, a plateau at the higher speeds, indicating the proximity of a minimum wake width, is missing; hence, it is concluded that the critical velocity sits beyond the present range of freestream velocity. At the mid-section of the leg, y = 545 mm and y = 650 mm, a similar drop of the wake width is observed between 5 and 15 m/s. In contrast to the lowest part of the leg, a plateau of relatively constant width is observed around 20-25 m/s (solid black and dashed red lines, respectively). This implies that the critical velocity is within the range of measured speeds and approximately equal to 20-25 m/s.

While the variation of the wake width at the lower leg is somehow similar to the isolated cylinder and spherical flow, the observations at the upper leg are different. Between 5 and 10 m/s the upper leg wake width drops, followed by a significant increase between approximately 10 and 20 m/s (y = 845 mm and y = 950 mm in Figure 5.9-left; dash-dot cyan line and dotted blue line, respectively). The former drop is associated with the transition from the sub-critical into the critical regime. The subsequent steep increase cannot be associated with the drag crisis mechanism for an isolated bluff body. It may be ascribed, instead, to the presence of the upstream arm. When the flow across the upper arm transitions from sub-critical to critical, its wake narrows and, hence, the flow upstream of the leg experiences a reduction of velocity deficit. As a consequence, the leg's wake width increases, similar to the increase in drag coefficient of the trailing one of two tandem cylinders (Section 2.2.2). Hence, limb flow interaction seems to play an important role in the Reynolds number effects on the cyclist upper leg, in contrast to the lower leg, which can be considered a more isolated geometry. A discussion on the wake width Reynolds number effects of the upper arm is presented in the next section.

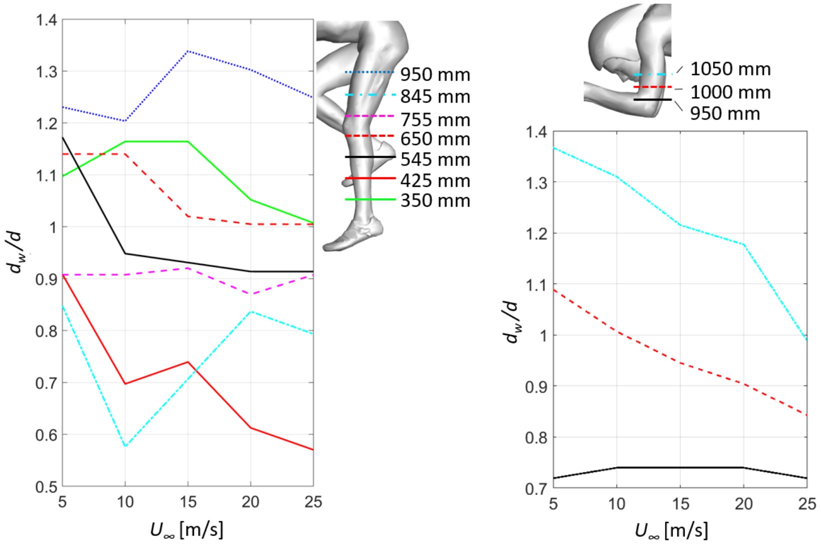

Figure 5.9: Non-dimensional wake width at increasing freestream velocity along the leg (left) and the arm (right).

The upper arm

The wake of the arm features a triangular shape with the apex above the elbow. Downstream of the latter, the streamwise velocity is largely Reynolds number invariant (wake marked in Figure 5.10-top-left). This absence of Reynolds number effects is attributed to a turbulent boundary layer that develops over the upstream lower arm. Above the elbow, the wake generally narrows between U_∞ = 5 and 25 m/s (marked d_w in Figure 5.10-top-left and right), although this narrowing is not as significant as for the leg and hip. Close to the trunk-arm junction clear Reynolds number effects in the wake of the arm seem to be absent possibly as a consequence of the proximity of the head (marked in Figure 5.10-top-right).

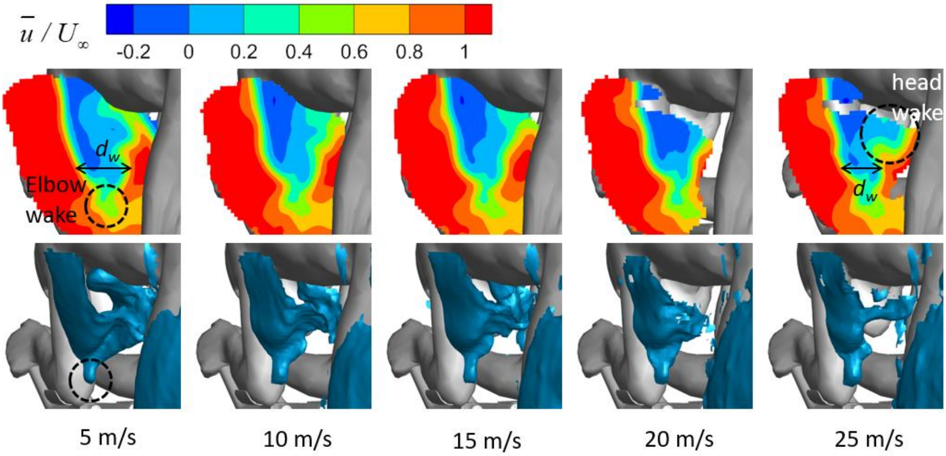

Figure 5.10: Contours of non-dimensional streamwise velocity at x = 240 mm (top) and iso-surfaces of $\bar{u}/U_\infty$ = 0.2 (bottom).

The wake of the head also poses a problem in the identification of the shear layer at the inside of the upper arm. The depicted profiles of streamwise velocity in Figure 5.11 highlight a wide profile scatter among the different speeds on the inside of the arm at y = 1100 (marked by dashed circle in second row). Hence, at this location the wake width cannot be determined using the present methodology. On the outside of the arm, instead, the shear layers can easily be detected and a significant inward relocation of the outer shear layer is observed (marked ΔSL_{out}). At the shoulder, where only the outside of the arm is exposed to the air flow, similar Reynolds number effects are observed (y = 1200 mm; Figure 5.11-top row). At the mid-segment of the upper arm the location of the outer shear layer is rather invariant, while the inner shear layer shifts inwards (marked ΔSL_{in} in Figure 5.11-third row). Finally, at the elbow it is observed that the velocity does not decrease below approximately 0.2 with little to no differences at the different speeds. The closely spaced profiles indicate the negligible variation of the elbow wake width, which is depicted in Figure 5.9-right (solid black line). The wake width in the mid-segment of the arm, y = 1000 and y = 1050, monotonically decays over the full range of

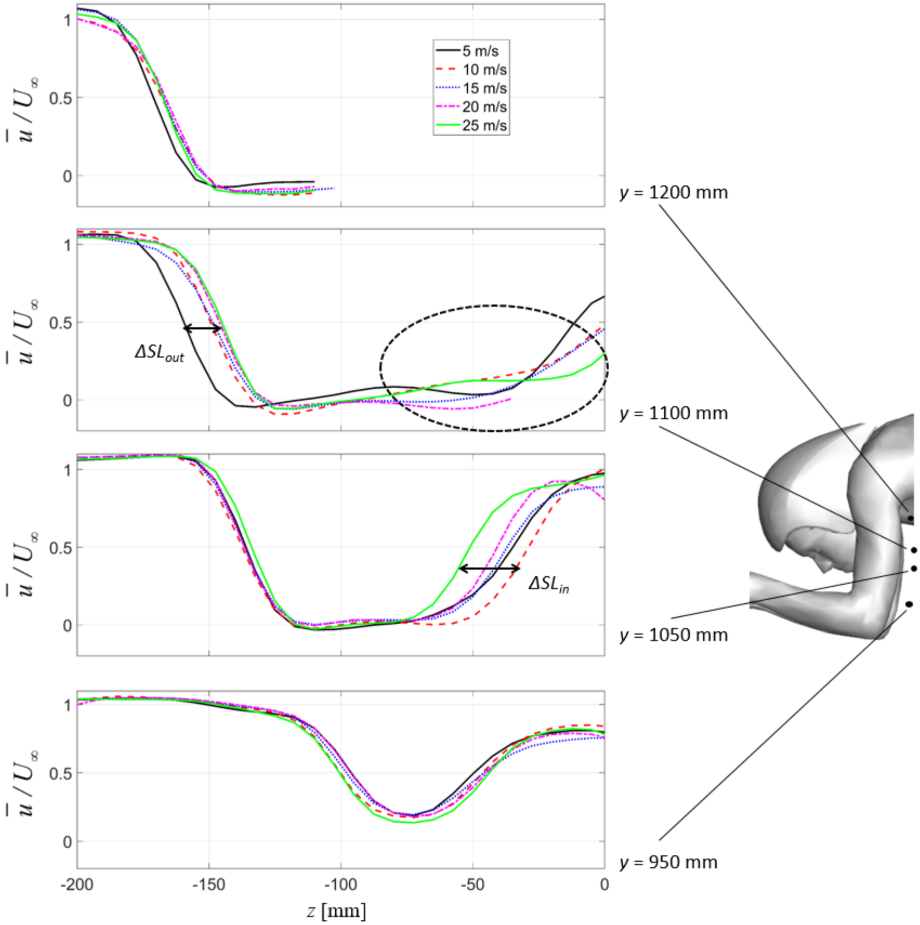

Figure 5.11: Spanwise profiles of non-dimensional time-average streamwise velocity in the near-wake of the upper arm.

freestream speeds, similarly to that of the lower leg. Hence, the critical velocity exceeds the maximum freestream velocity considered in this work.

The hip and lower back

In contrast to the arm and leg, the flow across the hip and lower back is strongly three dimensional and the width of its wake cannot be estimated in a similar way as for the previous cases. Hence, the discussion of the flow Reynolds number effects is presented more qualitatively. Figure 5.12 presents iso-surfaces of $\bar{u}/U_\infty = 0.2$ (first row), contours of non-dimensional streamwise velocity (second row), vertical velocity (third row) and non-dimensional streamwise vorticity (fourth row). Two branches of strong velocity deficit develop asymmetrically over the lower back (marked L and R in the top two rows of the first column of Figure 5.12) as a consequence of the asymmetric leg position. These branches stretch further

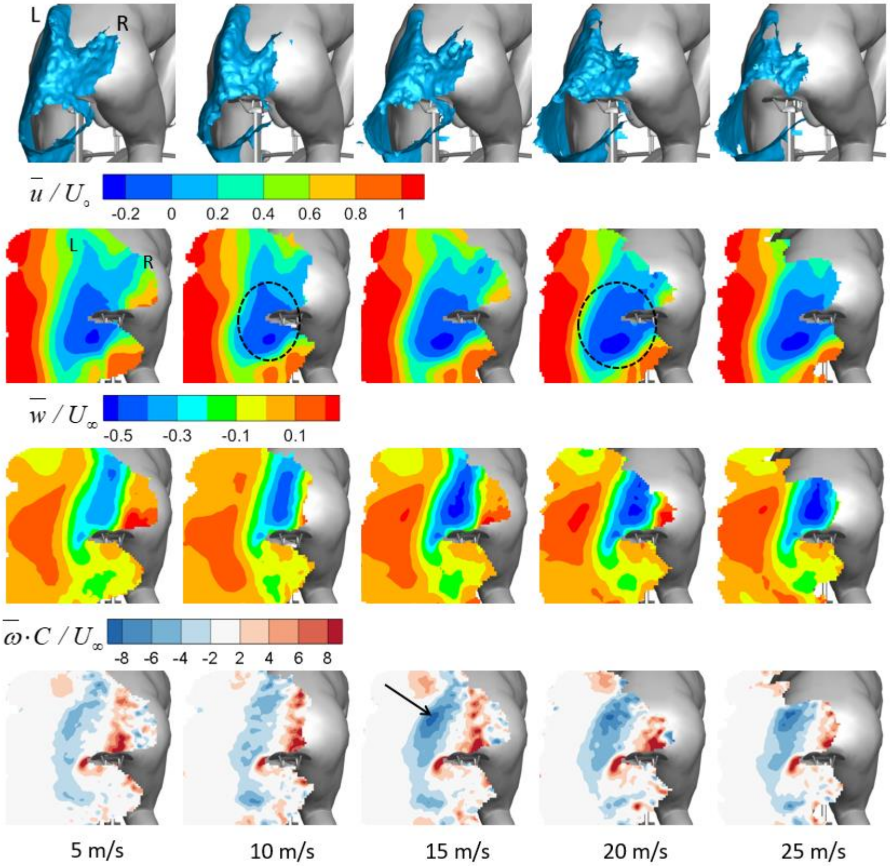

Figure 5.12: Iso-surfaces of 0.2 $\bar{u}/U_\infty$ (top), contours of non-dimensional streamwise velocity (second row), vertical velocity (third row) and streamwise vorticity (bottom) at x = 860 mm.

upstream at low freestream velocity (5 m/s $\leq U_\infty \leq$ 10 m/s) compared to the higher freestream speeds, suggesting a delayed flow separation in the latter conditions. As a consequence, the peak downwash over the lower back is increased from approximately $\bar{w}/U_\infty = -0.4$ to $\bar{w}/U_\infty = -0.55$ at 5 m/s $< U_\infty <$ 10 m/s and 15 m/s $< U_\infty <$ 25 m/s, respectively. Another consequence is an increase of the area of reverse flow behind the hip and lower back (indicated in Figure 5.12-second row). The delayed separation and increased downwash also introduce an increase of streamwise vorticity ($\bar{\omega}C/U_\infty$ increases from approximately -4.5 to -8.5) from the left thigh vortex (indicated in Figure 5.12-middle-bottom). Variations in the right thigh vortex cannot be observed, as it crosses the boundary of the measurement domain. It is concluded that the most significant change in flow topology in the present range of Reynolds numbers occurs between 10 m/s $< U_\infty <$ 15 m/s, as also observed for the upper leg flow.

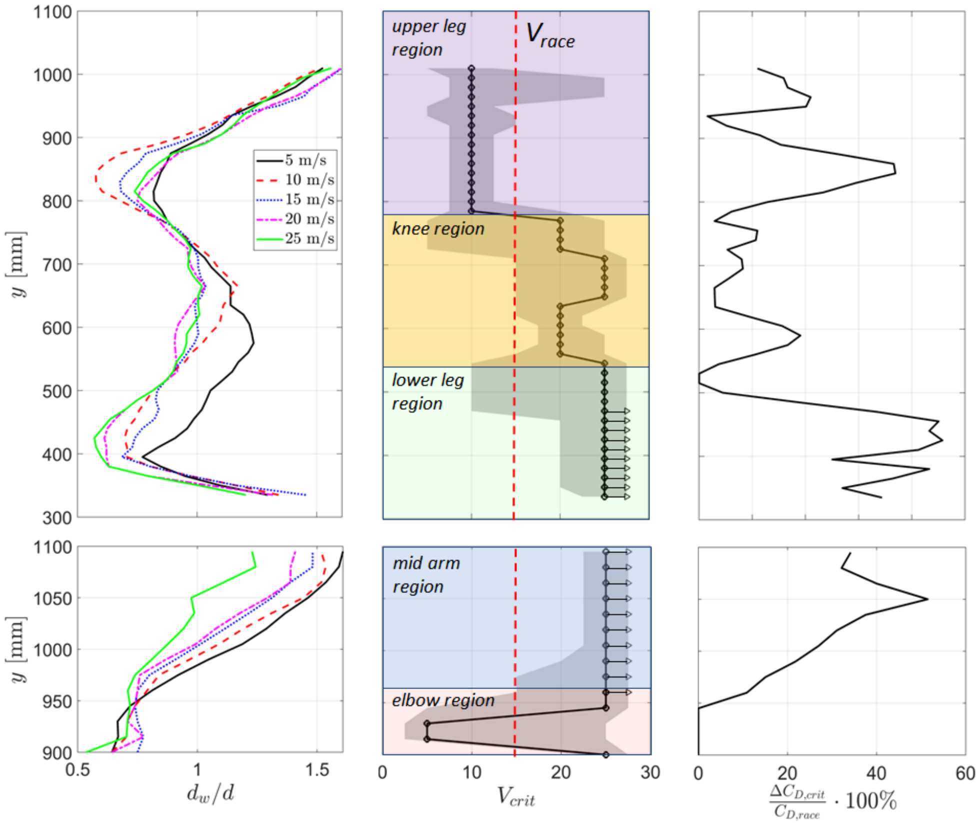

Figure 5.13: Wake width at increasing freestream velocity (left), critical velocity (middle) and relative drag coefficient reduction (right) along the leg (top) and the arm (bottom). The critical velocity uncertainty bandwidth is indicated by the shaded area and the red dashed line indicates typical race speed.

5.4.3 Wake width, critical velocity and drag reduction

The wake width is examined along the cyclist's arm and leg every 15 mm and at each value of the freestream velocity (Figure 5.13-left). It is observed that the spatial variation of the width along the leg is similar among the different speeds: minima of d/d_w are observed around y ~ 400 mm and y ~ 850 mm. This has been ascribed to the streamwise vortex pairs of the shank and upper leg, respectively. Furthermore, the large width at the top of the leg is the consequence of the merged left and right leg wakes. The critical velocity along the leg is depicted in Figure 5.13-middle and its uncertainty is indicated by the grey bandwidth. Three different regions can be distinguished: 1) the lower leg (320 mm < y < 500 mm), 2) the knee region (500 mm < y < 780 mm) and 3) the upper leg (780 mm < y < 1000 mm), which have been marked green, orange and purple (Figure 5.13-top middle), respectively. In the first region, the flow across the lower leg, the wake width decays rather monotonically over the full range of freestream velocity. Hence, the critical velocity is out of the present range of freestream velocity and exceeds 25 m/s, which is indicated by a right-pointing arrow symbol. In the knee region, the wake width exhibits a major reduction from U_∞ = 5 m/s to U_∞ = 15 m/s. At higher speeds it maintains approximately constant with a minor reduction between 15 m/s and 20 m/s. As a consequence, the critical velocity is estimated around 20 m/s, with an uncertainty typically exceeding 5 m/s. The boundaries of this region, where V_{crit} ~ 15 m/s, coincide with the location of the streamwise vortex pairs emanating from the shank and upper leg (see Figure 5.6) indicating that the flow Reynolds number effects of the leg are partly governed by these vortex structures. In both the lower leg and knee region, drag reductions may be achieved by tailored application of surface roughness considering a typical race speed V_{race} = 15 m/s. This is in contrast to the third region. Along the upper leg the wake width drops significantly between U_∞ = 5 m/s and U_∞ = 10 m/s, and then increases again for higher freestream velocities. Hence, the critical velocity is V_{crit} = 10 m/s and drag reduction may be achieved further polishing the leg's surface.

The upper arm may be divided into two different regions: The elbow (900 mm < y < 950 mm) and the mid-arm (950 mm < y < 1100 mm), marked red and blue, respectively in Figure 5.13-bottom-middle. The flow across the elbow does not exhibit typical drag crisis behaviour and, hence, no critical velocity exists. Conversely, in the mid-arm region the wake width drops significantly with increasing free-stream velocity. Similar to the lower leg, the critical condition is not reached in the present range of free-stream velocities. It is likely that the critical speed exceeds that of the lower leg considering the relatively large discrepancy between the wake width at 20 and 25 m/s in Figure 5.13-bottom left.

Finally, the reduction of the local drag coefficient with respect to race speeds, $\Delta C_{D,crit} / C_{D,race}$ is depicted in Figure 5.13-right, with $\Delta C_{D,crit} = C_{D,race} - C_{D,crit}$. In here $C_{D,race}$ is the drag coefficient at V_{race} = 15 m/s, while $C_{D,crit}$ is obtained through Equation 5.2. This relative drag coefficient reduction should be considered as a qualitative indication of the possible drag reduction among different regions on the cyclist body. It is observed that the most significant drag reductions are possible along the lower leg and the upper arm. A reduction of the critical velocity of the upper arm through application of surface roughness, however, may partly be balanced by an increase of the drag of the upper leg as a consequence of the reduced velocity deficit approaching it. In contrast to the lower leg and upper arm, the possible drag reduction is significantly smaller in the knee region as a consequence of critical velocity being closer to race speed.

5.5 Discussion

In the literature it has been hypothesized that the critical flow condition on leg models occurs at different speeds at different locations, because of its tapered geometry, and, hence, the drag crisis on the entire leg is not observed at one specific Reynolds number (e.g. Brownlie et al. 2009). Considering the results of the present work, that hypothesis is partly true. Indeed, starting from the ankle upwards, the critical velocity generally decays along the lower leg and knee region. In addition, however, other mechanisms affect the critical velocity and Reynolds number effects as well. The critical velocity on the cyclist limbs is governed locally by streamwise counter-rotating vortex pairs, such as the upper leg and shank vortices. Furthermore, wake interactions caused by the upstream arm, lead to Reynolds number effects opposite to those observed at isolated body parts. The Reynolds number effects in the regions that are not affected by these mechanisms are similar to those observed at isolated two-dimensional cylinders, depicting a significant decrease in wake width along the critical flow regime.

The authors realize that an experimental investigation such as that described in the present work is practically infeasible for most organisations that are responsible for the design of low-drag skinsuits, mostly because of the required PIV expertise and equipment. So instead of conducting these measurements for every new skinsuit, the present findings should serve as a reference and can be used in addition to the measurements that are conventionally conducted on isolated cylinders. Although the mannequin employed in the present investigation features specific anthropometric characteristics and is installed in a particular position, the model characteristics that affect the critical velocity can be considered typical features of a time-trial cyclist: legs with a thickness that increase from the ankle up, a knee junction between the upper and the lower leg and the upper arm being upstream of the upper leg. Hence, a general set of guidelines for the design of low-drag skinsuits can be distilled from this investigation. Based on the present finding the local aerodynamic drag along the cyclist’s lower leg, knee and upper arm can be reduced by application of surface roughness. To achieve the critical flow condition all along the limbs, the roughness on the upper arm and lower leg should be most pronounced, while in the knee region the roughness should be less articulated. In contrast, the aerodynamic drag of the upper leg may be reduced using extremely smooth fabrics. Note that the above recommendations to add surface roughness in the lower leg and knee region of the cyclist is currently in contradiction with cycling international regulations (uci.org). These regulations, however, describing on which parts of the legs a suit may be worn, may change in the future. Furthermore, the present findings may be used in sports such as speed skating, where such regulations are absent, and athlete position and speed is somehow similar to that in cycling.

6

THE RING-OF-FIRE SYSTEM: PRINCIPLES & PROOF-OF-CONCEPT

Preluding the application of the PIV wake rake on full-scale transiting cyclists, this chapter describes a proof-of-concept experiment that yields the aerodynamic drag of a sphere towed through stagnant air. Tomographic PIV measurements are conducted prior to and after passage of the model in the frame of reference of the laboratory. A Galilean transformation between coordinate systems, yields the velocity statistics in the frame of reference moving with the sphere. The aerodynamic drag is evaluated invoking the conservation of momentum within a control volume surrounding the model. The terms composing the drag are related to the flow momentum, the velocity fluctuations and the static pressure and are separately evaluated along the wake. The results show that the contribution of the pressure term vanishes after 5 sphere diameters. Hence, the PIV pressure evaluation can be omitted when evaluating the drag in the far wake, largely simplifying the wake rake procedures. Finally, the measurements are repeated at different towing speeds. The drag resolution of the PIV wake rake is estimated, assuming a constant drag coefficient within the Reynolds number range, to prospect the use of the technique in human-scale applications.

Part of the work presented in this chapter is published in:

Terra W, Sciacchitano A, Scarano F (2017), *Aerodynamic drag of a transiting sphere by large-scale tomographic-PIV*. Exp Fluids, 58:83

Terra W, Sciacchitano A, Scarano F, van Oudheusden BW (2018), *Drag resolution of a PIV wake rake for transiting models*. Exp Fluids, 59:120

6.1 Introduction

Aerodynamic drag measurement by PIV wake rakes can potentially be used to determine the aerodynamic drag of a cyclist in the field. This approach does not only allow for experiments practically impossible in a wind tunnel, it may also lead to a better understanding of the generation of the air resistance by relating the drag force to velocity distribution in the wake (e.g. Crouch et al. 2014). In this chapter, two experiments are documented, that serve as a proof-of-concept for the application of the PIV wake rake to cycling aerodynamics (the Ring-of-Fire system; Sciacchitano et al. 2015; Section 1.5). The goal of the first experiment is to measure the aerodynamic drag of towed sphere using tomographic PIV, by invoking the conservation of momentum in a control volume. Because micron-sized droplets limit PIV measurements to small measurement domains (Scarano 2013), helium-filled soap bubbles (HFSB) are considered essential for the current experiments (see Section 3.4). For the present demonstration, a sphere is towed within a rectangular channel at a velocity of 1.45 m/s (Re = 10,000). Despite the simple geometry, the flow exhibits an unsteady, turbulent wake with complex vortex interactions (e.g. Achenbach 1972; Brücker 2001), mimicking conditions also encountered behind some parts of the cyclist body. This first measurement campaign is referred to as the *single-velocity* experiment and the results are discussed in Sections 6.4.1 to 6.4.5.

The goal of the second experiment is to determine the drag resolution of the PIV wake rake by evaluating the air resistance of the sphere at different values of the towing velocity U_M = {1.08; 1.21; 1.34; 1.48; 1.62} m/s. The drag coefficient of a sphere exhibits a practically constant value over the flow regime 1000 < Re < 200,000 (Schlichting 1979). Hence, in the present range of conditions (6600 < Re < 11,400) the aerodynamic drag is expected to follow a quadratic increase with model speed. This property of the drag coefficient is exploited to estimate the accuracy of the drag from the PIV wake rake. Furthermore, the influence of non-quiescent flow conditions prior to the sphere passage is taken into account and discussed and the drag resolution of the PIV wake rake for transiting models is compared to that of other techniques to conclude on its applicability for full-scale field experiments. The results of such *multi-velocity* experiments are presented in Section 6.4.6.

6.2 Methodology

In contrast to typical wind tunnel conditions with a model at rest immersed into an air stream, in this work the model moves at constant speed, U_M^* through a fluid that is approximately quiescent ($u_{env}^* << U_M^*$) in the laboratory frame of reference, [x^*, y^*, z^*] (Figure 6.1-top; 2D representation for better readability). The instantaneous aerodynamic drag of a model in relative motion to a fluid can be expressed in the frame of reference moving with the object by invoking the conservation of momentum in a control volume, V (S being its boundary) surrounding it (Equation 3.6; Figure 6.1-bottom). After a Galilean transformation of the coordinates in the frame of reference moving with the model, $[\,x, y, z\,]$ to those in the laboratory frame of reference:

$$\begin{aligned} x^* &= x + U_M^* t \\ y^* &= y \\ z^* &= z \end{aligned} \qquad 6.1$$

The aerodynamic drag can be expressed in terms of the velocity measured in the laboratory frame of reference:

$$D(t) = \rho \iint\limits_{S_{meas}} \left(u_{env}^* - u_{wake}^*\right)\left(u_{wake}^* - U_M^*\right) dS + \iint\limits_{S_{meas}} \left(p_\infty - p\right) dS \qquad 6.2$$

In this equation $u*_{env}$ and $u*_{wake}$ are the streamwise velocity component of the fluid upstream and downstream of the model, respectively, and S_{meas} is the measurement plane, orthogonal to the motion of the object. The origin of the two coordinate systems coincides at $t = 0$ and, so, the velocity prior to and after passage of the model correspond to negative and positive t, respectively.

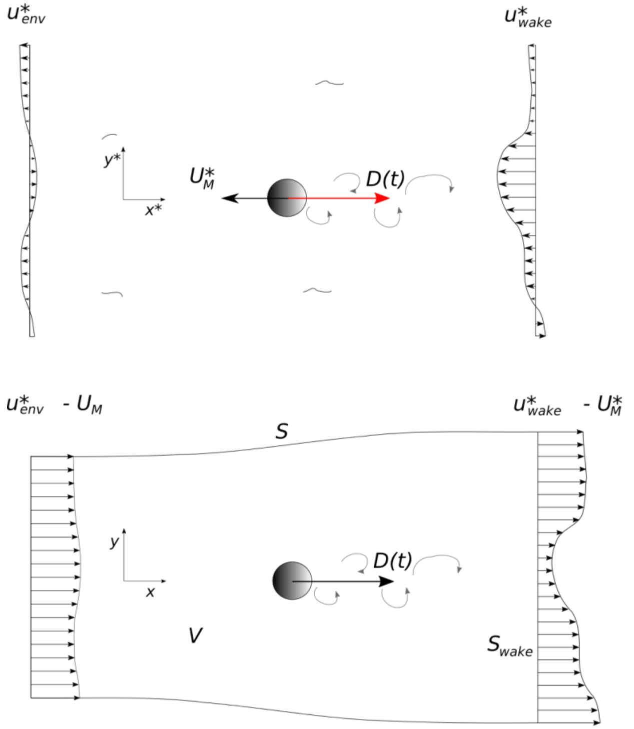

Figure 6.1: Fluid velocity relative to a transiting model in the laboratory frame of reference (top) and the frame of reference moving with the model.

Furthermore, note, that strictly speaking the present technique is not a PIV wake rake, as it requires the velocity upstream of the model in addition to that downstream of it. Only for perfectly quiescent air, $u^*_{env} = 0$, measurements upstream of the model can be omitted, which will be discussed in Section 6.4.6.

As a consequence of a fixed measurement area in the laboratory frame of reference in combination with a transiting model, the wake velocity field is acquired, after passage of the model, at increasing distance to the model. For each single transit, the drag of the model $\overline{D}_{single}$ can be computed as an average drag obtained from the collection of the acquired wake velocity fields after application of Equation 6.2. Consecutively, a multi-passage average drag $\overline{D}_{multi}$ can be computed from the ensemble $\overline{D}_{single}$ obtained from repeated measurements conducted at the same model speed.

Alternatively, $\overline{D}_{multi}$ can be obtained using the statistics of the obtained velocity fields. The measured fluid velocity and the model velocity are decomposed into an average and a fluctuating part:

$$\begin{aligned} u &= \overline{u} + u' \\ U_M &= \overline{U}_M + U'_M \end{aligned} \tag{6.3}$$

Note that the subscript * referring to a velocity measured in the laboratory frame of reference has been omitted for better readability. After substitution of the above expressions in Equation 6.2 and averaging both sides of the equation, the multi-passage average drag is obtained from velocity and pressure statistics:

$$\begin{aligned} \overline{D}_{multi} = {} & \rho \iint\limits_{S_{meas}} \left(\overline{u}_{env} - \overline{u}_{wake}\right)\left(\overline{u}_{wake} - \overline{U}_M\right) dS - \rho \iint\limits_{S_{meas}} \overline{{u'_{wake}}^2}\, dS + \\ & \rho \iint\limits_{S_{meas}} \left(\overline{u'_{wake}\, u'_{env}} + \overline{u'_{wake}\, U'_M}\right) dS + \iint\limits_{S_{meas}} \left(p_\infty - \overline{p}\right) dS \end{aligned} \tag{6.4}$$

where $\overline{u'_{env}\, U'_M}$ is neglected assuming null correlation between the velocity of the environment and that of the model. The third right-hand-side term in Equation 6.4 can be neglected whenever the model speed is constant among repeated model passages and the fluctuations in the fluid prior to the model passage are weakly related to those after transit. This assumption results in:

$$\overline{D_{multi}} = \rho \iint\limits_{S_{wake}} \left(\overline{u_{env}} - \overline{u_{wake}}\right)\left(\overline{u_{wake}} - \overline{U_M}\right) dS - \rho \iint\limits_{S_{wake}} \overline{{u'_{wake}}^2}\, dS + \iint\limits_{S_{wake}} \left(p_\infty - \overline{p}\right) dS \tag{6.5}$$

The pressure term, appearing in Equations 6.2 and 6.5, is evaluated from the velocity statistics solving the Poisson equation for pressure as described in Section 3.5.4.

Finally, to estimate the drag accuracy of this PIV wake rake, repeated experiments are conducted varying the model velocity in a narrow range of Reynolds numbers, such that the multi-passage average drag coefficient, $\overline{C_{D,multi}}$ can be considered constant and independent of U_M. An ensemble average value of $\overline{C_{D,ens}}$ is then obtained from the multi-passage average drag coefficients with an accuracy, or drag resolution, ΔC_D expressed as:

$$\Delta C_D = \sqrt{\frac{1}{N_M - 1}\sum_{i=1}^{N_M}\left(\overline{C_{D\,multi,i}} - \overline{C_{D,ens}}\right)^2} \qquad 6.6$$

where N_M is the amount of different model speeds that are considered.

6.3 Experimental apparatus and measurement procedure

6.3.1 Measurement apparatus and conditions

A schematic view of the system is shown in Figure 6.2, with a photograph of the setup in Figure 6.3. The apparatus consists of a 170 cm long duct with a squared cross-section of 50×50 cm^2, where the sphere model is towed. Part of the duct has transparent walls for optical access. The origin of the laboratory frame of reference and that moving with the sphere are in the center of the measurement domain and that of the sphere, respectively.

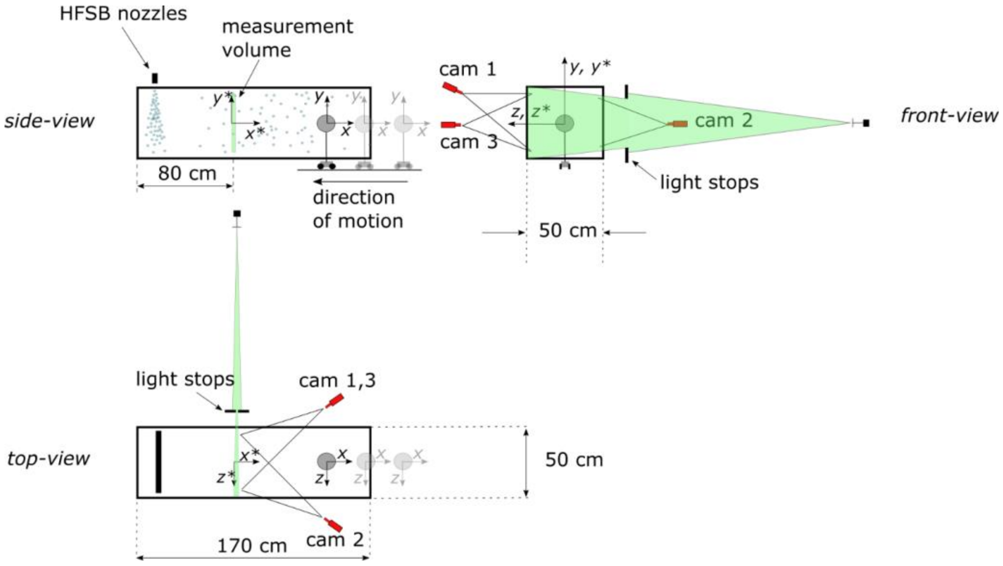

Figure 6.2: Schematic views of the experimental setup.

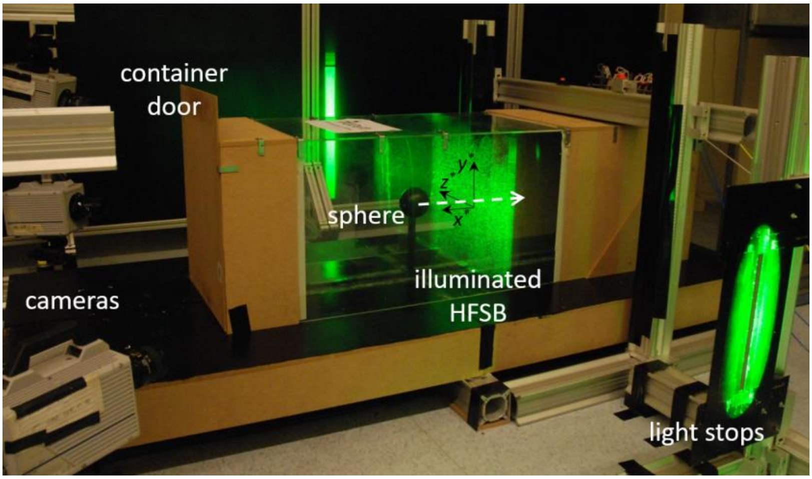

Figure 6.3: Overview of the experimental system and measurement configuration.

The model is a smooth sphere of diameter d = 10 cm towed at a constant speed U_M = 1.45 m/s along negative x-direction. The model is supported by an aerodynamically shaped strut with 20 mm chord and 3 mm thickness. The strut is 20 cm long and is installed onto a carriage moving on a rail beneath the bottom wall of the duct. The carriage is pulled by a linen wire connected to the shaft of a digitally controlled electric motor (Maxon Motor RE35). Five markers on the downstream surface of the sphere allow tracking its position during the transit.

The wake behind the sphere starting from rest needs time to reach a fully developed regime. For an impulsively started cylinder at low Reynolds number (Re < 100) it is reported that about 15 cylinder diameters (Coutanceau and Bouard 1977) are needed before the wake is developed. In the present work a conservative value is taken with the model starting from rest approximately 25 sphere diameters upstream of the measurement region.

6.3.2 Tomographic system

The time-resolved tomo-PIV measurements are conducted using neutrally buoyant helium-filled soap bubbles (HFSB, 300 μm diameter) as tracer particles produced with an array of ten generators that yield a total of about 300,000 particles per second. The air, helium and soap fluid flow rates are controlled by a fluid supply unit provided by LaVision GmbH. The average time response of such tracer particles is expected to be below 20 μs (Scarano et al. 2015). Considering the relevant flow time scale (d/U_M = 70 ms) the small value of the Stokes number of the tracers indicates their adequacy for the current experiments. PIV acquisition is performed within LaVision *Davis 8.3* and the PIV parameters, of the *single-velocity* and *multi-velocity* experiments, are listed in Table 6.1.

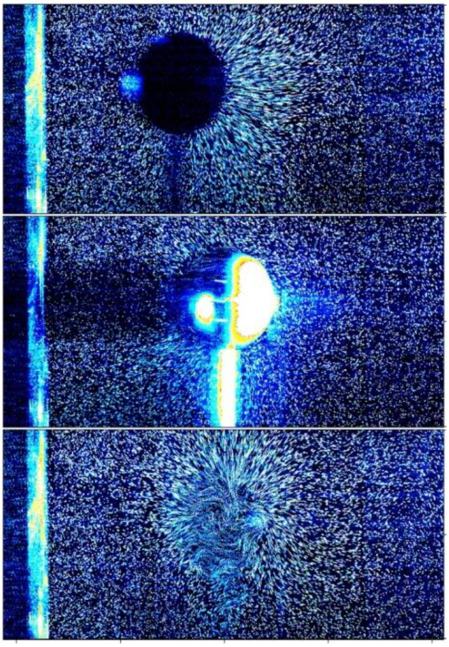

Figure 6.4: Particle streaks for three positions of the sphere passing through the measurement domain. The sphere positions are separated by time increments of 70 ms.

6.3.3 Measurement procedure

The tunnel entrance and exit are closed to confine the HFSB seeding before the transit of the sphere. The exit is closed by a porous curtain, which maintains the seeding tracers inside, but allows air flow associated to the sphere motion. The HFSB generators are operated for approximately two minutes until a steady-state concentration is reached. Approximately quiescent conditions are achieved 30 seconds after the generators are switched off. The tunnel entrance wall is then opened and the model is put in motion through the duct. Image recording begins one second before the sphere passes through the measurement region and stops when it touches the exit curtain. Figure 6.4 illustrates the air flow by particle streaks at three time instants; before entering (top), inside (middle) and after leaving the measurement domain (bottom). The measurements are separated by 70 ms (35 frames) and the streaklines are obtained by averaging ten consecutive frames. The highest velocity is observed in the center of the measurement region behind the model (bottom image) with quiescent air conditions at the edges. An animation of raw images of the passing sphere is available online (Terra et al. 2017; electronic supplementary material). The experiment comprises 35 repeated measurements to form a statistical estimate of the flow properties and the associated aerodynamic drag.

Table 6.1: Main experimental parameters and procedures of the *single-velocity* and *multi-velocity* experiments

Experimental apparatus and procedure

	Single-velocity	***Multi-velocity***
Duct dimensions [m^3]	2 × 0.5 × 0.5 [x, y, z]	2 × 0.75 × 0.5 [x, y, z]
Determination of model speed	Estimated by marker tracking using the images acquired for PIV	Edge detection using a fourth Photron Fast Cam SA1 with a line of sight orthogonal to the motion of the sphere
Model speed [m/s]	1.45 (assumed constant among passages)	1.08; 1.21; 1.34; 1.48; 1.62 (Measured each individual passage)
Number of model transits (per model speed)	35	20 - 60

PIV Equipment

Purpose	**Instrument**	***Single-velocity***	***Multi-velocity***
Imaging	cameras	Photron Fast Cam SA1 cameras (CMOS, 1024×1024 pixels, pixel pitch of 20 µm, 12 Bits)	Photron Fast Cam SA1 cameras (CMOS, 1024×1024 pixels, pixel pitch of 20 µm, 12 Bits)
	objectives	4 × Nikkor 60 mm	Nikkor 35, 50, 60 and 60 mm (camera 1, 2, 3 and 4, respectively)
Illumination	Laser	Quantronix *Darwin Duo* Nd:YLF laser (2 × 25 mJ/pulse at 1 kHz)	Quantronix *Darwin Duo* Nd:YLF laser (2 × 25 mJ/pulse at 1 kHz)
Seeding	Tracer particles	HFSB	HFSB
	Seeding system	10-nozzle array	10-nozzle array

PIV imaging and acquisition

Purpose	**Parameter**	***Single-velocity***	***Multi-velocity***
Imaging	Field of view [m^3]	0.03 × 0.4 × 0.4 [x, y, z]	0.03 × 0.4 × 0.4 [x, y, z]
	$f_\#$	8	8
	Magnification	0.07	0.07
Measurement rate	f_{acq} [Hz]	500	500
Seeding concentration	Particle image density [particles/px]	0.04	0.04
	Seeding density [particles/cm^3]	3	3

PIV processing parameters

Purpose	**Parameter**	***Single-velocity***	***Multi-velocity***
	Volume reconstruction and velocity evaluation	Sequential Motion Tracking Enhancement (SMTE) algorithm	Sequential Motion Tracking Enhancement (SMTE) algorithm
	Interrogation volumes [vox]	32^3	96^3 Note: volumes have been increased w.r.t. the single-velocity experiment to reduce the correlation between adjacent vectors
	Overlap	75%	75%
	Vector pitch [vectors/cm]	3	1

6.3.4 Data reduction

The tomographic-PIV data analysis is performed with the LaVision *Davis 8.3* software. Image pre-processing comprises background subtraction and Gaussian smoothing. The volume reconstruction and velocity evaluation follows the sequential MTE-MART algorithm (SMTE, Lynch and Scarano 2015), yielding a discretized object with 1074×1050×72 voxels. The interrogation is based on spatial cross-correlation volumes of 32^3 voxels with an overlap of 75%. The resulting velocity vector field has a density of 3 vectors/cm. Figure 6.5 illustrates the reconstructed intensity distribution along the depth. The SMTE algorithm returns a high reconstruction signal-to-noise ratio, indicating that the cross correlation result is not affected by ghost particles effects (Elsinga et al. 2006).

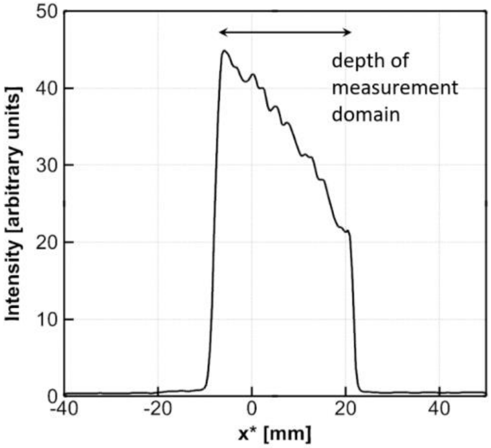

Figure 6.5: Intensity distribution of tomographic reconstruction along the measurement depth (evaluated over an area of 25×25 cm^2).

The time-average velocity and its fluctuations is obtained in the laboratory frame of reference from the repeated model transits. A three-dimensional spatial representation of the velocity field in the sphere frame of reference is obtained after a Galilean transformation of the latter (Equation 6.1). An illustration is given in Figure 6.6 encompassing the streamwise range between 0.5 < *x/d* < 9.5.

The Poisson equation for pressure is solved prescribing Neumann conditions on all boundaries. A uniform pressure distribution is added afterwards to the latter, such that the pressure along the top, bottom and side boundaries, in the spatial range in which the velocity at these boundaries best matches stagnant conditions (*x*/*d* > 4), matches that of the freestream. A small segment (5 cm wide) in the center of the bottom boundary, which is affected by the wake of the strut, is excluded from the boundary condition.

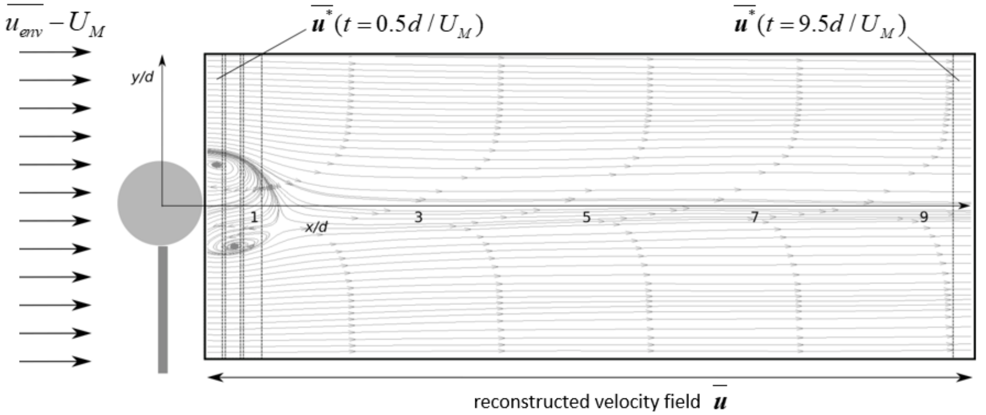

Figure 6.6: Illustration of the time-average streamlines of the velocity in the sphere frame of reference ($\overline{\boldsymbol{u}}$) after a Galilean transformation of the velocity statistics in the laboratory frame of reference ($\overline{\boldsymbol{u}}^*$).

6.4 Results

6.4.1 Instantaneous flow field

At a Reynolds number of 10,000 the flow around a sphere is in the sub-critical regime exhibiting an unsteady and turbulent wake. A snapshot of the flow structure will typically yield an asymmetric pattern, while the time-average structure is known to be axi-symmetric. Figure 6.7 shows the instantaneous velocity field in the laboratory frame of reference in the center *yz*-plane at four consecutive time instants. A supplementary animation of the time-resolved velocity field is available online (Terra et al. 2017; electronic supplementary material). Non-dimensional time is defined as $T = tU_M^* / d$. A unit time increment $\Delta T = 1$ corresponds to the sphere advancing one diameter. At $T = 0.5$, a region of accelerated flow is visible at the periphery of the wake. Furthermore, a peak of negative streamwise velocity is present in the near wake of the sphere. The maximum velocity deficit decays with time, consistently with the observations from past investigations (Jang and Lee 2008; Constantinescu and Squires 2003).

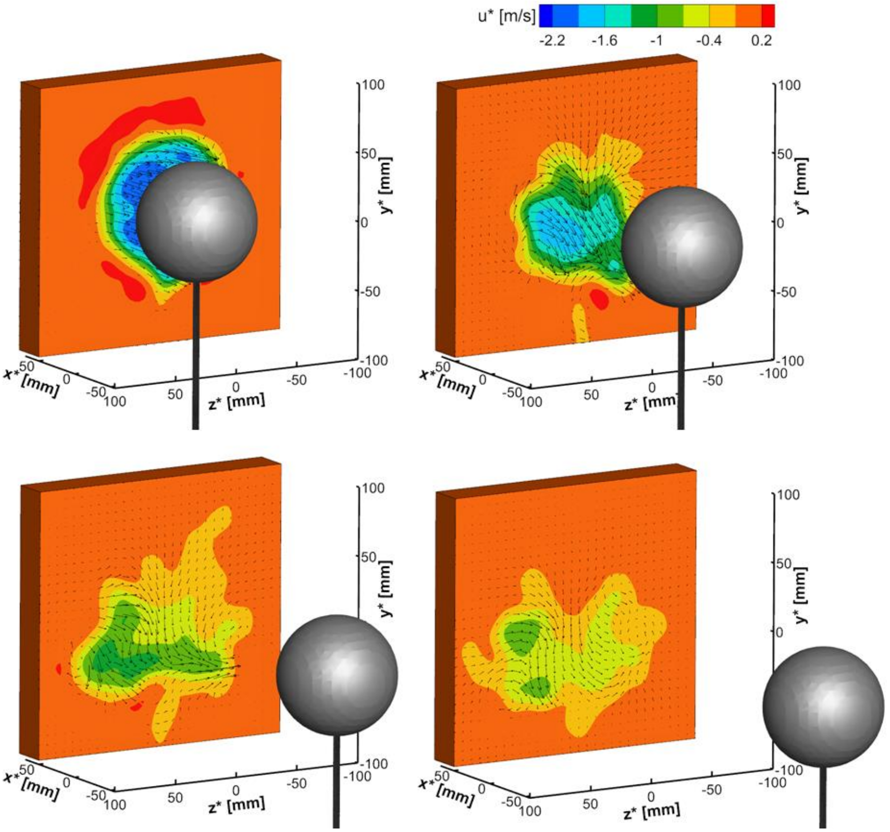

Figure 6.7: Instantaneous streamwise velocity u^* in the y^*z^*-plane at four time instants, $T = 0.5$, $T = 1.5$, $T = 2.5$ and $T = = 3.5$. The measurement region is cropped to half its size along y and z for readability.

6.4.2 Time-average flow structure

The ensemble-statistics yield the time-average velocity field, the fluctuating velocity and time-average pressure distribution. These terms are inspected to understand how the individual terms from Equation 6.5 contribute to the aerodynamic drag. Figure 6.8 illustrates the streamwise velocity distribution in the separated wake ($x/d = 0.85$, top) and after the flow reattachment ($x/d = 3$, bottom). The velocity field in the wake is close to the axi-symmetric condition, with some slight deviations due to the supporting strut, which causes a region of approximately 5% velocity deficit. The latter will be accounted for in the section on drag derivation. Furthermore, the spatial velocity distribution shows a radial velocity directed towards the flow symmetry axis, decreasing in magnitude at increasing distance from the sphere, which is also consistent with literature (e.g. Jang and Lee 2008; see also Section 2.1.2). The expected flow reversal in the center of the wake is also captured in the present measurement (Figure 6.8-top-right). The streamwise velocity contour at $x/d = 3$ (Figure 6.8-bottom-right) shows a pronounced asymmetry in the spatial velocity distribution outside the wake. At the top of the domain the

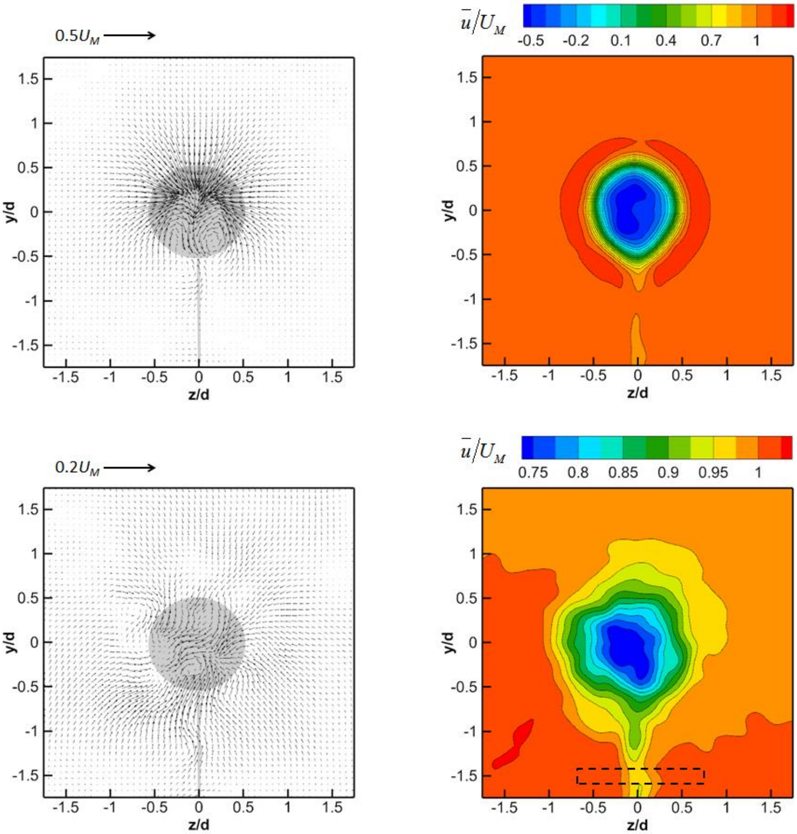

Figure 6.8: Time-average velocity vectors in the wake of the sphere at $x/d = 0.85$ (top-left) and $x/d = 3$ (bottom-left). Streamwise velocity contours (right). A rectangle (bottom-right) indicates the region where the strut drag is estimated.

non-dimensional streamwise velocity is about 0.98, while at its bottom it is 1.01. This asymmetry stems from the flow conditions prior to the transit of the sphere and is ascribed to the motion induced during injection of the HFSB tracers. In the derivation of the aerodynamic drag, the momentum term expresses a deficit in the wake, relative to the fluid momentum prior to the passage of the sphere (Equation 6.2). Therefore any residual motion before the passage of the sphere is accounted for in the drag evaluation. Furthermore, Appendix C is dedicated to characterization of the fluid motion prior to the model passage in relation to the wake velocity and model speed.

The streamwise velocity distribution in the central *xy*-plane is depicted in Figure 6.9 in the spatial range $0.5 < x/d < 3.5$. The streamlines pattern yields a reattachment point at about $x/d = 1.3$, which is consistent with values from literature. Table 2.1 summarizes, among other, the relevant flow properties from other works: Jang and Lee (2008) report a recirculation length, $L/d = 1.05$ ($Re = 11{,}000$) obtained by PIV; Ozgoren et al. (2011) measure a value of about 1.4

(*Re* = 10,000) by PIV; Bakić et al. (2006) list a value of 1.5 (*Re* = 51,500) measured by LDV; the numerical work of Yun et al. (2006) and Constantinescu and Squires (2003), both at *Re* = 10,000, report a significantly longer separated wake with *L*/*d* = 1.86 and 2.2, respectively. The variability of the reattachment position can be ascribed to experimental settings, the model support (Bakić et al. 2006 use a single rigid support from the back of the sphere; Ozgoren et al. 2011 apply a strut from the top and Jang and Lee suspend the sphere with two thin wires forming an X-shape through the center of the sphere) as well as to the settings of the numerical simulations (i.e. the grid resolution and subgrid-scale modeling for the LES).

The maximum reverse flow velocity measured here is -0.52 occurring at *x*/*d* = 0.85 approximately on the symmetry axis (Figure 6.9-top), which compares fairly well to the value of -0.4 reported by Constantinescu and Squires (2003) and -0.427 of Bakić et al. (2006). The location of maximum reverse flow, differs from that reported by Constantinescu and Squires (2003) (*x*/*d* = 1.41), presumably due to the larger recirculation length.

Asymmetries in the mean flow are observed in both the vertical plane (Figure 6.9-left) and the horizontal plane (Figure 6.9-right). These may stem from a number of causes: primarily non-homogeneous flow prior to the passage of the model, but also incomplete statistical convergence and the presence of the strut.

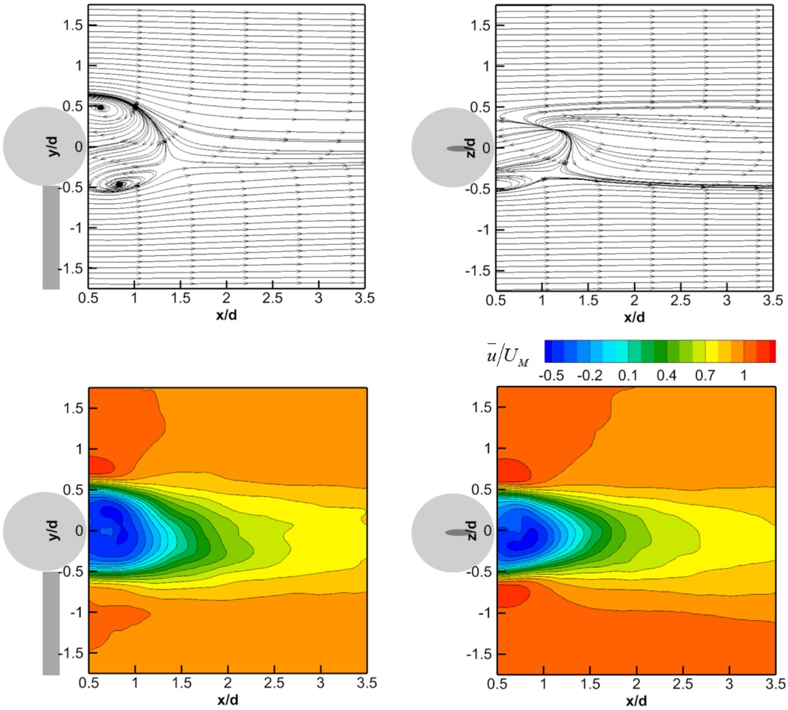

Figure 6.9: Spatial distribution of the time-average velocity in the wake of the sphere in the center *xy*-plane (left) and the center *xz*-plane (right). Flow streamlines (top) and contours of streamwise velocity (bottom). The measurement region is cropped along *x* for readability.

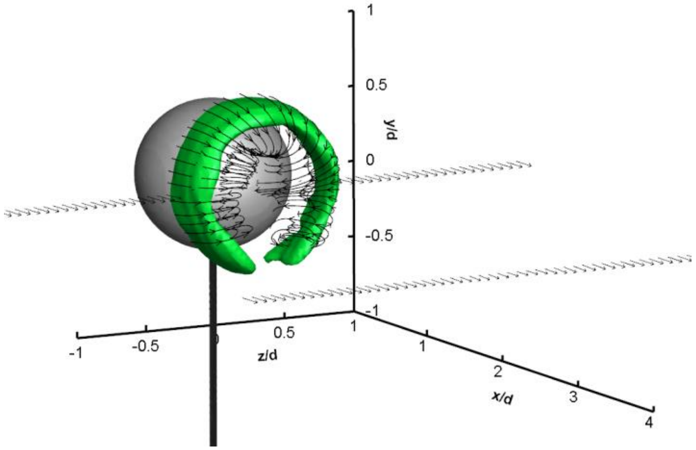

Figure 6.10: Streamlines of time-average velocity in the recirculation region in the wake of the sphere. Iso-surface of vorticity magnitude at 6.7 rad/s (green). Velocity vectors are depicted at x/d = 0.5 and x/d = 3.5 in the at y/d = 0.

The toroidal structure of the recirculating flow when examined in the *xy*-cross-section yields two foci at about x/d = 0.75 and radial distance r/d = 0.45, (Figure 6.9-top-left), which closely correspond with the flow topology reported by Ozgoren et al. (2011). The presence of this vortex structure is less evident in the horizontal center-plane (Figure 6.9-top-right), which is attributed to the limited size of the statistical ensemble. The recirculation region past a sphere is axis-symmetric (e.g. Jang and Lee 2008). Figure 6.10 illustrates that the vorticity magnitude iso-surface (value selected at 6.7 rad/s) features such an axi-symmetric flow structure with the annular shape shortly interrupted at the position of the supporting strut.

Table 6.2: Time-average velocity uncertainty as a percentage of the sphere velocity along the wake.

Position		Max uncertainty time-average velocity as percentage of U_M	
Region	x/d	$\bar{u}$	$\bar{v}, \bar{w}$
Wake center	1	6.5	5.5
	3	3.5	3
	7	1.5	1
Outer region	1 to 7	0.3	0.3

The uncertainty of the time-average velocity, ε_v primarily stems from the uncertainty of the measurement of the instantaneous velocity and the size of the ensemble used to estimate the time-average value. Its value decreases with the square root of the number of uncorrelated samples (N = 35 here): $\varepsilon_v = \sigma / \sqrt{N}$, where σ is the standard deviation of the velocity from the ensemble at the same phase. In the region outside the wake, velocity fluctuations are the smallest, and the standard uncertainty is about 0.3% of the sphere velocity. Inside the wake, the uncertainty attains a maximum level of 6.5% of the sphere velocity (as a result of the velocity fluctuations) at the shear layer locations at x/d = 1. The uncertainty of the mean velocity decreases with the distance from the model as a result of turbulence decay. At x/d = 3 the maximum uncertainty is 3.5% and at x/d = 7 it stays within 1.5%. An overview of the uncertainties of the three velocity components is given in Table 6.2.

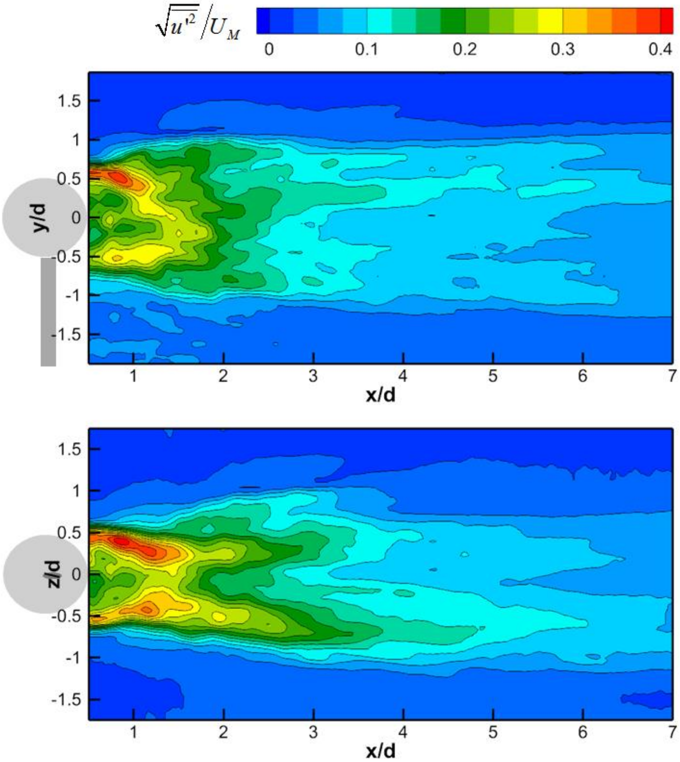

Figure 6.11: Spatial distribution of streamwise velocity fluctuations in the center xy-plane (top) and the center xz-plane (bottom).

6.4.3 Velocity fluctuations

The distribution of turbulent fluctuations plays a role in the momentum exchange within the wake and needs to be accounted for when evaluating the aerodynamic drag. Figure 6.11 shows the contour plots of the root-mean-square of the streamwise velocity fluctuations in the center xy-plane (top) and the center xz-plane (bottom). The velocity fluctuations are rather symmetric in both planes. Their distribution in the xz-plane compares well to literature data (Jang and Lee 2008; Constantinescu and Squires 2003; Yun et al. 2006), with maxima around $x/d = 1$ and $z/d = \pm 0.45$, featuring two branches with peak values that diverge from the streamwise axis and decreasing in strength for $x/d > 1$. The distribution in the xy-plane shows less similarity to literature, likely due to the disturbance of the supporting strut. The local maxima of $\sqrt{\overline{u'^2}}/U_M$ are between 0.35 and 0.4, within the range reported in literature (Table 2.1). At $x/d = 7$, the fluctuations have not decayed yet and exhibit a maximum of about 0.08, indicating that the Reynolds stress term in Equation 6.4 still contributes to the drag of the sphere at that distance.

6.4.4 Pressure distribution

The flow past a bluff body generally produces a large base drag resulting from a low-pressure region at the base of the object (Section 2.1.2). After reattachment the pressure recovers towards the free-stream conditions. This variation of the pressure field is investigated to understand its contribution to the aerodynamic drag. Figure 6.12 depicts the distribution of the mean pressure coefficient in the center *xy*-plane (top) and the center *xz*-plane (bottom). The spatial distribution of the time-average pressure coefficient features a minimum approximately corresponding with the focus of the toroidal recirculation (Figure 6.9-bottom-left). At the reattachment point, a region of positive C_P is observed. The distribution of pressure shows a slight asymmetry in both planes, but to a lesser extent compared to the velocity fields presented in Figure 6.9 and Figure 6.11. The general wake pressure topology corresponds relatively well to that obtained by Jux et al. (2019), although the annular pressure minimum of the present work (C_p ~ -0.7) is comparatively higher than that of the latter work (C_p ~ -0.5). The

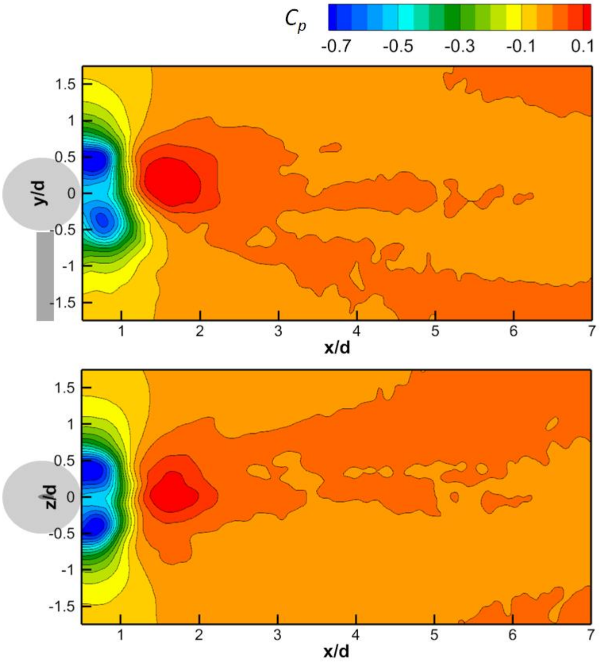

Figure 6.12: Spatial distribution of time-average pressure coefficient in the center *xy*-plane (top) and the *xz*-plane (bottom).

base pressure coefficient estimated from the flow field pressure close to the solid surface is about -0.52 in the present experiment, which is also comparatively higher than what is reported by Yun et al. (2006) and Constantinescu and Squires (2003) who report a value of -0.27 and Bakić et al. (2006) with a value of -0.3 at $Re = 51{,}500$. Nevertheless, in the current work, the drag is evaluated up to the far wake, where the pressure practically equals that of the quiescent flow and where the pressure term is deemed negligible ($|C_p| < 0.004$ at $x/d = 7$).

6.4.5 Aerodynamic drag evaluation

Both the model and its strut contribute to the drag. The two contributions need to be separated to obtain solely the sphere drag. The effect of the strut on the flow is visible in Figure 6.8-right. Its drag introduces a bias error for the estimation of the sphere drag. This error can be estimated by a local application of the control volume approach, which considers a region only affected by the strut. The control volume, containing a 2 cm section of the strut ($-0.75 < z/d < 0.75$ and $-1.4 < y/d < -1.6$), is indicated by the dashed line in Figure 6.8-right-bottom. The contribution is evaluated at a distance of 100 strut widths downstream of the model, where the pressure and Reynolds stress terms on the drag can be neglected. Afterwards, the drag of the entire strut is obtained, scaling the drag of the 2 cm section to its full length. The resulting strut drag is 0.6 mN, which is subtracted from the drag of the entire model (5.6 mN).

A second source of bias error for the drag is the finite size of the rectangular channel. Considering a blockage factor of 3.4%, the value of the drag in the experiment overestimates that of a sphere travelling in an unconfined medium (Moradian et al. 2009). The drag is therefore corrected, using the continuity equation (assuming continuous solid blockage), multiplying the measured value by a factor 0.94. The results presented in the remainder of the work refer solely to the drag of the sphere and include the correction for blockage (0.3 mN).

The time-average aerodynamic drag, derived from the velocity statistics, is expected to be independent of the distance between the measurement plane and the sphere. Given the principle stated in Equation 6.5 the sum of the three terms on the right hand side is an invariant when considering steady state conditions (assumed after ensemble averaging over several passages). At sufficient distance from the object, the drag is expected to be dominated solely by the momentum deficit term, as the pressure disturbance and the velocity fluctuations terms decay. Figure 6.13 shows the drag coefficient computed in the wake of the model in a streamwise range between $x/d = 0.5$ and $x/d = 9.5$. The physical location at which the drag is computed hardly affects the resulting drag coefficient value until $x/d = 7$, which confirms the solidity of the measurement principle. At $x/d = 7$, a sudden increase of the momentum contribution is observed, balanced by a negative increase of the pressure term. The latter situation is caused by the sphere hitting the porous curtain placed at the end of the channel. Given the amplitude of these effects, the measurement of the drag is not extended beyond 7 diameters, even though the drag coefficient itself appears to be affected to smaller extent.

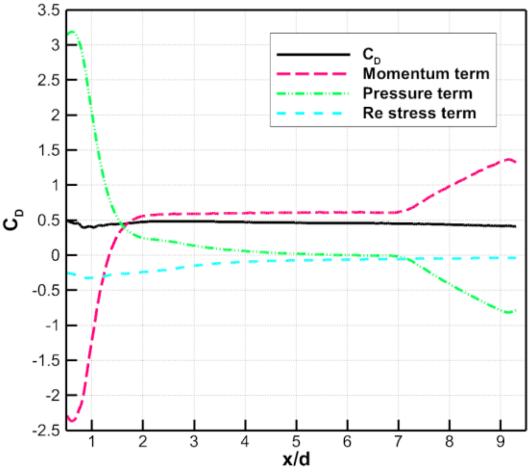

Figure 6.13: Mean drag coefficient and the individual momentum, pressure and Re stress terms evaluated at increasing distance from the sphere.

The momentum term is strongly negative close to the sphere, with a peak at *x*/*d* = 0.6, where it acts as a thrust term. Considering Equation 6.5, this thrust originates from the reverse flow in the recirculation region and partly from the accelerated flow around the sphere periphery. The contribution of the reverse flow to the thrust ends after reattachment (*x/d* = 1.3), where the momentum term changes sign and increases to reach a relatively constant value after *x/d* = 2. The negative contribution of the momentum deficit at small *x*/*d* is mostly compensated by the pressure term, which is highest within the first diameter close to the sphere and vanishes after about *x*/*d* = 5. The Reynolds normal stresses contribute negatively to the drag by definition. A minimum is observed around *x*/*d* = 1, which corresponds to the location of the peaks of streamwise velocity fluctuations in Figure 6.11. This term decays more slowly reaching a value of about -0.05 at *x*/*d* = 7. Along the wake the contribution of the Reynolds normal stress is significant and cannot be neglected when computing the aerodynamic drag.

The spatial development of the different terms, and in particular the pressure, has a practical consequence for the measurement of the aerodynamic drag. As long as the pressure term remains significant (*x*/*d* < 5), the full velocity gradient tensor evaluation is needed for accurate pressure reconstruction, requiring tomographic-PIV or other 3D-PIV techniques. Instead, when the pressure term is not significant, stereo-PIV measurements on a single plane may be sufficient for accurate drag evaluation.

The comparison against literature data is made taking into account the main sources of uncertainty. First, the position along the wake is considered. Although theoretically the drag may be measured at any arbitrary station in the wake, the large velocity fluctuations in the near wake increase the uncertainty of the measured time-average velocity (Table 6.2) and, therefore, the uncertainty of the pressure and the drag. The large variations observed for *x*/*d* < 2 suggest that reliable drag estimates should be obtained at a larger distance from the model. The computed drag coefficient is relatively constant with an average value of 0.47 for $x/d > 2$.

6.4.6 Sources of uncertainty and drag resolution

Note that in contrast to the results presented so far, the results addressed in the present section originate from the *multi-velocity* experiment, which consists of repeated *single-velocity* experiments at different model speeds within a Reynolds number range that allows the assumption of constant drag coefficient. Table 6.1 lists the main experimental parameters and procedures of the two experiments. In this case the instantaneous aerodynamic drag of individual passages is obtained through Equation 6.2.

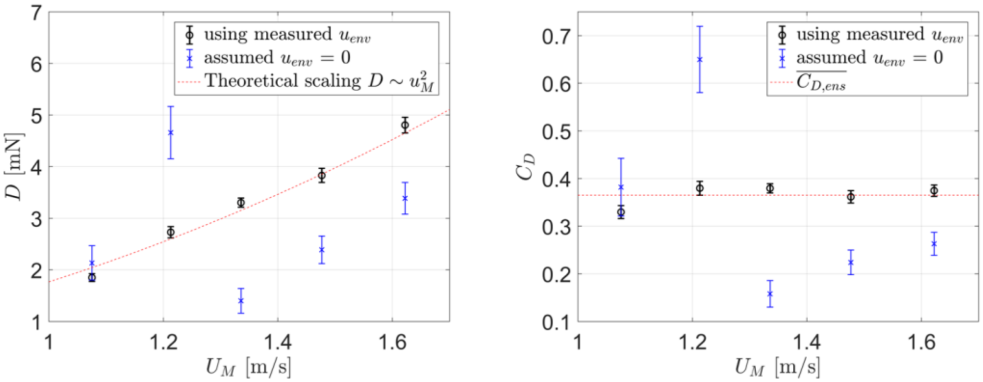

Figure 6.14**:** Multi-passage average drag $\overline{D}_{multi}$ (left) and drag coefficient $\overline{C_{D\,multi}}$ (right) at five different model velocities assuming $u^*_{env} = 0$ (blue symbols) and using the measured environment velocity u^*_{env} upstream of the model transit (black symbols). The red dashed lines represent a fit through the latter set of data points: $D = 0.00177U_M^2$ (left) and $C_D = 0.365$ (right).

First, the impact of the non-stagnant nature of the flow prior to the passage on the resulting drag force is evaluated. When the environment velocity is neglected (Figure 6.14-left, blue symbols), the expected quadratic increase in aerodynamic drag is not observed, resulting in an RMS error $\varepsilon_{RMS} = 1.5\,\text{mN}$ w.r.t. a quadratic fit of the five data points. Instead, accounting for the environment velocity yields values of the aerodynamic drag (Figure 6.14-left, black symbols) in good agreement with the theoretical quadratic scaling with the model velocity (red dashed line represents quadratic fit through the data points: $D = 0.00177U_M^2$) with an $\varepsilon_{RMS} = 0.16\,\text{mN}$. The uncertainty of the multi-passage average drag is computed at 95% confidence level, conservatively using one uncorrelated drag value per integer value of T. The uncertainty, depicted by the size of the error bars, is reduced from above 20% to below 7% of the mean drag value when accounting for the environmental velocity, hence increasing the precision of the wake rake approach. The uncertainty of the aerodynamic drag includes the drag variations stemming from the changing density and velocity of the model from run to run. In the computation of the drag coefficient these variations are accounted for and, hence, these sources of error do not contribute to the drag coefficient uncertainty (depicted in Figure 6.14-right). This explains why the relative uncertainty of the latter, is approximately 4% below that of the drag force.

For single model passages, variations of the drag coefficient up to 0.15 are observed (Figure 6.15). The latter are ascribed to the unsteady behavior of the wake, thus leading to a time-varying drag coefficient. Considering that the fluctuations of largest amplitude are observed over a time scale of approximately $T = 2$ (corresponding to a Strouhal number of 0.5), an observation time of the order of several periods would be required to achieve statistical convergence of the drag coefficient from a single passage. For each individual passage, the standard deviation of the (instantaneous) drag coefficient, C_D, is computed with respect to the time-average of the specific measurement, $\overline{C_D}_{single}$ (Figure 6.15-right). The ensemble average of these standard deviations is equal to $\sigma_{CD,single}$ = 0.026, exceeding the unsteady fluctuation of the C_D of a sphere reported in literature: Norman and McKeon (2011) measure $\sigma_{CD} \sim 0.02$ at Re = 50,000 and the numerical work of Constantinescu and Squires (2003) reports $\sigma_{CD} \sim 0.017$ at Re = 10,000. This over-prediction is largely attributed to the assumption of stationary flow prior to the model passage.

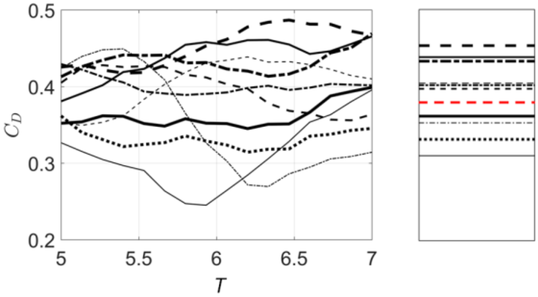

Figure 6.15: Temporal evolution of the measured drag coefficient from ten individual model passages (left) and its value averaged in the interval $5 < T < 7$. The ensemble average value is given in red (right).

Secondly, considerable variations of C_D are observed among different model passages, as can be seen from the comparison of the time-average drag coefficients from different runs (Figure 6.15-right). Such variations are mainly ascribed to the variability of the experimental conditions (mainly the environment velocity and its unsteady behaviour) among different runs. In particular, Equation 6.2 is valid under the assumption that the environment velocity field is stationary during the observation time ($-6 < T < 7$). The uncertainty associated with the variability of experimental conditions is quantified from the standard deviation of the average drag coefficients $\overline{C_D}_{single}$, and is equal to $2\sigma_{CD,multi}$ = 0.108. This uncertainty is considered as an upper-bound of the drag coefficient resolution of the single-passage PIV wake rake for transiting models. Decreasing this uncertainty value is likely possible taking into account longer measuring times (increasing the range of T). Considering that the average drag coefficient $\overline{C_{D\,multi}}$ is computed from N = 53 passages of the sphere, the uncertainty of the former at 95% confidence level is $2\sigma_{CD,multi}\Big/\sqrt{N}$ = 0.015.

Both the drag coefficient resolution of the single-passage measurement and the uncertainty of the multi-passage approach may be decreased firstly through better flow conditioning, thus reducing the temporal fluctuations of u_{env}, and secondly by decreasing the size of the wake plane by excluding the area that does not result from the interaction between the model and fluid. For example, the uncertainty of the multi-passage average drag coefficient decreases by 10%, when the integration area is reduced to [$-2 < y/d < 1.5$; $-1.5 < z/d < 1.5$] (illustrated by the dashed line, rectangular region in Figure C.1-top-right of Appendix C).

A third source of uncertainty may be introduced by possible systematic errors in the experiments, which can be evaluated from the drag coefficient obtained over repeated measurements at different model speed presented in Figure 6.14-right. As mentioned before, in this narrow range of Reynolds number the drag coefficient of the sphere is expected to be constant. Values of average drag coefficient between $0.33 < \overline{C_{D\,multi}} < 0.38$ are obtained, with an ensemble average drag coefficient of $\overline{C_{D,ens}}$ = 0.365 (red dashed line in Figure 6.14-right). When the drag resolution is computed considering the five model velocities (Equation 6.6; N_M = 5), the value ΔC_D = 0.021 or 21 drag counts is obtained (see also Table 6.3). When the drag coefficients are computed under the assumption of stagnant flow prior to the passage of the model (u_{env} = 0), the accuracy of the measurement is strongly reduced (see Figure 6.14 right) and the drag resolution is equal to ΔC_D = 0.193 (193 drag counts). This again clearly illustrates the necessity of measuring the flow prior to the passage to estimate the drag force accurately.

It is concluded that, with a drag resolution of about 20 drag counts, the PIV wake rake for transiting models remains a relatively course instrument compared to established techniques used in the laboratory environment (see Table 6.3 for a comparison). Instead, it is comparable to in-field approaches, such as the coast-down and torque measurement method. The additional contribution of the PIV wake rake is the introduction of fluid-dynamic information on the wake structure, of potential interest in the understanding of the flow physics and drag generation. It is expected that the current approach may be further perfected especially with control of environment conditions prior to the passage and possibly with more advanced modelling of the wake region.

Finally, regarding the applicability of the control volume approach to other bluff body flows, it is worth mentioning that the flow over spheres becomes turbulent at a Reynolds number around 800 and remains so afterwards. Hence, the statistical approach to determine the drag can be considered also for experiments at a higher Reynolds number. Therefore, the conclusions drawn from this study can be extrapolated to model geometries other than the sphere under the assumption of similarity in the behavior of the wake.

Table 6.3: Comparison between the drag resolution of the PIV wake rake of a transiting model to wind tunnel experiments and field test methods.

	Drag resolution [drag counts]
Stationary model in wind tunnel	
Force balance (Philipsen et al. 2004)	0.5
Pitot-tube wake rake (Brune 1994)	1
Transiting model	
PIV Wake rake (current study)	21
Coast-down method (Petrushov 1998)	12
Torque measurement (Bouillod et al. 2015)	10

7

CONCLUSIONS AND OUTLOOK

This research is divided into three research streams: Firstly, application of PIV wake rakes for cycling aerodynamic investigation; Secondly, a description of the cyclist Reynolds number effects and; Thirdly, a feasibility study to develop the Ring-of-Fire system for cyclist drag determination and quantitative flow visualization in the field. Each research stream involved large-scale PIV experiments that have been conducted using Helium-filled soap bubble tracers. The results revealed practical criteria for the use of PIV wake rakes in wind tunnels, as well as for its application in the field. The aerodynamic drag accuracy of these PIV wake rakes has been systematically determined to be able to comprehend their practical value. The flow topology and corresponding Reynolds number effects in the cyclist's near-wake have also been related to the aerodynamic drag. This led to a description of the drag crisis distribution along its limbs, yielding a reference for future low-drag skinsuit design.

Part of the work presented in this chapter is published in:

Spoelstra A, de Martino Norante L, **Terra W**, Sciacchitano A, Scarano F (2019) *On-site cycling drag analysis with the Ring of Fire*. Exp Fluids, 60:90

7.1 Conclusions

7.1.1 Wind tunnel cyclist PIV wake rakes

Two large-scale PIV wind tunnel experiments have been conducted in a thin volume of $5 \times 100 \times 160$ cm^3 in the wake of a full-scale cyclist model. The high light scattering capability of sub-millimeter helium-filled soap bubble tracers allows the measurement of the instantaneous velocity field in the full domain. The HFSB tracers are injected downstream of the wind tunnel turbulent meshes, resulting in a rather small cross-section of the seeded streamtube. As a consequence, the seeder dimensions play a critical role for the application of the PIV wake rake methods at the human scale.

In a first *partitioned-wake* experiment (PWE), cameras and laser imaged and illuminated, respectively, the entire measurement domain, while the in-house built HFSB seeder was traversed into 15 different positions to obtain flow tracers in the whole domain. Stitching of the velocity fields, resulting from each of these seeder positions, is avoided employing Lagrangian particle tracking. LPT allows to obtain the velocity statistics from the Lagrangian velocity ensemble and to obtain an accurate mean pressure solving the Poisson equation avoiding anomalies in the velocity gradients in the regions of overlap. Instead, in the second, *full-wake* experiments (FWE) campaign, a new and larger seeder, remained in a fixed position, seeding approximately the full cyclist wake, which allowed application of conventional stereo-PIV.

The distribution of the time-average streamwise velocity and vorticity compares well between the two experiments and also resembles literature closely. Differences, however, are observed as well. As a consequence of the relatively low seeding density and the resulting vector outliers, the level of velocity fluctuations obtained in FWE is relatively high in comparison to results of the PWE. This is particularly noticed at the edges of seeded streamtube, where the lack of seeding results in unphysical flow patterns of the time-average flow topology.

By invoking the conservation of momentum in a control volume containing the model, the time-average aerodynamic drag acting on the model is expressed as a summation of the three terms composing the overall resistive force, namely, the momentum, the Reynolds stress and the pressure term. Based on the results of the PWE, it is concluded that the contribution of the pressure term is negligible. Hence, the pressure reconstruction has been omitted in the FWE. More in general, the pressure reconstruction can be omitted for drag evaluation at a downstream distance of $x/L \geq 2.2$, where L is the hip width, which significantly simplifies data analysis. In contrast to the pressure term, the momentum term dominates the overall drag force, contributing to about 95% of the drag value.

The drag resolution of the PIV wake rake technique is estimated comparing the obtained aerodynamic drag to that of a force balance. The PWE were repeated at five freestream velocities, resulting in a measurement sensitivity of 30 drag counts or $\Delta C_D = 0.03$. This would qualify the large-scale PIV wake rake as a rather coarse instrument for drag determination. Instead, using the larger seeder, the drag resolution is reduced to 10 drag counts, after somehow similar repeated measurements. This suggests that traversing the seeder rake in order to seed the full cyclist wake, introduces a significant error into the measured velocity, which then propagates also into the obtained loads.

Finally, it is noted that after comparing measurements at a freestream speed of 4.5 m/s and 13 m/s, a significant wake narrowing and a corresponding drag coefficient reduction (approximately 15%) is observed in the latter condition. This may indicate a transition to turbulence in the boundary layer over the bluff elements of the cyclist body and consequently a delay in flow separation responsible for a local reduction of the drag coefficient. This assumption has been investigated in detail in Chapter 5 and the conclusions are summarized in the next section.

7.1.2 Cyclist Reynolds number effects and drag crisis distribution

The flow downstream of a cyclist mannequin's left arm, leg and hip is investigated using robotic volumetric particle image velocimetry at freestream velocities of [5 10 15 20 25] m/s. The near wake of these limbs features typical bluff body characteristics: two shear layers bounding a region of reverse flow. The width and length of the recirculation region increase with increasing body segment thickness. Moreover, this reverse flow area is governed by multiple streamwise counter-rotating vortex pairs that strongly reduce its size locally. The wake width of the lower leg and arm reduces with increasing freestream velocity. This variation is related to a variation in drag coefficient and exhibits the typical drag crisis behaviour as that encountered for isolated cylinders. In contrast, an increase in wake width is observed on the upper leg, which is attributed to the corresponding decrease of the upstream arm's wake width.

A distribution of the so-called critical velocity, the freestream speed at which the wake width is minimal, allows dividing the leg into different regions: 1) The lower leg region features a critical velocity that exceeds 25 m/s, the maximum of the present range of speeds; 2) The critical velocity in the knee region is approximately 20-25 m/s, and 3) The upper leg critical velocity equals 10 m/s. Similar to the lower leg, also along the upper arm the critical velocity exceeds 25 m/s.

Furthermore, it is concluded that critical flow condition is not only governed by the taper of the cyclist limbs. Instead, streamwise counter-rotating vortex pairs and limb wake interactions should also be considered in future cycling skinsuit design to achieve critical flow conditions along each body segment, and consequently have minimum aerodynamic drag at race speed. The author suggests that the present work serves as a reference for such design process. This would avoid repeating the present analysis for each newly to-be-designed skinsuit, which may be quite infeasible for most skinsuit designers.

7.1.3 Principles and Proof-of-Concept of the Ring-of-Fire system

In addition to applications in wind tunnels, cyclist PIV wake rakes may be used as well in the field through the Ring-of-Fire system. This concept is demonstrated in laboratory conditions by measuring the flow over a towed sphere with a diameter of 10 cm moving at 1.45 m/s. Time resolved PIV measurements are conducted during 35 model transits to obtain velocity statistics in the near- and far-wake of the model.

The time-average velocity and its fluctuations are used to estimate the flow field pressure. The aerodynamic drag is evaluated via a control volume approach, similar to the formulation used for wind tunnel PIV wake rakes. In contrast to the wind tunnel, where the incoming undisturbed flow can be assumed uniform, the environmental flow conditions prior to model passage are unknown. Hence, in order to evaluate the conservation of momentum across the model, the velocity prior to model passage needs to be measured in addition to the wake flow.

It is shown that the aerodynamic drag coefficient is practically unaffected by the position (distance into the wake) where the momentum integral is evaluated. In particular, the time-average drag coefficient obtained over two sphere diameters downstream of the model falls within the range of reported values in literature. For practical applications of the wake rake approach, it is observed that the pressure term vanishes after 5 sphere diameters, somehow similar to the observations of the cyclist wind tunnel PIV wake rake. Hence, drag estimation in the far-wake of the model allows omitting the pressure reconstruction, which can greatly simplify the measurement procedure. Furthermore, at such distance the aerodynamic drag is dominated by the momentum term and the Reynolds stress term contribution is below 10%. These findings correspond well to the human-scale wind tunnel PIV wake rake observations.

After repeating the measurements at five different model velocities in a narrow Reynolds number range, in which the drag coefficient is assumed constant, the drag accuracy of the PIV wake rake is assessed. It is concluded that when flow conditions are not fully quiescent, measurement of the spatial distribution of the flow velocity prior to the passage of the model is necessary for accurate drag estimations. In the present case the streamwise velocity upstream of the model generally remained below 2% of the model speed. Nevertheless, when not accounting for it in the momentum balance, the drag resolution deteriorates one order of magnitude. Instead, when the environmental conditions are normally accounted for, the PIV wake rake for transiting bluff bodies returns the average drag force and coefficient from multiple model passages with a drag resolution of the order of 20 drag counts ($\Delta C_D = 0.02$).

It is assumed that the major contribution of this drag uncertainty stems from the non-quiescient velocity prior to the model passage. As a consequence of the control volume application, any change in streamwise velocity between the velocity measurement upstream and downstream of the model, is felt as a force acting on the model. So the measured force can result from the fluid-model interaction and also from, for example, a sudden wind gust. The latter effect can be minimized, firstly, by cropping the integration surface to include only the fluid region downstream of the model that is affected by its passage. Secondly, reducing the time between the upstream and downstream measurement also reduces possible velocity variations that are not related to the actual aerodyamic drag acting on the model.

7.2 Outlook

7.2.1 Human-scale PIV wake rakes in wind tunnels

The human-size wind tunnel PIV wake rake returns the aerodynamic drag with an accuracy of approximately 10 drag counts. This can likely be reduced by the use of a tailored HFSB seeder. The seeding rake ideally is installed such that it is non-intrusive. However, the HFSB tracers will likely contaminate the turbulent meshes when injected upstream of these. Installing the seeder in the wind tunnel settling chamber downstream of these meshes resolves this problem. For a cyclist PIV wake rake application in a wind tunnel with a contraction ratio of 4, this would require a seeding rake of approximately 2 m (width) × 3 m (height). The seeder should also provide a sufficient seeding density in the entire measurement domain in order to avoid a too high level of PIV outliers.

7.2.2 Cyclist wake characterization

The control of HFSB seeding is especially relevant for further wake characterisation. The main streamwise vortices in the wake of the mannequin are unsteady in nature, suggesting that an analysis of the instantaneous wake topology may provide new insights for future drag reductions. Such wake characterisation is possible, for example, using proper orthogonal decomposition (POD) in order to identify the most energetic wake modes. A snapshot POD analysis (Sirovich 1987) has been performed using the instantaneous velocity fields obtained during the human-scale stereo PIV wake rake experiment (Chapter 4). Applied to velocity fields, this modal decomposition considers the input velocity fluctuations to rank the modes and, hence, the first modes are the most energetic (contain largest portion of kinetic energy). Figure 7.1 depicts the sum of the obtained velocity field time steady value and the first (left) and second POD mode (right). Note that the POD evaluation was performed at low freestream speed (5 m/s) and the domain has been cropped to achieve larger seeding density and avoid unseeded regions at the boundary, respectively.

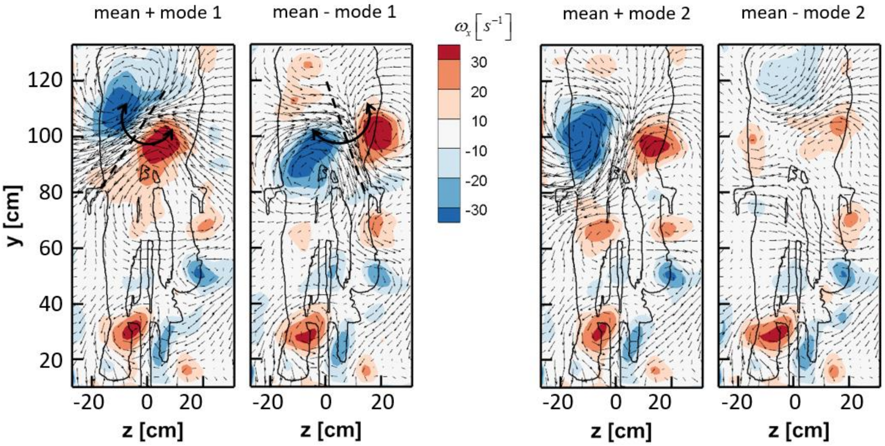

Figure 7.1: Cyclist wake first POD mode obtained at U_∞ = 5 m/s.

The first mode seems to involve a rotation along a streamwise axis of the primary wake vortex pair that evolves from the cyclist hip and thigh. The second mode, instead, seems to be associated with a growing and shrinking of vorticity magnitude of this primary vortex pair. As was to be expected from the present analysis, the first two modes are associated with the primary wake structure. Hence, the present analysis seems to provide further insight into a cyclist wake's unsteady behaviour. However, only a small amount of energy (approximately 5%) is contained in the present first two POD modes and the decay of energy with increasing order of the mode is slow. This is associated with the outliers in the instantaneous velocity fields used for the present analysis. Therefore, a deeper investigation has been omitted in this dissertation and the author recommends first to achieve a more robust and homogenous seeding distribution, in order to avoid these outliers. In the future this may allow, for example, investigations into the use of flow control methods to suppress the modes that are associated with high aerodynamic drag.

7.2.3 Reynolds number effects and low-drag skinsuit design

The use of passive flow control, through skinsuit surface roughness manipulation, has already been used successfully to reduce the aerodynamic drag of cyclists and other athletes, such as speed skaters. The present research provides new insights into further optimization of this approach and how different human limbs should be treated. An obvious limitation of the present investigation is the focus on the left side of the mannequin, the one with the leg extended. An investigation to the right side of the cyclist may confirm the assumptions of the authors that the Reynolds number effects in the wake of the flexed leg are much weaker as a consequence of 1) the more streamwise oriented upper and lower leg and 2) the larger knee angle and the corresponding increase of the strength of the counter rotating streamwise vortices emanating from the upper leg and shank (Jux et al. 2018). Furthermore, extending the present investigation to different crank angles would complement the understanding of the near-wake Reynolds number effects and the distribution of critical velocity. In addition, an investigation on a pedaling cyclist model may provide further insights. The pedaling motion induces additional streamwise and vertical velocity components to the leg and, hence, changes the orientation and magnitude of the leg's approach flow, thus likely affecting the critical velocity. For such a study, first the uncertainty of the present critical velocity estimation (2.5 m/s) should be reduced in order to measure the effect of these additional velocity components which remain generally below 2 m/s (crank length of 0.17 m and pedaling frequency of 1.7 Hz).

Apart from the above limitations of the experimental measurements, it should be noted that in practice a cyclist likely experiences conditions that are different from those seen during the present wind tunnel measurements. In particular the freestream turbulence may be different and the cyclist is at non-zero yaw angle as a consequence of cross-winds. It is well known that the former, the flow turbulence, affects the laminar to turbulent boundary layer transition, flow separation and, in turn, the critical Reynolds number. D'Auteuil et al. (2012) present the drag coefficient envelope of different skating mannequins in a *smooth* flow and a *turbulent* flow, mimicking the conditions in the field (Figure 7.2). Unfortunately, the turbulence characteristics of the two flow conditions are not published. Nevertheless, it is observed that the impact of the freestream turbulence on the model's drag coefficient is significant, which is attributed by the authors to a reduction of the critical velocity in the flow around the athlete's limbs with increasing turbulence. Hence, a description of the flow turbulence characterization of the athlete's race conditions in comparison to that of wind tunnels, and its effect on the aerodynamic drag, is deemed valuable for cycling aerodynamic community as well.

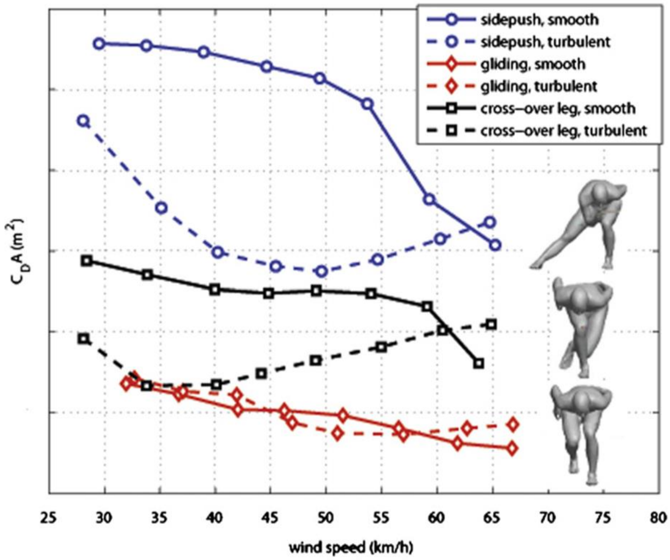

Figure 7.2: Drag coefficient at increasing velocity of three different skating mannequins in a smooth and a turbulent flow. The figure is adapted from D'Auteuil et al. (2012).

7.2.4 Cyclist aerodynamic drag analysis with the Ring-of-Fire

A first application

The findings from the conceptual studies on the transiting sphere, discussed in Chapter 6, are applied to assess the aerodynamic drag of a real cyclist by Spoelstra et al. (2019). The experimental apparatus adopted by Spoelstra et al. is largely similar to that described in Section 6.3.1. The experiments are conducted in a sport hall with an amateur cyclist riding repeatedly through a tunnel that is filled with HFSB (see Figure 7.3). The tracers are injected by a 4-wing-80-nozzle seeding system that is installed inside the tunnel, which was also used in the partitioned wake PIV wake rake experiment (Section 4.3.2). Low-repetition stereo-PIV is employed to obtain the velocity prior to, during and after the rider's transit in a 2 m × 2 m plane, orthogonal to the cyclist motion, in order to obtain the aerodynamic drag invoking the conservation of mass and momentum in a control volume moving with the model.

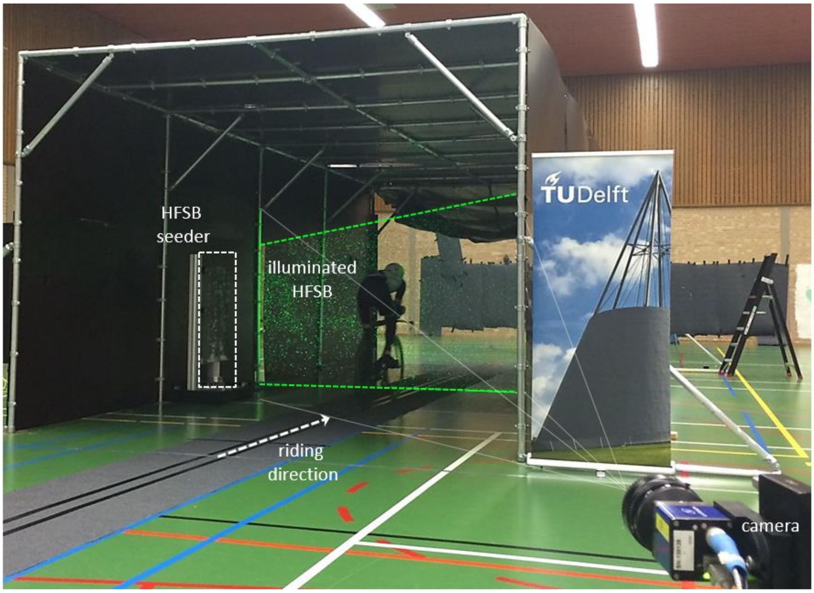

Figure 7.3: Experimental setup of an indoor Ring of Fire experiment (Figure adapted from Spoelstra et al. 2019).

In contrast to the experiments with the transiting sphere, phase-averaging of the instantaneous velocity fields in the wake of a pedaling cyclist requires accurate repeatability of the rider's crank angle upon crossing the measurement plane. This is especially relevant considering the significant variations in the wake topology and aerodynamic drag with changing position of the rider's legs along the crank cycle (see Section 2.3). The phase-average streamwise velocity at three wake stations is depicted in Figure 7.4. The silhouette that is depicted in the Figure to the left does not represent the rider's actual geometry. It only serves for better readability of the results and to indicate the cyclist leg position. At closest distance to the rider (x/c = 3 where c = 0.600 m) a distinct region of high velocity deficit behind the riders legs is observed, similar to the observations obtained with the cyclist wind tunnel PIV wake rake (see Section 4.4.1). At larger distance, the peak velocity deficit decays and the area that is affected by the passage of the rider increases. As a consequence of the latter wake widening, a part of the wake eventually exists the measurement domain at very large distance from the cyclist (x/c > 10; not shown here). These conditions are omitted when computing the aerodynamic drag by the wake rake approach. Furthermore, as expected based on the wind tunnel measurements, the in-plane streamlines depict a strong downwash and the presence of a counter-rotating streamwise vortex pair downstream of the lower back and hips (Figure 7.4). As a consequence of turbulent diffusion, also these structures are less prominent at increasing distance from the rider.

The ensemble average aerodynamic drag is obtained in two different rider positions, the up-right and time-trial position. In each position the mean drag is computed from 28 repeated cyclist passages considering only those wake measurements in which the pressure term contribution is negligible. The aerodynamic drag area is obtained with a relative accuracy of approximately 2.5%.

Hence, the drag area in upright position (C_dA ~ 0.27) can reliably be distinguished from that in time-trial position (C_dA ~ 0.23).

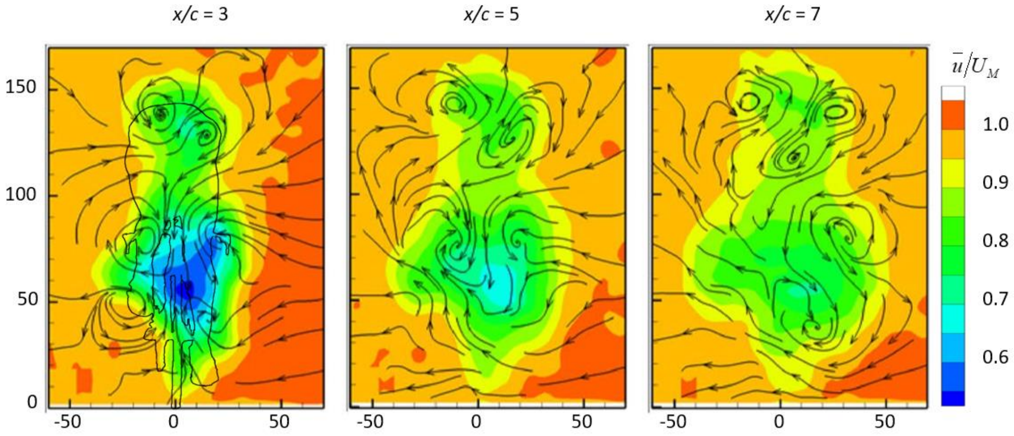

Figure 7.4: Non-dimensional phase average streamwise velocity at three wake stations (Figure adapted from Spoelstra et al. 2019).

Future research with the Ring-of-Fire

A more detailed aerodynamic drag uncertainty investigation is deemed necessary to understand the specific sources of uncertainty and their contributions. More specifically it is recommended, firstly, to measure the cyclist frontal area, in addition to the present PIV recordings, during the cyclist passage to allow evaluation of the drag coefficient, instead of C_DA, and separate possible variations of the frontal area during single transits and among repeated ones. Moreover, to evaluate the drag resolution of this technique, a rider in static position may be used, using an engine driven bike. This would remove any drag uncertainty as a consequence of the pedalling motion and the corresponding drag variations. Secondly, the sensitivity of the measured drag coefficient to the inlet flow conditions should be investigated to understand the conditions in which the system provides acceptable accuracy. Such analysis may also allow characterization of the flow turbulence that, in turn, can be used in the design and test process of low-drag skinsuits (see Section 5.5).

The present Ring-of-Fire experimental setup consists of two cameras and a laser that illuminates a plane from one direction. This arrangement allows measurement prior and after passage of the cyclist. Near-wake measurements, close to the athlete body, instead, are difficult as a result of model shadows and optical blockage. An extension of the PIV experimental arrangement is recommended to partially remedy this so that the flow closer to the cyclist can be measured. This is necessary, among others, to investigate the flow around individual cyclist limbs. Illumination from multiple directions may be achieved using LED illumination installed in an arc or ring formation around the measurement plane (somehow similar to the Ring-of-Fire illustration in Sciacchitano et al. 2015) to avoid shadows. Note that the use of LED light also aids in safe usage of the system and it makes the use of laser safety goggles redundant. Furthermore, increasing the amount of cameras may reduce optical model blockage and, hence, allows flow inspection more generally around the body.

A

EFFECT OF SEEDER POSITION ON AERODYNAMIC DRAG

Balance measurements are conducted simultaneously to PTV at each position of the seeding system. The HFSB seeder is traversed into 15 positions, depicted in Figure A.1-left. For each position the obtained drag force is presented in Figure A.1-right. Clearly, the measured drag at positions 7 and 8 is largely affected by the seeder upstream of the model, with a drag value 4 to 8 % below that of the other positions. In these cases, the lateral position of the supporting strut of the seeder coincides with that of the wind tunnel model and, hence, the velocity deficit in the wake of the former reduces the drag measured on the latter. This reduction in drag, however, is not observed for seeder position 9. In this position the strut supporting the seeder is entirely below the ground plate and its wake cannot interact with the wind tunnel model. Therefore, it is concluded that it is mainly the wake of this strut, and not that of the seeder itself, that interacts with the bike and the mannequin and reduces its drag.

In the wake of the strut, generally, no or little seeding is present and particle tracks are scarce in this region. Hence, it is assumed that the wake of the strut has a negligible effect on the measured velocity and the resulting drag measured by the PIV wake rake. To compare the drag obtained by the PIV wake rake and that of the force balance, therefore, the measurements of the latter that are affected by the strut are excluded. To identify these data points, the drag values outside one standard deviation from the mean obtained over all seeder positions are excluded in the computation of the final statistical mean aerodynamic drag. The standard deviation of the data excluding these outliers is considered the uncertainty of the mean drag and is presented by the error bars in Figure 4.11-top-left.

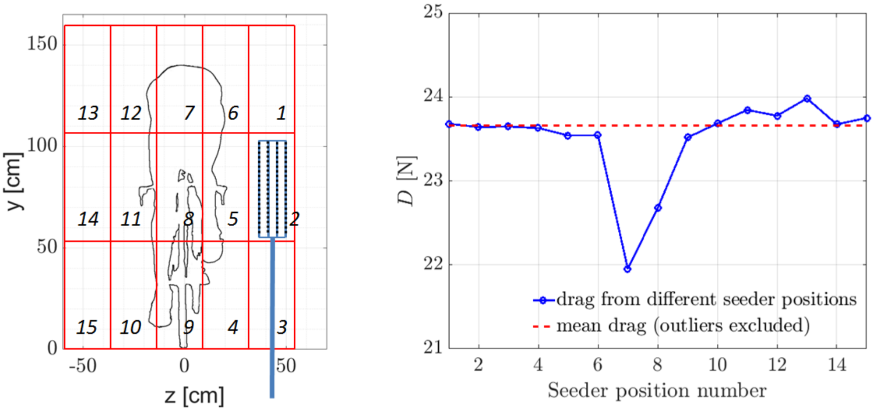

Figure A.1: Seeder position numbering and illustration of seeder position 2 (left) and the effect of the seeder on the measured aerodynamic drag with the balance at $U_\infty = 12.97$ m/s (right).

B

CROPPING PROCEDURE OF PIV WAKE RAKE INTEGRATION AREA

During the large seeder PIV wake rake experiments the seeding on the boundary of the present wake plane is scarce resulting in erroneous velocity vectors and a unphysical non-uniform velocity distribution in the freestream region on the edges of the measured wake plane (Figure 4.6). Furthermore, the seeding distribution in the wake plane varied during the measurements causing large unphysical velocity fluctuations in that same area (Figure 4.7). To minimize propagation of these errors into the PIV wake rake aerodynamic drag the wake area, used for the drag analysis, is cropped, omitting the near-boundary region that does not result from the interaction between the model and the fluid. The area $A_{wake\ rake}$ that is used for drag computation is defined following this logic:

1. Define an initial area for drag computation, $A_{wake\ rake}$:
    a. Find the cell with minimum streamwise velocity. This is the first cell that is part of $A_{wake\ rake}$.
    b. Expand the area with all cells that are within a radius of 3 cells of the boundary of $A_{wake\ rake}$ requiring that in each newly added cell $u/U_{\infty,tunnel} < 0.95$, where $U_{\infty,tunnel}$ is the speed measured by a calibrated pitot-tube inside in the settling chamber of the wind tunnel.
    c. Repeat step *1b* until no cells are added anymore.
2. Expand the area $A_{wake\ rake}$ resulting after step *1*:
    a. Expand the area $A_{wake\ rake}$ with all cells directly adjacent to it requiring that in the newly added cells $u/U_{\infty,tunnel} < 0.98$ and u in the new cell is larger than that in the boundary cells of $A_{wake\ rake}$ along y and z-direction.

Repeat step *2a* three times.

C

CHARACTERIZATION OF ENVIRONMENTAL FLOW

This appendix provides a characterization of the flow prior to the passage of the sphere during the *multi-velocity* experiments. Figure C.1-left depicts this environmental velocity in terms of the spatial distribution of time-average velocity and its fluctuations, obtained from 53 repeated experiments at a model speed of 1.34 m/s. The results at the other speeds are omitted for reasons of conciseness. Note that this Figure reports the stream velocity u^* measured in the laboratory frame of reference, in contrast to the results depicted in Figures Figure 6.8-Figure 6.11, which report the velocity in the model frame of reference. The time-averaged velocity distribution (Figure C.1-top-left) depicts a streamwise velocity up to 4% of the model velocity, which corresponds to up to 20% of the streamwise velocity measured in the wake of the model (Figure C.1-top-middle). Hence, for a correct estimate of the drag value, the streamwise velocity deficit $\Delta u^* = u^*_{wake} - u^*_{env}$ must be considered, which is illustrated in Figure C.1-top-right. In the latter, the velocity difference is brought close to zero almost everywhere outside of the sphere wake, except for the strut wake region. Fluctuations in the environment prior to the passage appear relatively uniform and limited to approximately 1.5% of the model velocity (Figure C.1-bottom-left). The fluctuations in the wake (Figure C.1-bottom-middle) are concentrated around the cross section of the model. Subtracting the initial velocity of the environment, the level of the fluctuations outside of the wake is reduced considerably (Figure C.1-bottom-right), which further clarifies the increased precision of the PIV wake rake when u^*_{env} is accounted for.

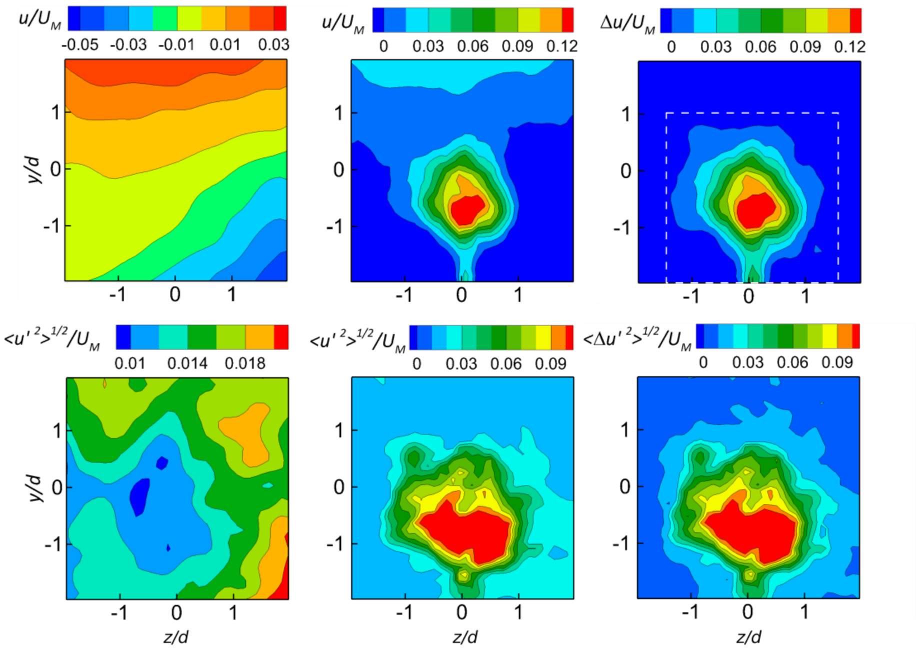

Figure C.1: Spatial distribution of the ensemble average streamwise velocity (top) and its fluctuations (bottom). Velocity prior to the passage of the model at $T = -6$, u^*_{env} (left), and after five diameters ($T = 5$), u^*_{wake} (middle). Net velocity deficit, $\Delta u^* = u^*_{wake} - u^*_{env}$ (right) for a model speed of 1.34 m/s.

REFERENCES

Achenbach E (1968) Distribution of local pressure and skin friction around a circular cylinder in cross-flow up to Re = 5 × 10^6. J Fluid Mech 34(4):625-639

Achenbach E (1971) Influence of surface roughness on the cross flow around a cylinder. J Fluid Mech 46(2):321-335

Achenbach E (1972) Experiments on the flow past spheres at very high Reynolds numbers. J Fluid Mech 54(3) 565-575

Achenbach E (1974) The effect of surface roughness and tunnel blockage on the flow past spheres. J Fluid Mech 65(1):113-125

Adrian RJ (1997) Dynamic ranges of velocity and spatial resolution of particle image velocimetry. Meas Sci Technol 8:1393-1398

Agüera N, Cafiero G, Astarita T, Discetti S (2016) Ensemble 3D PTV for high resolution turbulent statistics. Meas Sci Technol 27 124011

Alons HJ (2008) OJF External Balance. Nationaal Lucht en Ruimtevaartlaboritorium (National Aerospace Laboratory NLR) NLR-CR-2008-695

Anderson Jr JD (1991) Fundamentals of aerodynamics. International Edition McGraw-Hill, New York

Ayoub A, Karamcheti K (1982) An experiment on the flow past a finite circular cylinder at high subcritical and supercritical Reynolds numbers. J Fluid Mech 118:1-26

Bakić VV, Schmid M, Stanković BF (2006) Experimental investigation of turbulent structures of flow around a sphere. Thermal Sci 10:97-112

Barry N, Burton D, Sheridan J, Thompson M, Brown NAT (2014) Aerodynamic performance and riding posture in road cycling and triathlon. J Sports Engin Techn 1-11

Barry N, Burton D, Sheridan J, Thompson M, Brown NAT (2015) Aerodynamic drag interactions between cyclists in a team pursuit. J Sports Engin18:93–103

Barry N, Burton D, Sheridan J. Thompson N, Brown NAT (2016) Flow field interactions between two tandem cyclists. Exp Fluids 57:181

Bearman PW (1969) On vortex shedding from a circular cylinder in the critical Reynolds number regime. J Fluid Mech. 37(3):577-585

Blocken B, Defraeye T, Koninkx E, Carmeliet J, Hespel P (2013) CFD simulations of the aerodynamic drag of two drafting cyclists. Comp Fluids 71:435-445

Blocken B, van Druenen T, Toparlar Y, Andrianne T (2018a) Aerodynamic analysis of different cyclist hill descent positions. J Wind Eng Ind Aerodyn 181:27-45

Blocken B, van Druenen T, Toparlar Y, Malizia F, Mannion P, Andrianne T, Marchal T, Maas G, Diepens J (2018b) Aerodynamic drag in cycling pelotons: New insights by CFD simulation and wind tunnel testing. J Wind Eng Ind Aerodyn 179:319-337

Bosbach J, Kühn M, Wagner C (2009) Large scale particle image velocimetry with helium filled soap bubbles. Exp Fluids 46(3):539-547

Bouillod A, Pinot J, Froncioni A, Grappe F (2015) Validity of Track Aero System to assess aerodynamic drag in professional cyclists. J Sci and Cycling, 4(2)

Brownlie L (1992) Aerodynamic characteristics of sports apparel. PhD Thesis. National Library of Canada

Brownlie L, Kyle C, Carbo J; Demarest N, Harber E, MacDonald R, Nordstrom M (2009) Streamlining the time trial apparel of cyclists: The Nike Swift Spin project. Sports Technol 2:53-60

Brücker C (2001) Spatio-temporal reconstruction of vortex dynamics in axisymmetric wakes. J Fluid Struct 15:543-554

Brune GW (1994) Quantitative Low-Speed Wake Surveys. J Aircraft 31(2)

Bursnall WJ, Loftin Jr LK (1951) Experimental investigation of the pressure distribution about a yawed circular cylinder in the critical Reynolds number range. NACA TN 2463, NASA, Washington DC

Capone A, Klein C, Di Felice F, Miozzi M (2016) Phenomenology of a flow around a circular cylinder at sub-critical and critical Reynolds numbers. Phys Fluids 28(7) 101063

Caridi GCA, Ragni D, Sciacchitano S, Scarano F (2016) HFSB-seeding for large-scale tomographic PIV in wind tunnels. Exp Fluids 57:190

Caridi GCA (2018) Development and application of helium-filled soap bubbles. PhD Thesis. TU Delft Repository

Chabroux V, Mba MN, Sainton P, Favier D (2010) Wake characteristics of time trial helmets using PIV-3C technique. In: Proceedings 15th Int Symp Appl Laser Techn Fluid Mech, Lisbon, Portugal

Chopra G, Mittal S(2017) The intermittent nature of the laminar separation bubble on a cylinder in uniform flow. Comp Fluids 142:118-127

Constantinescu GS, Squires KD (2003) LES and DES investigations of turbulent flow over a sphere at Re = 10,000. Flow Turb Comb 70:267–298

Constantinescu GS, Squires K (2004) Numerical investigations of flow over a sphere in the subcritical and supercritical regimes. Phys of Fluids 16 1449

Coutanceau M, Bouard R (1977) Experimental determination of the main features of the viscous flow in the wake of a circular cylinder in uniform translation. Part 2. Unsteady flow. J Fluid Mech 79:257-272

Crouch TN (2013) Flow topology & large-scale wake structures around elite cyclists. PhD thesis. Monash University. Faculty of Engineering. Depart Mech Aerospace Engineering

Crouch TN, Burton D, Brown NAT, Thomson MC, Sheridan J (2014) Flow topology in the wake of a cyclist and its effect on aerodynamic drag. J Fluid Mech 748:5-35

Crouch TN, Burton D, Thompson MC, Brown NAT, Sheridan J (2016a) Dynamic leg-motion and its effect on the aerodynamic performance of cyclists. J Fl Str 65 121-137

Crouch TN, Burton D, Venning JA, Thompson MC, Brown NAT, Sheridan J (2016b) A Comparison of the Wake Structures of Scale and Full-scale Pedalling Cycling Models. Proc Engin 147:13-19

Crouch TN, Burton D, LaBry ZA, Blair KB (2017) Riding against the wind a review of competition cycling aerodynamics. Sports Eng 20:81-110

De Kat R, Bleischwitz R (2016) Towards instantaneous lift and drag from stereo-PIV wake measurements. In: Proceedings 18th Int Symp Appl Laser Imag Techn Fluid Mech, Lisbon, Portugal

D'Auteuil A, Larose GL, Zan SJ (2012) Wind turbulence in speed skating: Measurement, simulation and its effect on aerodynamic drag. J Wind Eng Ind Aerodyn 104-106: 585-593

Debraux P, Grappe F, Manolova AV, William B (2011) Aerodynamic drag in cycling: Methods of assessment. Sports Biomech 10(3):197-218

Defraeye T, Blocken B, Koninckx E, Hespel P, Carmeliet J (2010) Aerodynamic study of different cyclist positions: CFD analysis and full-scale wind-tunnel tests. J Biomech 43(7):1262-1268.

Defraeye T, Blocken B, Koninckx E, Hespel P, Carmeliet J (2011) Computational fluid dynamic analysis of drag and convective heat transfer of individual body segments for different cyclist positions. J Biomech 44:1695-1701

Elsinga GE, Scarano F, Wieneke B, van Oudheusden BW (2006) Tomographic particle image velocimetry. Exp Fluids 41:933-947

Elsinga GE, Westerweel J, Scarano F, Novara M (2011) On the velocity of ghost particles and the bias errors in Tomographic-PIV. Exp Fluids 50(4): 825-838

Faleiros DE, Tuinstra M, Sciacchitano A, Scarano F (2018) Helium-filled soap bubbles tracing fidelity in wall-bounded turbulence. Exp Fluids 59:56

Faleiros DE, Tuinstra M, Sciacchitano A, Scarano F (2019) Generation and control of helium-filled soap bubbles for PIV. Exp Fluids 60:40

Fitzgerald S, Kelso R, Grimshaw P, Warr A (2019) Measurement of the air velocity and turbulence in a simulated track cycling team pursuit race. J Wind Eng Ind Aerodyn 190:322-330

Ford MD, Nikolov HN, Milner JS, Lownie SP, DeMont EM, Loth F, Holdsworth DW, Steinman DA (2008) PIV-Measured Versus CFD-Predicted Flow Dynamics in Anatomically Realistic Cerebral Aneurysm Models. J Biomech Engineer 130 021015-1

Fujisawa N, Tanahashi S, Srinivas K (2005) Evaluation of pressure field and fluid forces on a circular cylinder with and without rotational oscillation using velocity data from PIV measurement. Meas Sci Technol 16(4):989-996

Giaquinta D (2018) The flow topology of the Ahmed body in cross-wind. MSc Thesis. TU Delft repository

Gibeau B, Gingras D, Ghaemi S (2018) Evaluation of a full-scale helium-filled soap bubble generator. Exp Fluids 61:28

Grappe F (2009) Résistance totale qui s'oppose au déplacement en cyclisme [Total resistive forces opposed to the motion in cycling]. In: Cyclisme et Optimisation de la Performance (2nd edn.) [Cycling and optimisation of performance] (p. 604). Paris: De Boeck Université, Collection Science et Pratique du Sport

Griffith MD, Crouch T, Thompson MC, Burton D, Sheridan J, Brown NA (2014) Computational fluid dynamics study of the effect of leg position on cyclist aerodynamic drag. J Fluids Engineering 136(10) 101105

Guglielmo JJ, Selig MS (1996) Spanwise variations in profile drag for airfoils at low Reynolds numbers. J of Aircraft 33:699-707

Hanna RK (2002) Can CFD make a performance difference in sport? Eng Sport 4:17–30

Herman GT, Lent A (1976) Iterative reconstruction algorithms. Comput Bio Med 6:273-294

Huhn F, Schanz D, Gesemann S, Dierksheide U, van de Meerendonk R, Schröder A (2017) Large-scale volumetric flow measurement in a pure thermal plume by dense tracking of helium-filled soap bubbles. Exp Fluids 58:116

Jang YI, Lee SJ (2008) PIV analysis of near-wake behind a sphere at a subcritical Reynolds number. Exp Fluids 44:905-914

Jones BM (1936) Measurement of profile drag by the pitot-traverse method. ARC R&M 1688

Jux C, Sciacchitano A, Schneiders JFG, Scarano F (2018) Robotic volumetric PIV of a full-scale cyclist. Exp Fluids 59:74

Jux C, Scarano F, Sciacchitano A (2019). Aerodynamic pressure reconstruction on generic surfaces from robotic PIV measurements. In: Proceedings 13th Int Symp Particle Image Velocimetry, Munich, Germany

Kähler CJ, Scharnowski, Cierpka C (2012) On the resolution limit of digital particle image velocimetry. Exp Fluids 52:1629-1639

Kühn M, Ehrenfried K, Bosbach J, Wagner C (2011) Large-scale tomographic particle image velocimetry using helium-filled soap bubbles. Exp Fluids 50:929-948

Kurtulus DF, Scarano F, David L (2007) Unsteady aerodynamic forces estimation on a square cylinder by TR-PIV. Exp Fluids 42:185-196

Kyle CR, Burke ER (1984) Improving the racing bicycle. Mech Eng 106(9):34-45

Lallement P (1866) Velocipede. US Patent No. 59915, United States Patent and Trademark office

Lehmkuhl O, Rodriguez I, Borell R, Chiva J, Oliva A (2014) Unsteady forces on a circular cylinder at critical Reynolds numbers. Physics of Fluids 26 125110

Lienhard JH (1966) Synopsis of Lift, Drag, and Vortex Frequency Data for Rigid Circular Cylinders. Techn Ext Serv, College Engineer Research Division 300

Lignarolo LEM, Ragni D, Krishnaswami C, Chen Q, Simão Ferreira CJ, Van Bussel GJW (2014) Experimental analysis of the wake of a horizontal-axis wind-turbine model. Renew Energy 70:31-46

Liu Z, Zheng Y, Jia L, Jiao J and Zhang Q (2006) Stereoscopic PIV studies on the swirling flow structure in a gas cyclone. Chem Eng Sci 61:4252-4261

Lukes RA, Hart JH, Chin SB, Haake SJ (2005) The understanding and development of cycling aerodynamics. Sports Engineering 8:59-74

Lynch KP, Scarano F (2015) An efficient and accurate approach to MTE-MART for time-resolved tomographic PIV. Exp Fluids 56:66

Maas HG, Gruen A, Papantoniou D (1993) Particle tracking velocimetry in three-dimensional flows. Exp Fluids 15:133-146

Malizia F, Blocken B (2020) Bicycle aerodynamics: History, state-of-the-art and future perspectives. J Wind Eng Ind Aerodyn 200:104134

Martin JC, Milliken DL, Cobb JE, McFadden KL, Coggan AR (1998) Validation of a mathematical model for road cycling power. J Appl Biomech 14:276-291

Martin JC, Davidson CJ, Pardyjak ER (2007) Understanding sprint-cycling performance: the integration of muscle power, resistance, and modeling. Int J Sports Physiol Perform 2(1):5-21

Maskell EC (1973) Progress towards a method for the measurement of the components of the drag of a wing of finite span. RAE technical report 72232

McClure J, Yarusevych S (2016) Surface and Wake Pressure Fluctuations of a Cylinder in Transitional Flow Regime. In: Proceedings 18th Int Symp Appl Laser Imag Techn Fluid Mech, Lisbon, Portugal

Meinhart CD, Wereley ST and Santiago JG (2000) A PIV algorithm for estimating time-averaged velocity fields. J Fluids Eng 122:285-289

Melling A (1997) Tracer particles and seeding for particle image velocimetry. Meas Sci Technol 8:1406

Mercker E, Wiedemann J (1996) On the correction of interference effects in open jet wind tunnels. SAE Trans J Engines 105(6):795-809

Mohebbian A, Rival D (2012) Assessment of the derivative-moment transformation method for unsteady-load estimation. Exp Fluids 53:319-330

Moradian N, Ting DSK, Cheng S (2009) The effects of freestream turbulence on the drag coefficient of a sphere. Exp Thermal and Fluid Sci 33:460-471

Müller RHG, Scherer T, Rotger T, Schaumann O and Markwart M (1997) Large body aircraft cabin a/c flow measurement by helium bubble tracking. J Flow Vis Image Proc 4(3):295-306

Neeteson NJ, Bhattacharya S, Rival DE, Michaelis D, Schanz D, Schröder A (2016) Pressure-field extraction from Lagrangian flow measurements: first experiences with 4D-PTV data. Exp Fluids 57:102

Norberg C (1986) Interaction between freestream turbulence and vortex shedding for a single tube in cross-flow. J Wind Eng Ind Aerodyn 23:501-514

Norberg C , Sunden B (1987) Turbulence and Reynolds number effects on the flow and fluid forces on a single cylinder in cross flow. J Fluids Struct 1(3):337-357

Norberg C (1998) LDV-measurements in the near wake of a circular cylinder. In: Proceedings Advances in Understanding of Bluff Body Wakes and Vortex-Induced Vibration, Washington DC, USA

Norman AK, McKeon BJ (2011) Unsteady force measurements in sphere flow from subcritical to supercritical Reynolds numbers. Exp Fluids 51:1439-1453

Novara M, Scarano F (2013) A particle-tracking approach for accurate material derivative measurements with tomographic PIV. Exp Fluids 54:1584

Novara M, Schanz D, Reuther N, Kähler CJ, Schröder A (2016) Lagrangian 3D particle tracking in high-speed flows: Shake-The-Box for multi-pulse systems. Exp Fluids 57:128

Oggiano L, Troynikov O, Konopov I, Subic A, Alam F (2009) Aerodynamic behaviour of single jersey fabrics with different roughness and cover factors. Sports Eng 12:1-12

Okajima A (1977) Aerodynamic characteristics of stationary tandem cylinders at high Reynolds numbers. Bulletin of the Japan Society of Mechanical Engineers 22:504-511

Okajima A, Sukitana K (1981) Aeroelastic oscillation of a cylinder in tandem arrangements. Bulletin of the Research Institute of Applied Mechanics, Kyushu University 57, 247-265 (in Japanese).

Ozgoren M, Okbaz A, Kahraman A, Hassanzadeh R, Sahin B, Akilli H, Dogan S (2011) Experimental Investigation of the Flow structure around a sphere and its control with jet flow via PIV. In: Proceedings 6th Int Advanc Technol Symp, Elazığ, Turkey

Pearcey HH, Cash RF, Salter IJ, Bormond A (1982) Interference effects on the drag loading for groups of cylinders in uni-directional flow. National Maritime Institute Report NMI-R-130

Petrushov VA (1998) Improvement in vehicle aerodynamic drag and rolling resistance determination from coast-down tests. Proc Instn Mech Engrs, 212(D)

Philipsen I, Hoeijmakers H, Alons HJ (2004) A new balance and air-return line bridges for DNW-LLF models. NLR-TP-2004-315

Prasad AK (2000) Stereoscopic particle image velocimetry. Exp Fluids 29:103-116

Raffel M, Willert CE, Scarano F, Kähler CJ, Wereley ST, Kompenhans J (2018) Particle Image Velocimetry - A Practical Guide. Springer International Publishing

Rodriguez I, Lehmkuhl O, Chiva J, Oliva A (2015) On the flow past a circular cylinder from critical to super-critical Reynolds numbers: Wake topology and vortex shedding. Int J Heat Fluid Flow 55:91-103

Roshko A (1955) On the wake and drag of bluff bodies. J Aeronautical Sciences 22:124-132

Roshko A (1961) Experiments on the flow past a circular cylinder at very high Reynolds number. J Fluid Mech 10:345-356

Sakamoto H, Haniu H (1990) A study on vortex shedding from spheres in a uniform flow. J Fluids Eng 112:386

Saredi E, Sciacchitano A, Scarano F (2020) Multi-Δt 3D-PTV based on Reynolds decomposition. Meas Sci Technol (accepted manuscript)

Scarano F, Riethmuller ML (2000) Advances in iterative multigrid PIV image processing. Exp Fluids 29:S051-S060

Scarano F, Moore P (2012) An advection-based model to increase the temporal resolution of PIV time series. Exp Fluids 52:919–933

Scarano F (2013) Tomographic PIV: principles and practice. Meas Sci Technol 24:012001

Scarano F, Ghaemi S, Caridi GCA, Bosbach J, Dierksheide U, Sciacchitano A (2015) On the use of helium-filled soap bubbles for large-scale tomographic PIV in wind tunnel experiments. Exp Fluids 56:42

Schanz D, Gesemann S, Schroeder A (2016) Shake The Box: Lagrangian particle tracking at high particle image densities. Exp Fluids 57-70

Schewe G (1983) On the force fluctuations acting on a circular cylinder in crossflow from subcritical up to transcritical Reynolds numbers. J Fluid Mech 133:265-285

Schlichting H (1964) Grenzschicht-Theorie, pp 215-220. Karlsruhe: Braun

Schneiders J.F.G, Caridi GCA, Sciacchitano A, Scarano F (2016) Large-scale volumetric pressure from tomographic PTV with HFSB tracers. Exp Fluids 57:164

Schneiders JFG, Jux C, Sciacchitano A, Scarano F (2018) Coaxial volumetric velocimetry. Meas Sci Technol 29 065201

Sciacchitano A, Scarano F, Wieneke B (2012) Multi-frame pyramid correlation for time-resolved PIV. Exp Fluids 53:1087-1105

Sciacchitano A, Scarano F (2014) Elimination of PIV light reflections via a temporal high pass filter. Meas Sci Technol 25(8):084009

Sciacchitano A, Caridi GCA, Scarano F (2015) A quantitative flow visualization technique for on-site sport aerodynamics optimization. Proc Engineer 112:412-417

Shah YH (2017) Drag analysis of full scale cyclist model using large-scale 4D-PTV. MSc Thesis. TU Delft repository

Shih WCL, Wang C, Coles D, Roshko A (1993) Experiments on Flow Past Rough Circular Cylinders at Large Reynolds Numbers. J Wind Eng Ind Aerodyn 49:351-368

Sirovich L (1987) Turbulence and the dynamics of coherent structures. I-III Quart Appl Math 45(3):561-590

Spoelstra AMCMG, de Martino Norante L, Terra W, Sciacchitano A, Scarano F (2019) On-site cycling drag analysis with the Ring of Fire. Exp Fluids 60:90

Terra W, Sciacchitano A, Scarano F (2017) Aerodynamic drag of a transiting sphere by large-scale tomographic-PIV. Exp Fluids 58:83.

Terra W, Sciacchitano A, Shah Y.H. (2019) Aerodynamic drag determination of a full-scale cyclist mannequin from large-scale PTV measurements. Exp Fluids 60:29

Tropea C, Yarin A, Foss JF (2007) Springer handbook of experimental fluid mechanics. Springer, Berlin

Unal MF, Lin JC, Rockwell D (1997) Force prediction by PIV imaging: a momentum based approach. J Fluids Struct 11:965-971

Union Cycliste Internationale (2020, April 7) UCI Cycling Regulations: Part 1 General Organization of Cycling as a Sport. www.uci.org

Unnikrishnan S, Gaitonde DV (2019) First-mode-induced nonlinear breakdown in a hypersonic boundary layer. Computer and Fluids 191 104249

Van Dyke M (1982) An album of fluid motion. The Parabolic Press, Stanford, California

Van Oudheusden BW, Scarano F, Casimiri EWF (2006) Non-intrusive load characterization of an airfoil using PIV. Exp Fluids 40:988–992

Van Oudheusden BW, Scarano F, Roosenboom EWM, Casimiri EWF, Souverein LJ (2007) Evaluation of integral forces and pressure fields from planar velocimetry data for incompressible and compressible flows. Exp Fluids 43:153-162

Van Oudheusden BW (2013) PIV-based pressure measurement. Meas Sci Technol 24 032001

Van Ingen Schenau GJ (1982) The influence of air friction in speed skating. J Biomech 15:449-458

Van Tubergen J, Verlinden J, Stroober M, Baldewsing R (2017) Suited for performance: fast full-scale replication of athlete with FDM. In: Proceedings SCF ’17, Cambridge, MA, USA

Wang R, Cheng S, DS Ting (2019) Effect of yaw angle on flow structure and cross-flow force around a circular cylinder. Phys. Fluids 31 014107

Westerweel J, Scarano F (2005) Universal outlier detection for PIV data. Exp Fluids 39(6):1096-1100

Westerweel J, Elsinga GE and Adrian RJ (2013) Particle image velocimetry for complex and turbulent flows. Annu Rev Fluid Mech 45:409-436

Wielerflits (2017, September 20) Wielerflits. www.wielerflits.be

Wieneke B (2013) Iterative reconstruction of volumetric particle distribution. Meas Sci Technol 24:024008

Wikipedia contributors (2020, April 7) Hour record. In: Wikipedia, The Free Ecyclopedia

Willert CE, Gharib M (1991) Digital particle image velocimetry. Exp Fluids 10:181-93

White BL, Nepf HM (2008) A vortex-based model of velocity and shear stress in a partially vegetated shallow channel. Water Resources Research 44 W01412

Yeo D, Jones PJ (2008) Investigation on 3D characteristics of flow around a yawed and inclined circular cylinder. J Wind Eng Ind Aerodyn 96:1947-1960

Yeon SM, Yang J, Stern F (2016) Large-eddy simulation of the flow past a circular cylinder at sub- to super-critical Reynolds numbers. Applied Ocean Research 59:663-675

Yun G, Kim D, Choi H (2006) Vortical structures behind a sphere at subcritical Reynolds numbers. Phys Fluids 18 015102

Zdravkovich MM (1987) The effects of interference between circular cylinders in cross flow. J Fluid Structures 1:239-261.

Zdravkovich MM (1990) Aerodynamics of bicycle wheel and frame. J Wind Eng Ind Aerodyn 40:55-70

Zdravkovich MM (1997) Flow around circular cylinders. Volume 1: Fundamentals. Oxford University Press, New York

Zdravkovich MM (2003) Flow around circular cylinders. Volume 2: Applications. Oxford University Press, New York

Zdravkovich MM, Brand VP, Mathew G, Weston A (1989) Flow past short circular cylinders with two free ends. J Fluid Mech 203:557-575

ACKNOWLEDGEMENTS

I realize that I may have been quite an odd figure, arriving in the department of Aerodynamics in May 2015 at the age of 35, eight years after graduating from the faculty of Aerospace Engineering of the TU Delft. Going back to academia may have seemed quite a surprise to many. Nevertheless, looking back, I am still happy and a little proud, that I was brave enough to make that decision, as it positively changed my life ever since. Although, I spoke to many friends and family about wanting to quit my job in industry and thinking of starting a PhD, I particularly thank my girlfriend, *Nicky Hogenkamp,* and best friend, *Joost Lasschuit*, for supporting me to make that decision and doing so all the way until today.

That brings me right away to the most important person in my life, not only during the last five years of my research, but since the day we met 17 years ago. *Nicky*, you deserve so much more than a single acknowledgement. Right after the start of my PhD, you convinced me into buying a so-called klushuis and, so, spending a great amount of time and energy in the years after into the transformation of an old school into a modern family home. And, as if working on a PhD and the renovation of a house wasn't enough, in October 2016 our daughter *Bo* was born and two years later, in November 2018, our son *Max*, turning my life upside down. Despite, that it was certainly not always easy and, more than occasionally very stressful: Thank you so much, *Nicky*, for experiencing all of it together with me and helping me in moments of despair! And, *Bo* and *Max*, although you may not yet fully understand, you also helped me a great deal in those hard moments. Looking at the both of you, feeling so much love, reminded me of what is really important in life and it often stopped me from worrying about the slow progress of my research. So thank you little ones.

Now I come to the point where I want to acknowledge my supervisors and my colleagues at the university. Although it may seem of secondary importance, after sharing some of my personal life first. That is certainly not how it is intended. I simply wanted to put my PhD work in perspective first.

From the day I started working under the supervision of my promotor, prof. dr. *Fulvio Scarano* and my co-promotor, dr. *Andrea Sciacchitano* (until today I keep double checking if I spelled your name correctly). I have always felt a great amount of confidence from their side that I would be able to accomplish writing and defending, what has become, the present dissertation. Thank you both for believing in me, coaching me and writing our publications together.

Also I owe quite some acknowledgements to *Daan Bregman*, business director of the Delft Sport Engineering Institute. I met *Daan* even before starting my PhD. It was he how pointed out to me that there could be a possibility to start a PhD in cycling aerodynamics. Thank you *Daan*, without you I would never have contacted Fulvio and, so, I would never have started this PhD. Also thank you for partly funding manufacturing the cyclist replica that I used extensively throughout my research. I also keep very good memories to our trip to Australia for the ISEA conference in Brisbane and our attempts surfing in Noosa Heads. And last but not least, you were largely responsible for convincing my present manager *Kamiel Maase*, to open the position for embedded scientist aerodynamics. So thank you again *Daan* and also you, *Kamiel* for allowing me to take that position at TeamNL.

The last five years would not have been as much fun as they have been without the collaboration with Team Sunweb (before named team Giant Alpecin, among others). Team Sunweb is a German professional cycling team that is managed by Dutch. So hereby I acknowledge the entire team and, in particular, I thank *Tom Davids* and *Teun van Erp* for together making the cyclist replica and designing new low-drag skinsuits for your riders.

I guess all my fellow PhD candidates deserve an acknowledgement somehow. However, I want to mention some of them in particular. Thank you *Beppe Caridi*, for helping me with my earlier experiments and for some seriously dangerous driving in Gottingen (please keep paying attention for traffic lights, especially those red ones!). Also, I want to thank *Tiago Cabral Santos Pestana*, for just being a very friendly and social colleague and friend. I wish you and your family all the best in Sweden. Finally, thank you *Alexander Spoelstra* and *Constantin Jux* for those repeating discussions about cycling and what would be the best road bike to buy and for helping me during several experiments. Good luck to the both of you finishing your PhD's and enjoy those crazy cycling and triathlon events you will participate in.

Also I want to acknowledge the students that joined my research for their master thesis work, an internship or any other occasion. Thank you *Martyna Goral*, *Alexander Spoelstra* (again), *Yash Shah*, *Luigi de Martino Norante*, *Francesco Scarano* and *Florian Adam.*

For helping me printing this dissertation, for opening the front door, again and again (I tend to regularly forget my pass to enter the building) and for helping me numerous times with all the administrative burdens, I owe *Colette Russo* a big acknowledgement. And also I want to acknowledge our department's technicians *Peter Duyndam*, *Frits Donker Duyvis* and *Dennis Bruikman* for helping me, among others, aligning lasers, building enormous tents in remote sport halls and installing cyclist mannequins in our wind tunnels.

At the start of my PhD, being back at the university after so many years, was quite awkward with so many younger people around. And so, I experienced the regular lunches with my good old friend *Gosse Oldenziel*, as being welcome moments of tranquillity. Thank you *Gosse* for talking about those many surf experiences and about exotic PIV experiments and for having good coffees after lunch.

Finally, I want thank my family. *Mijntje*, thank you for always believing in the decisions I make and supporting me with your ever present positivity. *Evert* and *Carla*, thank you for always being there for me (and Nicky) whenever I needed help with the kids or the house. *Bas* and *Hannie*, thank you as well for all those hours of help, which allowed me to spent the necessary time and energy in writing this dissertation. And, *Koen* and *Daan*, thank you for simply being my brothers and, *Koen*, obviously you deserve an acknowledgement for designing the cover of this booklet.

BIOGRAPHICAL NOTE

Wouter Terra was born on the 16th of January of 1981 in Alkmaar, The Netherlands. He graduated from the faculty of Aerospace Engineering in 2007 with a M.Sc. thesis on the topic 'Development of a Finite-Volume Euler Code for Unsteady Flows' under supervision of dr. G. Carpentieri and prof. dr. van Tooren.

After university Wouter worked, among others, for WENS Chalets, catering and managing a chalet in the French ski village Avoriaz during the winter season of 2007/2008. Subsequently, he travelled for six months around Latin America, experiencing other cultures, before starting as a consultant for the Dutch company ORTEC after the summer of 2009. Being responsible for the successful implementation of advanced scheduling and routing software for companies in the oil and gas industry, Wouter, among others, visited several distribution sites of the Italian company Liquigas and quickly developed a passion for the country's cuisine. It is not surprising that, hereafter, his interest in cooking focused mostly on Italian dishes and recipes.

Wouter competed in Judo competition for most of his pre-university life and, afterwards, started practicing speed skating and cycling. To combine this passion for sports with that for data science and engineering, he quit his job at ORTEC in the end of 2015. To his own surprise, Wouter managed to convince prof. dr. Scarano to offer him a Ph. D. position on the topic of cycling aerodynamic investigation by large-scale PIV within the Aerodynamics department of the TU Delft. Wouter's research is on the applied side of the scientific spectrum to achieve a direct impact in cycling, and more generally, in the sports industry. In October 2018, Wouter started as an embedded scientist aerodynamics for TeamNL in parallel to finishing his PhD work. In his position of sport aerodynamic expert, Wouter is responsible for the development of equipment and knowledge that boosts the performance of Dutch athletes increasing the number of Olympic medals.

LIST OF PUBLICATIONS

Journal articles

Terra W, Sciacchitano A, Scarano F (2020) Cyclist Reynolds number effects and drag crisis distribution. J Wind Eng Ind Aerod 200 104143

Spoelstra AMCMG, de Martino Norante L, **Terra W**, Sciacchitano A, Scarano F (2019) On-site cycling drag analysis with the Ring of Fire. Exp Fluids 60:90

Terra W, Sciacchitano A, Shah YH (2019) Aerodynamic drag determination of a full-scale cyclist mannequin from large-scale PTV measurements. Exp Fluids 60:29

Terra W, Sciacchitano A, Scarano F, van Oudheusden BW (2018) Drag resolution of a PIV wake rake for transiting models. Exp Fluids 59:120

Terra W, Sciacchitano A, Scarano F (2017) Aerodynamic drag of a transiting sphere by large-scale tomographic-PIV. Exp Fluids 58:83

Book contributions

Sciacchitano A, **Terra W**, Schneiders JFG, Jux C, Shah Y, Scarano F (2018) Flow over a Full-Scale Cyclist Model by Tomographic PTV. In: Particle Image Velocimetry, A Practical Guide, 3rd edition, Springer International Publishing AG, Cham, Switzerland

Conference proceedings

Terra W, Sciacchitano A, Scarano F (2019) On the Cyclist's Drag Crisis. J Science & Cycling vol 8, issue 2 57:58

Adam F, **Terra W**, Sciacchitano A (2019) Experimental Characterization of a Cyclist’s Wake. J Science & Cycling vol 8, issue 2

Terra W, Sciacchitano A, Scarano F, van Oudheusden BW (2018) Drag resolution of a PIV wake rake for transiting models. 19th Int. Symp Appl Laser Techn Fluid Mech, Lisbon, Portugal

Spoelstra AMCMG, de Martino Norante L, **Terra W**, Sciacchitano A, Scarano F(2018) An assessment of the Ring of Fire approach for indoor and outdoor on-site sports aerodynamic investigation. 19th Int Symp Appl Laser Techn Fluid Mech, Lisbon, Portugal

Sciacchitano A, **Terra W**, Shah YH (2018) Aerodynamic drag determination of a full-scale cyclist mannequin from large-scale PTV measurements. 19th Int Symp Appl Laser Techn Fluid Mech, Lisbon, Portugal

Spoelstra AMCMG, **Terra W**, Sciacchitano A (2018) The Ring of Fire for in-Field Sport Aerodynamic Investigation. 12th Conf Int Sports Eng Assoc, Brisbane, Australia

Terra W, Sciacchitano A, Scarano F (2018) A Novel Approach for Skin Suit Aerodynamic Optimization Using Local Momentum Deficit. 12th Conf Int Sports Eng Assoc, Brisbane, Australia

Terra W, Sciacchitano A, Scarano F (2016). Aerodynamic drag of transiting objects by large-scale tomographic-PIV. 18th Int Symp Appl Laser Techn Fluid Mech, Lisbon, Portugal

Terra W, Sciacchitano A, Scarano F (2016) Drag Analysis from PIV Data in Speed Sports. Proc Engineer 147:50-55

Terra W, Sciacchitano A, Scarano F (2016) Evaluation of aerodynamic drag of a full-scale cyclist model by large-scale tomographic-PIV. Int Workshop Non-Intr Opt Flow Diag, Delft, The Netherlands

Terra W, Sciacchitano A, Scarano F (2015) Large-scale tomo-PIV for on-site drag analysis in speed sports. Workshop Non-Intr Meas Unstead Flows Aerodyn, Poitiers, France